Design of a 250 GHz Gyrotron Amplifier

by

Emilio A. Nanni

B.S. Electrical Engineering, University of Missouri - Rolla (2007)
B.S. Physics, University of Missouri - Rolla (2007)

Submitted to the
Department of Electrical Engineering and Computer Science
in partial fulfillment of the requirements for the degree of

Master of Science

at the

MASSACHUSETTS INSTITUTE OF TECHNOLOGY

September 2010

Author .....
Department of Electrical Engineering and Computer Science
August 17, 2010

Certified by .....
Richard J. Temkin
Senior Research Scientist, Department of Physics
Thesis Supervisor

Accepted by .....
Professor Terry P. Orlando
Chairman, Committee on Graduate Students
Department of Electrical Engineering and Computer Science

Design of a 250 GHz Gyrotron Amplifier

by

Emilio A. Nanni

Submitted to the Department of Electrical Engineering and Computer Science
on August 17, 2010, in partial fulfillment of the
requirements for the degree of
Master of Science

Abstract

A design is presented of a 250 GHz, 1 kW gyrotron traveling wave tube (gyro-TWT) amplifier with gain exceeding 50 dB. Calculations show that the amplifier will operate at 32 kV, 1 A with a saturated gain of 60 dB, an output power of 1 kW and a gain bandwidth of 3 GHz. The amplifier uses a novel photonic band gap (PBG) interaction circuit for stable single mode operation in an overmoded circuit. The design mode is a TE_{03}-like mode confined by the PBG lattice with no nearby competing modes. The design of the input coupler, interaction circuit, output coupler and electron gun have also been completed. The amplifier design accounts for requirements imposed by the device's intended application of pulsed nuclear magnetic resonance spectroscopy with pulses as short as several hundred picoseconds. This design will be implemented at a later date for the construction of the highest frequency, kW power level amplifier based on vacuum electronics. To gain understanding of short pulse amplification in vacuum electron devices, an experimental study of sub-nanosecond pulse amplification in a gyro-TWT has been carried out on an existing experimental setup at 140 GHz. The gyro-TWT operates with 30 dB of small signal gain in the HE_{06} mode of a confocal waveguide. Picosecond pulses show broadening and transit time delay due to two distinct effects: the frequency dependence of the group velocity near cutoff and gain narrowing by the finite gain bandwidth of 1.2 GHz. Experimental results taken over a wide range of parameters, with pulses as short as 400 ps, show good agreement with a theoretical model in the small signal gain regime.

Thesis Supervisor: Richard J. Temkin

Title: Senior Research Scientist, Department of Physics

Acknowledgments

I would like to thank my advisor, Dr. Richard Temkin, for his guidance and mentorship. He never fails to provide good suggestions and is an invaluable source of knowledge. I would also like to thank Dr. Michael Shapiro for many useful conversations and for patiently answering all of my questions, and Dr. Jagadishwar Sirigiri for all his help in the lab and for keeping me on track. I have benefited from working with all of our group members: Dr. Alan Cook, Dr. Hae Jin Kim, Dr. Colin Joye, Elizabeth Kowalski, Dr. Roark Marsh, Ivan Mastovsky, Brian Munroe, David Tax and Antonio Torrezan de Sousa. You have made this process so enjoyable. I want to thank my instructor for all things DNP, Alexander Barnes. I could never forget my mentors Dr. Reza Zoughi and Dr. Ronald Bieniek, both from the University of Missouri-Rolla, who encouraged me to be a better student, scientist and engineer. On a personal note, I must also thank my parents Antonio and Valeria Nanni who inspired me and provided me with every opportunity. Finally, my fiancée Sarah Wilson, your love is all the support I will ever need.

Contents

List of Figures

List of Tables

Chapter 1

Introduction

1.1 Motivation

Novel high power sources in the millimeter and sub-millimeter wave are of great interest due to their potential applications in spectroscopy, communications and radar. This thesis presents the design of a 250 GHz, 1 kW gyrotron traveling wave tube amplifier for nanosecond pulses with gain exceeding 50 dB. The amplifier will eventually be used in pulsed dynamic nuclear polarization (DNP) nuclear magnetic resonance (NMR) and electron paramagnetic resonance (EPR) experiments. Controlled microwave irradiation of an NMR sample can be used to transfer the high electron polarization to the nucleus under study resulting in a dramatic increase in the NMR signal by factors exceeding 100 [3]. Currently, there are no commercially available devices that can generate peak powers in the kW region with high gain at 250 GHz. A gyrotron amplifier was chosen because it offers high gain, broad bandwidth at these frequencies and allows the use of an overmoded interaction structure resulting in easier fabrication and reduced thermal effects.

Pulsed DNP NMR requires the amplification of pulse trains with ns times scale resolution. In principle an amplifier with over 1 GHz of instantaneous bandwidth should be able to meet this requirement. However, waveguide dispersion and gain dispersion remain a concern for successful operation. In light of these concerns a study of pulse amplification in a 140 GHz gyrotron traveling wave tube (gyro-TWT) was

performed. The 140 GHz gyro-TWT used in the experiment was developed at MIT for use in pulsed DNP. This study was the first investigation of sub-ns pulse amplification in a gyro-TWT, and yielded the first dispersion free amplification of sub-ns Gaussian pulses. The effects of waveguide dispersion and gain dispersion were thoroughly investigated in the linear gain regime of the amplifier. A theory was developed to describe the effects of waveguide and gain dispersion on pulse amplification in gyro-TWTs, in excellent agreement with experimental results.

1.2 Gyrotron Oscillators and Amplifiers

The generation of millimeter and sub-millimeter wavelength radiation at high power has proved to be a significant challenge. Solid state devices have never been considered as a possibility for high power generation at such high frequencies (hundreds of GHz) due to scalability and efficiency issues. Classical microwave tubes, e.g. klystrons and traveling wave tubes, can produce high power (kW) electromagnetic radiation up to 100 GHz, but these slow wave devices require physical structures in the interaction cavity that are smaller than the wavelength of operation. This small element size produces difficulties with thermal damage and manufacturing of the interaction cavity. Gyrotrons are a form of electron cyclotron maser capable of producing kilowatts to megawatts of output power in the microwave, millimeter wave and terahertz bands [18, 12, 22, 36]. These devices operate by the resonant interaction between the eigen-modes of an interaction cavity, typically cylindrical, and a mildly relativistic electron beam that is gyrating in a constant axial magnetic field. The most basic configuration of a gyrotron consists of a magnetron injection gun (MIG) that launches an annular electron beam into the hollow bore of a solenoidal, often superconducting, magnet. The orientation of the DC electric field that extracts the electron beam from the cathode produces a beam that has both a perpendicular and parallel velocity component to the axial field produced by the solenoidal magnet. As the electron beam travels into the central bore, it undergoes adiabatic compression that increases its orbital momentum. The beam enters a metallic cavity that has an eigen-mode resonance

that is close to a harmonic of the frequency at which the electron gyrates around the magnetic field line. The electron beam surrenders some of its kinetic energy to the electromagnetic mode through stimulated emission. The electrons exit the cavity and are deposited on a metallic collector. In its simplest configuration, the collector can also hold an axial dielectric window that couples the electromagnetic radiation out of the device. However, it is often convenient to convert the wave into a Gaussian beam that can be efficiently extracted in a transverse direction using mirrors.

In recent years, gyrotron traveling wave tube (TWT) amplifiers have demonstrated high output power levels with significant gain bandwidths [13, 11, 7]. A gyrotron-TWT amplifier works on the same fundamental principles as a gyrotron oscillator for the extraction of energy from an electron beam. However, the amplifier is operated under conditions that suppress self-start oscillations, including backward wave oscillations (BWOs) that could disrupt the operation of the device. Amplification is achieved in a gyro-TWT by a convective instability supported by a mildly relativistic, annular, gyrating electron beam and a transverse electric mode in a waveguide immersed in a strong static axial magnetic field (B_0). The grazing intersection between the dispersion relation of the cyclotron resonance mode and a transverse electric waveguide mode near the waveguide cutoff results in high gain and moderate bandwidth. The beam mode dispersion relation is given by

$$\omega - s\Omega/\gamma - k_z v_z \geq 0 \tag{1.1}$$

and the waveguide mode dispersion relation is expressed as

$$\omega^2 - k_z^2 c^2 - k_\perp^2 c^2 = 0 \tag{1.2}$$

where ω is the frequency of the wave, $\Omega = eB_0/m_e$ is the non-relativistic cyclotron frequency of the gyrating electrons, e and m_e are, respectively, the charge and the rest mass of the electron, γ is the relativistic mass factor, s=1 is the cyclotron harmonic number, k_z and $k_\perp$ are the longitudinal and transverse propagation constants, respectively, of the waveguide mode, v_z is the axial velocity of the electrons, and c is

the velocity of light. This requires the design of an interaction circuit that supports the propagation of a mode at the correct frequency while appearing lossy to frequencies and modes outside the region of interest. This is usually performed by inserting lossy ceramics, severs and selecting geometries with favorable dispersion relations [29]. Further complications arise when considering the design of an amplifier at 250 GHz because the operational mode of the amplifier cannot be a fundamental mode due to compression restrictions of the electron beam. In a gyro-TWT, the signal of interest must be efficiently coupled into the cavity at the beginning of the interaction region. The wave propagates along the amplifier circuit while extracting energy from the electron beam until it is removed from the device with an output coupler in a similar fashion to the oscillator.

1.3 Background of Gyro-TWTs

Gyro-TWT amplifiers were first studied in the early 1970s, mainly at the Naval Research Laboratory (NRL). These devices were in the X and Ku bands and operated in the fundamental waveguide mode [4, 39]. These early studies showed how the promise of high gain and high output power in gyro-TWTs was limited by the strong forward and backward wave gyrotron oscillations near the waveguide cut-off and interaction at higher harmonics.

More recently, a scheme of distributed loading was proposed by the research group at the National Tsing Hua University (NTSU) in Taiwan to suppress the gyrotron backward wave oscillations (gyro-BWO) and forward wave gyrotron oscillations near the waveguide cut-off. A proof-of-principle device demonstrated over 70 dB of gain at 35 GHz [13]. This device operated in the fundamental TE_{11} waveguide mode. Subsequently, a TE_{01} high average power device based on this concept was demonstrated at NRL [35] and a TE_{01} device was demonstrated at 94 GHz by Communication and Power Industries (CPI) [8]. A comparison of recent gyro-TWT experiments is shown in Table 1.1.

Table 1.1: Recent Gyro-TWT Experiments

	Freq (GHz)	Gain (dB)	Pout (kW)	Voltage (kV)	Current (A)
NTHU[13]	35	70	93	100	3.5
CPI[8]	95	43	1.5	30	1.8
MIT (2003)[42]	140	29	30	65	7
MIT (2008)[29]	140	34	0.8	37	2.7

However, operation at fundamental modes is not feasible at high frequencies such as 250 GHz where the radius of the interaction structure would be of the order of a fraction of a millimeter. This results in high ohmic losses and presents significant challenge in transporting an electron beam over long distances (~20 cm) without causing beam interception on the waveguide walls. In prior research at MIT, gyro-TWTs with high power (30 kW) and low power (0.8 kW) have been successfully demonstrated at 140 GHz [44, 29]. These experiments used a novel quasioptical, overmoded interaction structure which allows for single mode operation in a higher order mode. The interaction circuit consists of a confocal waveguide with severs for additional suppression of oscillations. Such a mode-selective open waveguide imparts high diffractive losses to the lower order modes which tend to interact with the beam more strongly. This selective loading of the lower order modes allows for stable operation in a higher order mode. Though mode selective, the confocal waveguide has an azimuthally asymmetric field profile which reduces its interaction efficiency with the annular beam produced by the MIG that is typically used in gyrotrons.

One important application of millimeter waves is in spectroscopy, where coherent pulses on a sub-nanosecond or picosecond time scale are needed for optical pumping of molecular states. The pulses must be shorter than the relaxation time, typically requiring sub-nanosecond (or picosecond scale) pulse lengths [6]. Sub-nanosecond microwave pulses have been demonstrated in a vacuum electron device by superradiance [21], but such pulses cannot be used for spectroscopy. Sub-nanosecond pulses must contain a spectral bandwidth exceeding the transform limit of 1 GHz. In the conventional microwave bands at frequencies of one to several GHz, the required gain bandwidth to amplify such picosecond pulses is generally not available, since the GHz

bandwidth is a large fraction of the carrier frequency. In recent years, high power, wideband amplifiers in the millimeter wave band have been developed that are suitable for amplifying picosecond pulses. For example, a form of klystron called an extended interaction klystron has been developed at 95 GHz with a gain bandwidth of about 1 GHz. This amplifier has been used to successfully amplify 1 kW output pulses as short as 800 picoseconds [9]. A gyro-TWT at 95 GHz has been demonstrated with a gain bandwidth of 6.5 GHz at an output power level of 2 kW [7]. This gyro-TWT could in principle be used to amplify a 150 ps pulse. To our knowledge, amplification of picosecond pulses has not been tested with these or other powerful wideband gyro-amplifiers. Because of the possibility of distortion in amplification of picosecond pulses, detailed studies are needed of the amplification process in such devices.

1.4 Current Effort

A novel interaction structure that is highly mode selective and has strong coupling with the electron beam resulting in higher interaction efficiency will be presented. The circuit is based on a photonic band gap (PBG) structure made of a two dimensional triangular lattice of metal rods. The dimensions of the lattice are tuned so that it acts as a perfect reflector in a narrow band of frequencies around the operating mode. A defect is created in the lattice by removing some rods, allowing a higher order mode to be confined with high a quality factor (Q). Other modes that can exist in the defect either at higher or lower frequencies suffer significant losses because of the partially transparent lattice. This amplifier will ultimately be applied to coherent molecular spectroscopy. Therefore, the bandwidth of the amplifier has been an important consideration to insure the ability of the gyro-TWT to faithfully amplify very short pulses without distortion, since it is important to the application. The input coupler, output coupler and electron gun designs for this experiment will be presented.

We report a detailed study of amplification of pulses as short as 400 ps in a 1

kW, 140 GHz gyro-TWT with a gain bandwidth exceeding 1 GHz. The gyro-TWT operates with 30 dB of small signal gain near 140 GHz in the HE_{06} mode of a confocal waveguide. Picosecond pulses show broadening and transit time delay due to two distinct effects: the frequency dependence of the group velocity near cutoff and gain narrowing by the finite gain bandwidth of 1.2 GHz. A comparison between theory and experiment in the dispersion of picosecond pulses in a vacuum electron device amplifier was performed by driving the amplifier with pulses as short as 400 ps, which contain frequencies over a 2.5 GHz bandwidth, about twice the amplifier's inherent gain bandwidth. Experimental results show good agreement with a theoretical model in the small signal gain regime. These results show that in order to limit the pulse broadening effect in gyro-amplifiers, it is crucial to both choose an operating frequency at least several percent above the cutoff of the waveguide circuit and operate at the center of the gain spectrum with sufficient gain bandwidth.

Chapter 2

Theory of Gyro-devices

2.1 Axial and Azimuthal Bunching of Electrons

An electron beam propagating along a magnetic field line is subject to a variety of instabilities. Of particular importance are the axial and azimuthal bunching mechanisms of the electromagnetic electron cyclotron instability. The electron cyclotron maser instability is driven by the azimuthal bunching mechanism and requires a relativistic treatment. The Weibel-type instability is driven by axial bunching and does not require relativistic treatment. Both mechanisms exist and compete against each other when an external magnetic field is present [15].

Assume an infinite homogeneous magnetic field $B_0\hat{z}$ with the electron distribution given by

$$f_0 = \delta(p_\perp - p_{\perp 0})\delta(p_z)/2\pi p_\perp \tag{2.1}$$

where $p_\perp$ is the transverse momentum, p_z is the axial momentum and $p_{\perp 0}$ is a constant. This distribution represents streaming electrons in the moving frame. This monoenergetic beam would be the ideal case for an experiment designed to extract energy from the electrons, and it approximates the electron beam produced by high quality electron guns.

If we perturb the electron beam with an electromagnetic wave, the system will

require the linearized relativistic Vlasov equation,

$$\frac{\partial}{\partial t}f_1 + \mathbf{v}\cdot\frac{\partial}{\partial \mathbf{x}}f_1 - \frac{e}{c}\mathbf{v}\times\mathbf{B}_0\cdot\frac{\partial}{\partial \mathbf{p}}f_1 = e\left(\mathbf{E}_1 + \frac{1}{c}\mathbf{v}\times\mathbf{B}_1\right)\cdot\frac{\partial}{\partial \mathbf{p}}f_0 \tag{2.2}$$

and the combined Maxwell's equations,

$$\nabla\times\nabla\times\mathbf{E}_1 = -\frac{1}{c^2}\frac{\partial^2}{\partial t^2}\mathbf{E}_1 - \frac{4\pi}{c^2}\frac{\partial}{\partial t}J_1 \tag{2.3}$$

to fully describe the physics of the interaction. A subscript 0 or 1 represent the initial or perturbed quantity, respectively. The electron distribution is f, E is the electric field, B is the magnetic field, and the current J is defined as

$$\mathbf{J}_1 = -e\int f_1\mathbf{v}d^3p. \tag{2.4}$$

Simplifying the above equations and performing perturbative analysis for a wave that propagates as $\exp(-i\omega t + ik_z z)$, we obtain the relativistic dispersion relation [15]:

$$\omega^2 - k_z^2c^2 = -\pi\omega_p^2\int_0^\infty p_\perp dp_\perp\int_{-\infty}^\infty dp_z$$
$$\times\left[\left(\omega - \frac{k_zp_z}{\gamma m}\right)p_\perp\frac{\partial f_0}{\partial p_\perp} + \frac{k_z}{\gamma m}p_\perp^2\frac{\partial f_0}{\partial p_z}\right](\gamma\omega - k_zp_z/m - \Omega_e)^{-1}$$

where $\omega_p^2 = 4\pi ne^2/m$, $\Omega_e = eB_0/mc$, and $\gamma = (1 + p_\perp^2/m^2c^2 + p_z^2/m^2c^2)^{1/2}$. This expression is for any generic distribution of the electrons. However, we can simplify further by considering the monoenergetic case from Equation (2.1) that is most relevant to practical devices. This reduces the dispersion relation to

$$\omega^2 - k_z^2c^2 = \frac{\omega_p^2}{\gamma_0}\left(\frac{\omega}{\omega - \Omega_e/\gamma_0} - \frac{\beta_{\perp 0}^2(\omega^2 - k_z^2c^2)}{2(\omega - \Omega_e/\gamma_0)^2}\right) \tag{2.5}$$

where $\gamma_0 = (1 + p_{\perp 0}^2/m^2c^2)^{1/2}$ and $\beta_{\perp 0} = p_{\perp 0}/\gamma_0 mc$. To extract some physical interpretation from Equation (2.5) one should make note that the last term on the RHS is where the axial and azimuthal bunching mechanism reside. The azimuthal and axial bunching are represented by the ω^2 and $c^2k_z^2$ terms respectively. Furthermore, the

denominator $(\omega - \Omega_e/\gamma_0)$ imposes a requirement that the frequency of oscillation for the wave must meet the condition $\omega \approx \Omega_e/\gamma_0$ in order to produce a large instability. This can be understood as a requirement for synchronous behavior between the electrons and the electromagnetic wave. Additionally, if the phase velocity of the wave is equal to the speed of light there is no instability present, defining an inflection point between an instability dominated by axial and azimuthal bunching. If

$$\omega^2/k_z^2 > c^2, \tag{2.6}$$

the phase velocity of the wave is greater than the speed of light and azimuthal bunching dominates. If

$$\omega^2/k_z^2 < c^2, \tag{2.7}$$

the phase velocity of the wave is less than the speed of light and axial bunching dominates. In Figure 2-1 the solution to Equation (2.5) is plotted for $\Omega_e/\gamma_0\omega_p = 10$ and $\gamma_0 = 1.02$. We note that the instability is only present when the frequency of the fast and slow wave meet the condition $\omega/\omega_p = 10$ as required for synchronous behavior. The instability for the fast and slow wave are only present when Equations (2.6) and (2.7) are satisfied.

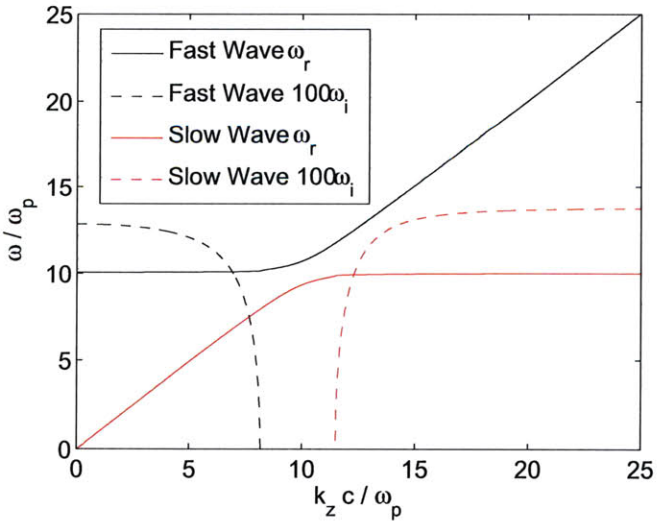

Figure 2-1: The solution to 2.5 for $\Omega_e/\gamma_0\omega_p = 10$ and $\gamma_0 = 1.02$.

Gyrotrons and gyro-TWTs are both fast wave devices that rely electron cyclotron maser instability, driven by the azimuthal bunching mechanism. Due to this bunching mechanism a relativistic treatment is required to explain these devices properly.

2.2 Fundamentals of Gyrotron Oscillators

As mentioned in the previous section, electron cyclotron resonance masers (gyrotrons) are fast wave devices, i.e. the phase velocity of the wave is greater than the speed of light. They are capable of producing high average power in the microwave, millimeter wave and sub-millimeter wave range. The most basic configuration of a gyrotron can be seen in Figure 2-2. The magnetron injection gun that launches an annular electron beam would be located to the left of Figure 2-2(a). The axial magnetic field is produced by a solenoidal magnet than can either be a pulsed magnet or a DC superconducting magnet. As the electron beam travels through the central bore, it enters a metallic cavity that has an eigen-mode resonance that is close in frequency to a harmonic of the frequency at which the electron gyrates around the magnetic field line. The electron beam surrenders some of its kinetic energy to the electromagnetic mode through stimulated emission. In order for the electron to interact with the electromagnetic mode in the cavity, the relativistic electron frequency must be close to the frequency of oscillation for the mode [14]. The relativistic cyclotron frequency is

$$\Omega_{rel} = \frac{eB_0}{\gamma m_e}, \tag{2.8}$$

where B_0 is the DC axial magnetic field, γ is the relativistic mass factor, m_e is the electron mass, e is the charge of the electron. In a cylindrical cavity the dispersion relation for TE modes is

$$k^2 - k_t^2 - k_z^2 = 0, \tag{2.9}$$

where $k = w\sqrt{\mu_0 \epsilon_0}$ is the wave vector in free space, $k_t = \nu_{mn}/r_w$ is the transverse propagation constant, ν_{mn} is the root of a Bessel function and k_z is the axial propagation constant. It can be shown [5] that the Doppler shifted resonance for the electron

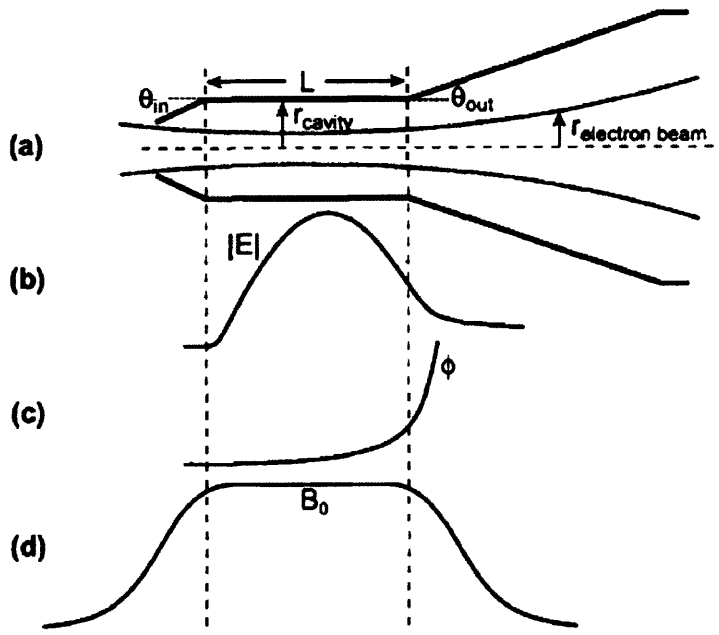

Figure 2-2: Cross section of the interaction region along the axis of the DC magnetic field with (a) a view of the electron beam passing through the physical structure, (b) the amplitude (c) and phase of the RF electric field and (d) the DC magnetic field [26].

becomes

$$\omega - k_z v_z - n\Omega_{rel} = 0, \tag{2.10}$$

and when the frequency of the mode and the resonance intersect, as seen in Figure 2-3, oscillation and stimulated emission can occur. The blue and red line in Figure 2-3 are the electron beam dispersion relations for $n = 1$ and $n = 2$, respectively. The blue dot is a fundamental forward wave oscillation, the red dot is a second harmonic forward wave oscillation and the green dot is a fundamental backward wave oscillation.

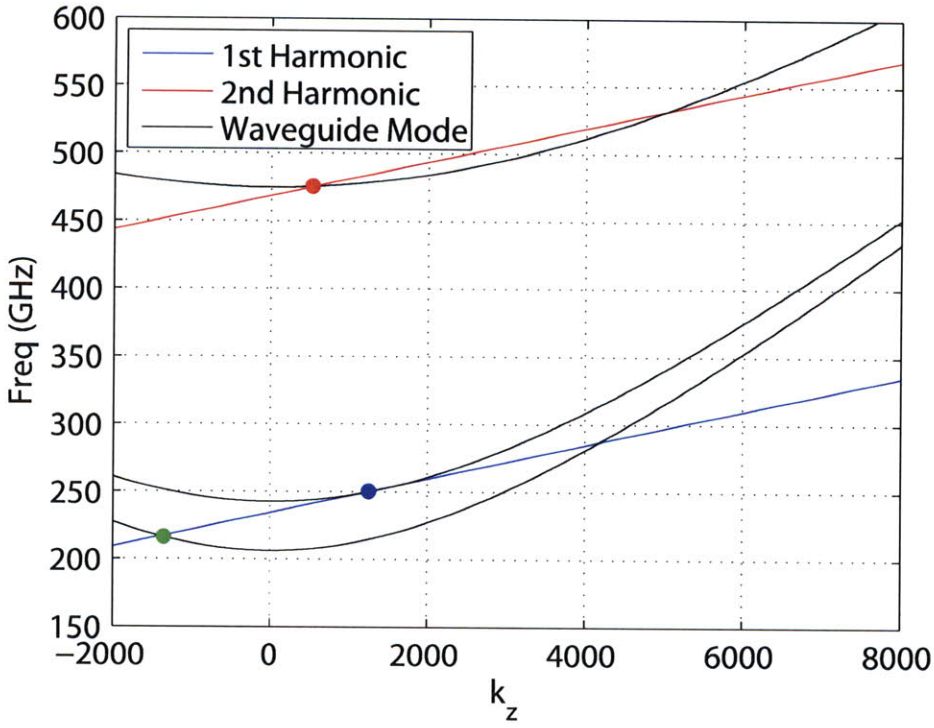

Figure 2-3: Dispersion diagram for cyclotron resonance and cylindrical waveguide modes.

2.3 Background

Gyrotrons were initially proposed due to the cyclotron resonance instability that was discovered independently in the late 1950s by R. Twiss [48], J. Schneider [40] and A. Gapanov [19]. This led to the invention of the gyrotron in a similar configuration to the one described in Section 2.2 by Gapanov et al. [20] with 190 W CW power at 1.2 cm wavelength. This was followed by the design of gyrotrons in the 1970s that could produce several kW of power at frequencies up to 300 GHz by Zaystev et al. [51]. To minimize the thermal load, the production of pulse gyrotron oscillators with several hundred kW of power and high frequencies was completed in the 1980s [47]. In the past two decades the focus has shifted from simply achieving higher frequency devices to providing useful millimeter and sub-millimeter wave sources for Electron Cyclotron Resonance Heating (ECRH) of plasmas [46], Nuclear Magnetic Resonance Dynamic Nuclear Polarization (NMR-DNP) and Electron Paramagnetic

Table 2.1: Illustrative THz Gyrotron Oscillator Experiments

Source	Year	Freq. (GHz)	Cvcl. harm.	Mode (TE_{mnp})	V (kV)	I (A)	P (W)
MIT[27]	2004	460	2	$TE_{0,6,1}$	12.4	0.13	8
IAP[51]	1973	326	2	$TE_{2,3,1}$	27.9	0.9	1500
Fukui[28]	1998	301	1	$TE_{0,3,1}$	14	0.08	17

Resonance (EPR) experiments [3]. This changed the focus to providing reliability, efficient power conversion and delivery, larger bandwidth and signal stability. A new class of device called the gyro-TWT also emerged from the discovery of the cyclotron resonance instability [14] that operates on similar principles, described in Section 2.6 of this paper. Table 2.1 shows some leading CW and pulse gyrotron experiments in terms of frequency of operation, power output, and bandwidth. In Figure 2-4, the achieved single device power output for solid state and vacuum electron devices is plotted. The THz gap is clearly visible with conventional gyrotrons having a clear supremacy for the 100-500 GHz range.

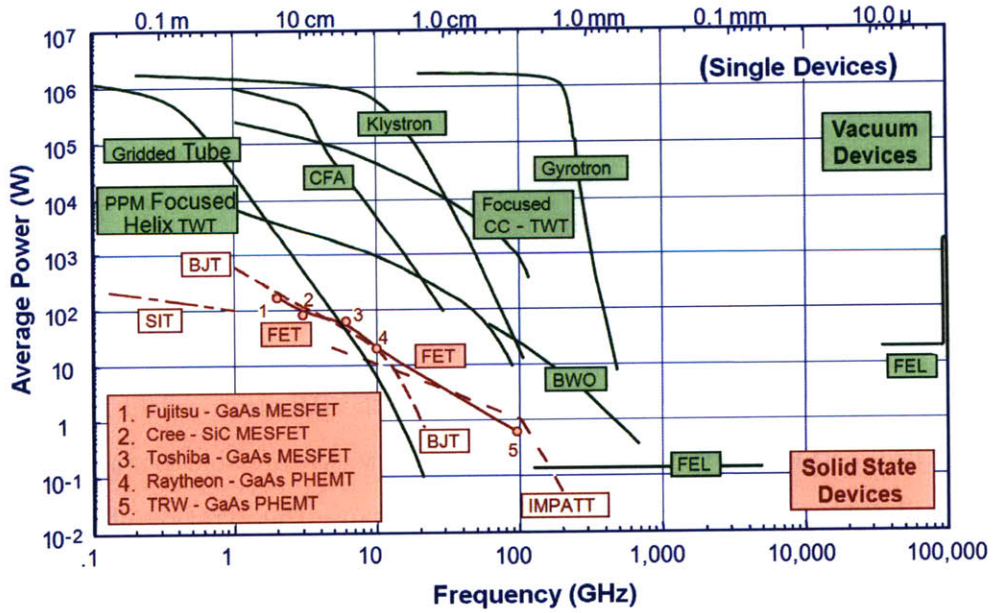

Figure 2-4: Power output for vacuum electron and solid state devices [42].

2.4 Nonlinear Theory of Gyrotron Oscillators

2.4.1 Derivation

To understand the operation of a gyrotron oscillator, we must describe the interaction between an energetic electron and the electromagnetic mode confined in the resonator or interaction cavity. Like all vacuum electron devices, gyrotrons extract kinetic energy from the electron beam as it passes through the interaction cavity. However, a gyrotron does not extract any energy from the axial component of the velocity, only from the transverse direction.

This energy extraction is made possible because an electron traveling in a circular path around a DC magnetic field will feel an accelerating or decelerating force from the oscillating electric field that can deposit or extract energy from the electron. The initial change in energy that results from the applied force causes more energetic electrons to rotate slower and less energetic electrons to rotate faster, because of the change in γ and Ω_{rel}. The different rotational frequencies can produce phase bunched electrons that act coherently to deposit energy into the electromagnetic mode of the cavity. This process can be described by the pendulum equations that relate the change in energy and momentum for the electron to the electric and magnetic fields that are present. These equations of motion are

$$\frac{\partial \mathcal{E}}{\partial t} = -e\mathbf{v} \cdot \mathbf{E}, \tag{2.11}$$

$$\frac{\partial \mathbf{p}}{\partial t} = -e\mathbf{E} - \frac{e}{c}\mathbf{v} \times \mathbf{B}, \tag{2.12}$$

where the electron energy is $\mathcal{E}$, the momentum $\mathbf{p}$, the RF electric field is $\mathbf{E}$, the DC magnetic field is $\mathbf{B}$ and the velocity of the electron is $\mathbf{v}$. We are able to ignore the effect of the oscillating magnetic field on the electron because the gyration of the electron is dominated by the axial magnetic field $\mathbf{B} = B_0\mathbf{z}$. The instantaneous kinetic energy and momentum of a relativistic electron are $\mathcal{E} = \gamma m_e c^2$ and $|\mathbf{p}| = \gamma\beta m_e c$ respectively, where $\gamma = (1 - \beta_\perp^2 - \beta_\parallel^2)^{-\frac{1}{2}}$ and $\beta = v/c$. The $\perp$ symbolizes the component that is

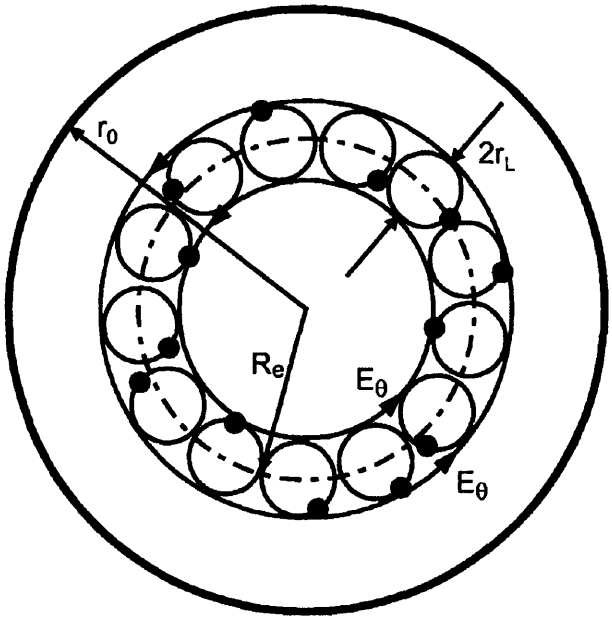

Figure 2-5: Cross section of the interaction region with black dots representing electrons on their gyration orbit [27]. The waveguide radius is r_0, the Larmor radius is r_L, the guiding center radius is R_e and E_θ denotes the $\hat{\theta}$ component of the electric field.

transverse to the beam and the $\|$ represents the axial or z component. It will be useful to convert these equations into normalized variables and to solve the standard and practical case of a cylindrical resonator. The normalized variables will relate to relevant design constraints to be discussed later. To begin this process, we convert to a relative energy for the electron $w = 1 - \gamma/\gamma_0$ which relates to the differential through $\frac{\partial w}{\partial t} = \frac{\partial}{\partial t}(1 - \gamma/\gamma_0) = (-1/\gamma_0 m_e c^2)\frac{\partial \mathcal{E}}{\partial t}$. It is also convenient to convert to a normalized axial position $Z = \omega z/\beta_{\|0}c$ which relates to the differential through $\frac{\partial z}{\partial t} = \beta_\|$ and $\frac{\partial}{\partial t} = \omega\beta_\|/\beta_{\|0}\frac{\partial}{\partial Z}$. The values of $\beta_{\|0}$ and γ_0 are defined at the beginning of the interaction region, and ω is the angular frequency of the electromagnetic wave. Applying these conditions to Equation (2.11) yields

$$\frac{\partial w}{\partial Z} = \frac{e}{(m_e c)^2 \omega}\frac{\beta_{\|0}}{\gamma\gamma_0\beta_\|}\mathbf{p}\cdot\mathbf{E}. \tag{2.13}$$

In order to distinguish the magnitude and phase of the transverse momentum

of the electron and electric field, we can write these quantities in complex notation, $\mathbf{p} = p_x + ip_y = p_+ = |p_+|e^{i\alpha}$ and $\mathbf{E} = E_x + iE_y = E_+ = |E_+|e^{i(wt+\psi)}$. The angular term α for the electron's momentum is defined at the center of gyration for the electron which is at a radius R_e as seen in Figure 2-5. Now we can express the energy in terms of the real part of our complex variables

$$\frac{\partial w}{\partial Z} = \frac{e}{(m_e c)^2 \omega} \frac{\beta_{\parallel 0}}{\gamma \gamma_0 \beta_\parallel} Re(p_+^* E_+). \tag{2.14}$$

By taking equation (2.12) and considering the complex transverse momentum $|p_+|e^{i\alpha}$ we find that $\frac{\partial \mathbf{p}}{\partial t} = e^{i\alpha}\left(\frac{\partial |p_+|}{\partial t} + |p_+| i \frac{\partial \alpha}{\partial t}\right)$. Dividing by $e^{i\alpha}$ and solving for the imaginary part provides an equation that describes the change in phase with position for the momentum of the electron

$$\frac{\partial \alpha}{\partial Z} = \frac{\beta_{\parallel 0} \omega_c}{\beta_\parallel \omega} - \frac{e\beta_{\parallel 0}}{\omega \beta_\parallel |p_+|} Im(p_+^* E_+), \tag{2.15}$$

where $\omega_c = eB_0/m_e c\gamma$ is the cyclotron resonant frequency. The traditional configuration for a gyrotron consists of a cylindrical interaction region with a down-taper leading towards the electron gun and an up-taper facing the electron beam collector and the output window for the microwave signal. With this resonant configuration, the dominant contribution to the Q-factor will be the diffractive $Q = Q_D$. This diffractive Q is large enough that we can write a fixed expression for the field distribution $f(z) = e^{-(k_\parallel z)^2}$ which is a valid assumption for our configuration. The electric field in the transverse direction is identical to the TE_{mp} modes for a cylindrical waveguide along with a variation in the amplitude in the z direction. The fields are

$$\mathbf{E} = (E_R \hat{R} + E_{\phi_0} \hat{\phi}_0) e^{i(wt+\psi)},$$

$$E_R = i(m/k_\perp R) E_0 f(z) J_m(k_\perp R) e^{-im\phi_0},$$

$$E_{\phi_0} = E_0 f(z) J'_m(k_\perp R) e^{-im\phi_0},$$

where $k_\perp = \nu_{mp}/r_0$ and $w \approx n w_c$. These field expressions are written in the coordinate

frame (R, ϕ_0) which is centered in the middle of the solenoid. As stated previously, the complex expression for momentum considers the phase of the electron as it rotates about its center of gyration. Therefore, we also need our field expression to be centered around the same point. Haldar and Beck were able to convert from a reference frame in the center of the cavity to the center of the orbit for the electron using Graf's formula for Bessel functions [23]. This produces a series solution, but only one term will interact in a coherent fashion with the n^{th} order resonance. This allows us to express the fields as

$$\mathbf{E} = (E_{rn}\hat{r} + E_{\phi n}\hat{\phi})e^{i(wt+\psi)},$$

$$E_{rn} = i(n/k_\perp r)E_0 f(z)J_{m\pm n}(k_\perp R_e)J_n(k \perp r)e^{-im\phi_0}e^{-in(\phi-\phi_0)},$$

$$E_{\phi n} = E_0 f(z)J_{m\pm n}(k_\perp R_e)J'_n(k_\perp r)e^{-im\phi_0}e^{-in(\phi-\phi_0)}.$$

In order to evaluate Equations (2.14) and (2.15) we need the complex expression $E_+ = E_x + iE_y = Re(E_{rn}e^{i(wt+\psi)})e^{i\phi} + Re(E_{\phi n}e^{i(wt+\psi)})ie^{i\phi}$. Which gives

$$E_+ = -E_r \sin[\omega t - n\phi + \psi - (m-n)\phi_0]e^{i\phi} + E_\phi \cos[\omega t - n\phi + \psi - (m-n)\phi_0]ie^{i\phi},$$

where $E_r = |E_{rn}|$ and $E_\phi = |E_{\phi n}|$. If we set $\theta = \omega t - n\phi$, the complex expression becomes

$$E_+ = -E_r \sin[\theta + \psi - (m-n)\phi_0]e^{i\phi} + E_\phi \cos[\theta + \psi - (m-n)\phi_0]ie^{i\phi},$$

since ϕ is the angular position of the electron from its gyrocenter, it is related to the angular phase of its momentum by $\alpha = \phi + \pi/2$, because the position vector is orthogonal to the velocity vector for the electron. This changes the field expression to

$$E_+ = E_r \sin[\theta + \psi - (m-n)\phi_0]ie^{i\alpha} + E_\phi \cos[\theta + \psi - (m-n)\phi_0]e^{i\alpha},$$

and allows us to evaluate Equations (2.14) and (2.15) quite simply

$$\frac{\partial w}{\partial Z} = \frac{e}{\gamma_0 m_e c w} p'_\perp E_\phi \cos[\theta + \psi - (m-n)\phi_0], \tag{2.16}$$

$$\frac{\partial\theta}{\partial Z} = \delta_0 - w - \frac{ne}{\gamma_0 m_e c w}\frac{(1-w)}{p'_\perp}E_r \sin[\theta + \psi - (m-n)\phi_0], \tag{2.17}$$

where $\delta_0 = 1 - \omega_{c0}/\omega$, $\omega_{c0} = eB/m_e c\gamma_0$ and $p'_\perp = (|p_+|/\gamma_0 m_e c) = (\beta_{\perp 0}^2 - 2w + w^2)^{1/2}$. The value of δ_0 is equivalent to the detuning of the magnetic field as it relates to the ratio of the initial cyclotron resonance frequency and the frequency of the electromagnetic wave. Conveniently, we can set $\psi - (m-n)\phi_0 = \pi/2$ because there is no axial bunching, and the electrons at the input have a random phase about their gyrocenter, which further reduces our equations to

$$\frac{\partial w}{\partial Z} = \frac{E_\phi}{nB_0}p'_\perp \sin\theta, \tag{2.18}$$

$$\frac{\partial\theta}{\partial Z} = \delta_0 - w - \frac{E_r}{B_0}\frac{(1-w)}{p'_\perp}\cos\theta. \tag{2.19}$$

It is interesting to note that the radial electric field changes the energy of the electron and the azimuthal electric field affects the phase. In both cases, this affects the phase bunching of the electrons. It is convenient to rescale our normalized variables by

$$u \equiv \frac{2w}{\beta_{\perp 0}^2} = \frac{2}{\beta_{\perp 0}^2}(1 - \frac{\gamma}{\gamma_0}),$$

$$\zeta \equiv \frac{\beta_{\perp 0}^2}{2}Z = \pi\frac{\beta_{\perp 0}^2}{\beta_{\parallel 0}}\frac{z}{\lambda},$$

and normalize our fields with

$$F \equiv \frac{E_0}{B_0}\beta_{\perp 0}^{n-4}\frac{n^{n-1}}{n!2^{n-1}}J_{m\pm n}(k_\perp R_e).$$

It is also possible to make the approximation

$$k_\perp r \approx n\frac{\gamma B_\perp}{\gamma_0} = n\beta_{\perp 0}(1 - \frac{2w - w^2}{\beta_{\perp 0}^2})^{1/2} = np'_\perp.$$

These renormalizations and the approximation alter equations (2.18) and (2.19) to the form

$$\frac{\partial u}{\partial\zeta} = 2\left(\frac{2^n n!}{n^n\beta_{\perp 0}^{n-1}}\right)Ff(\zeta)\frac{p'_\perp}{\beta_{\perp 0}}J'_n(np'_\perp)\sin\theta, \tag{2.20}$$

$$\frac{\partial\theta}{\partial\zeta} = \Delta - u - n\left(\frac{2^n n!}{n^n \beta_{\perp 0}^{n-1}}\right) F f(\zeta) \frac{\beta_{\perp 0}(1-\beta_{\perp 0}^2 u/2)}{{p'_\perp}^2} J'_n(np'_\perp)\cos\theta, \tag{2.21}$$

where $\Delta \equiv 2\delta_0\beta_{\perp 0}^2$. We allow the normalization F for the field to be very complicated because under the condition that $\beta_{\perp 0}^2/2 \ll 1$, then $p'_\perp \approx (\beta_{\perp 0}^2 - 2w)^{1/2} = \beta_{\perp 0}(1-u)^{1/2}$. This condition permits a small argument expansion on the remaining Bessel function $J'_n(x) = \frac{n^n}{2^n n!}x^{n-1}$. If we apply this expansion we can rewrite our differential equations as

$$\frac{\partial u}{\partial\zeta} = 2Ff(\zeta)(1-u)^{n/2}\sin\theta, \tag{2.22}$$

$$\frac{\partial\theta}{\partial\zeta} = \Delta - u - nFf(\zeta)(1-u)^{n/2-1}\cos\theta. \tag{2.23}$$

Finally, we can define our cavity length L by $k_\parallel = 2/L$ and rewrite the axial field profile from $f(z) = e^{-(k_\parallel z)^2}$ to $f(\zeta) = e^{-(2\zeta/\mu)^2}$, where $\mu \equiv \pi\frac{\beta_{\perp 0}^2}{\beta_{\parallel 0}}\frac{L}{\lambda}$. We have constructed the coupled differential nonlinear equations of motion for a gyrating electron interacting with an electromagnetic field. These equations which describe the normalized transferred energy and phase of the electron are only functions of three parameters: the normalized field strength F, cavity length μ and detuning of the magnetic field Δ. However, Equations (2.22) and (2.23) only track the amount of energy that a single electron surrenders to the electromagnetic mode. Therefore, we need to verify that for various input boundary conditions the electrons will act coherently. The energy spread for the electrons at the input is very small allowing the electrons to have the same gyration frequency, but the phase around the gyrocenter is completely random ($\theta_0 = 0 \rightarrow 2\pi$). To calculate the actual efficiency of energy conversion for the device, we have to make sure that the stimulated emission is coherent for all of the electrons. This efficiency can be calculated by averaging over initial boundary conditions $\eta_\perp = < u(\zeta_{out}) >_{\theta_0}$.

2.4.2 Analysis

The efficiency analysis for the conversion of energy from kinetic electron energy to electromagnetic radiation was performed by using a fourth-order Runge-Kutta algo-

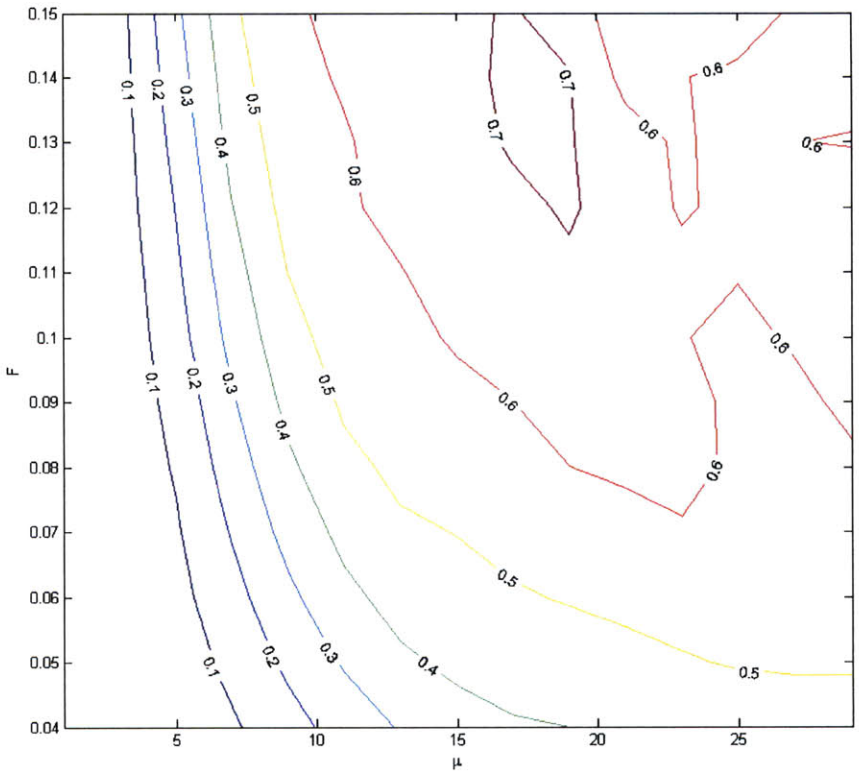

Figure 2-6: Contour plot for efficiency of the 1^{st} harmonic interaction between a cavity with normalized field strength, F, and interaction length, μ.

rithm and averaging the results for 32 electrons with uniform spacing in initial phase. For clarity the results are shown as contour plots with variables F and μ and optimized for Δ. These plots are shown in this form because Δ is often the easiest parameter to vary as the magnet can be charged to the desired strength. The spatial limits for the calculation were set at $\zeta = -\sqrt{3}\mu/2$ to $\sqrt{3}\mu/2$ and this is the commonly accepted cutoff point for the electric field of a tapered gyrotron oscillator.

In Figure 2-6, the contour plot for efficiency as a function of F and μ is shown for the first harmonic, and Figure 2-7 shows the contour plot for the second harmonic. It is possible that there are other peaks in efficiency for larger values of F and μ, but it is often desirable to operate at the smallest values of F and μ. This is because the longer the cavity, the more expensive the solenoidal magnet, and the larger the

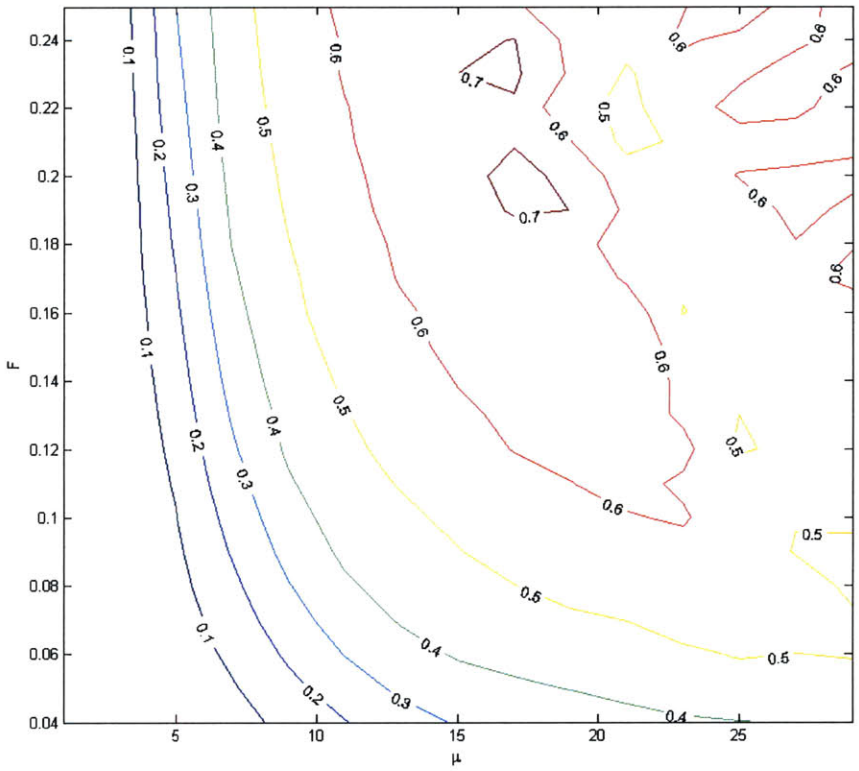

Figure 2-7: Contour plot for efficiency of the 2^{nd} harmonic interaction between a cavity with normalized field strength, F, and length, μ.

F, the greater current the electron gun must provide. Through power conservation, one can show that $F = \eta_{\perp}^2 I$, where I is the normalized current. This is the balance equation that specifies the current the electron gun must supply to the gyrotron. A direct expression for the actual current can be found, but that is beyond the scope of this thesis.

It is also possible to show how the average efficiency changes as the electrons progress through the cavity, as shown in Figure 2-8. It should be noted that the peak efficiencies for the first harmonic $\eta_{\perp_1} = 0.72$ and the second harmonic $\eta_{\perp_2} = 0.71$ are in excellent agreement with published values [17, 37, 50].

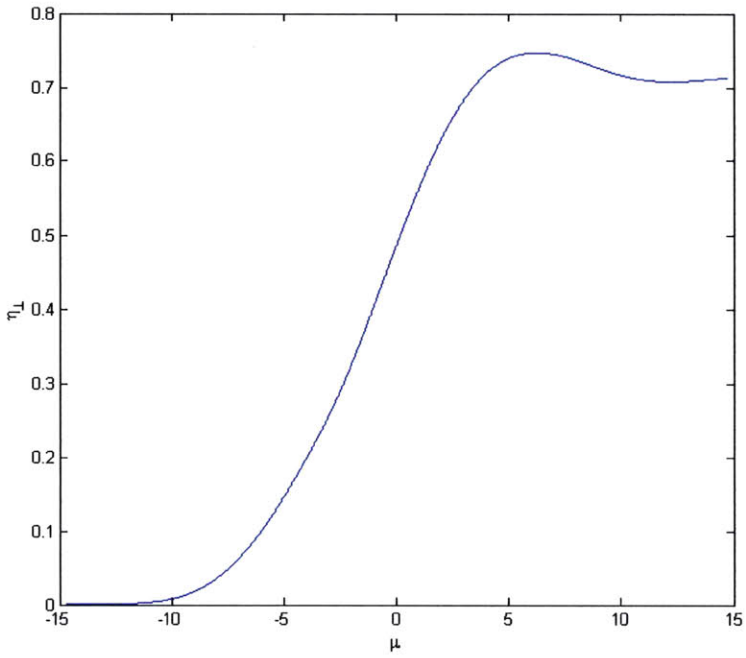

Figure 2-8: The fraction of electron energy that is extracted from the beam, averaged over 32 initial phases, as it passes through the cavity.

2.5 Quantum Mechanical Approach for Gyrotron Oscillators

In order to verify that stimulated emission can occur for gyrating electrons, we must consider their behavior on a quantum mechanical level. Landau showed [33, 27] that an electron moving perpendicularly to the magnetic field is a simple harmonic oscillator with energy levels $W_i = (i + \frac{1}{2})\hbar\omega_0$. With the relativistic treatment of the relativistic Schrödinger equation [40], the result is altered to

$$W_i = m_0c^2[1 + 2(i + \frac{1}{2})\hbar\omega_0/m_0c^2]^{1/2} - m_0c^2. \tag{2.24}$$

Therefore, with some small approximations, the transition between two states $i+1$ and i will emit a photon of frequency

$$\omega_{i,i+1} = (W_{i+1} - W_i)/\hbar = m_0c^2/\hbar[[1 + (i + \frac{3}{2})\hbar\omega_0/m_0c^2 + \frac{1}{2}(i^2 + 3i + 9/4)(\hbar\omega_0/m_0c^2)^2]$$
$$+[1 + (i + \frac{1}{2})\hbar\omega_0/m_0c^2 + \frac{1}{2}(i^2 + i + 1/4)(\hbar\omega_0/m_0c^2)^2]]),$$

$$\omega_{i,i+1} = \omega_0(1 - i\hbar\omega_0/m_0c^2). \tag{2.25}$$

If our system of N_i electrons is placed in a alternating electric field it will undergo transitions $\omega_{i,i+1}$ and $\omega_{i,i-1}$. This will produce a net power transfer of

$$P_i = N_i\hbar(\omega_{i,i+1}w_{i,i+1} - \omega_{i,i-1}w_{i,i-1}). \tag{2.26}$$

We need to compute the transition probability $w_{i,i+1}$ in order to find an expression for power transfer. The transition probability is given as $w_{i,i+1} = \hbar^{-2}E^2(\mu_{i,i+1})^2g(\omega)$ and $\mu_{i,i+1} = e[(i+1)\hbar/2m_0\omega_0]^{1/2}$ [40]. If we assume a small collision frequency $1/\tau$ the response can be assumed as Lorentzian where $g(\omega) = \tau/[1 + (\omega_{i,i+1} - \omega)^2\tau^2]$.

Solving for the transfer of power, we find

$$P_i/[N_i(e^2\tau/m_0)(E^2/2) = \Phi = \frac{(1 - i\alpha)(i+1)}{1 + (\omega_{i,i+1} - \omega)^2\tau^2} - \frac{(1 - (i-1)\alpha)i}{1 + (\omega_{i,i-1} - \omega)^2\tau^2}, \tag{2.27}$$

where Φ is the normalized power transfer, $\alpha = \hbar\omega_0/m_0c^2$. It is convenient to define a variable $x = (\omega_{i,i+1} - \omega)\tau$ and manipulate the expression (neglecting higher order terms in α) until the normalized power transfer becomes

$$\Phi(x) = \frac{1}{1 + x^2} + 2Q\frac{Wx}{m_oc^2(1 + x^2)^2}, \tag{2.28}$$

where W is the kinetic energy, $Q = \omega_0\tau$.

Equation (2.28) is plotted in Figure 2-9 for two cases where we have a relativistic electron and a nonrelativistic one. Several major observations can be made from this plot, most importantly that only in the relativistic case, where the energy levels of

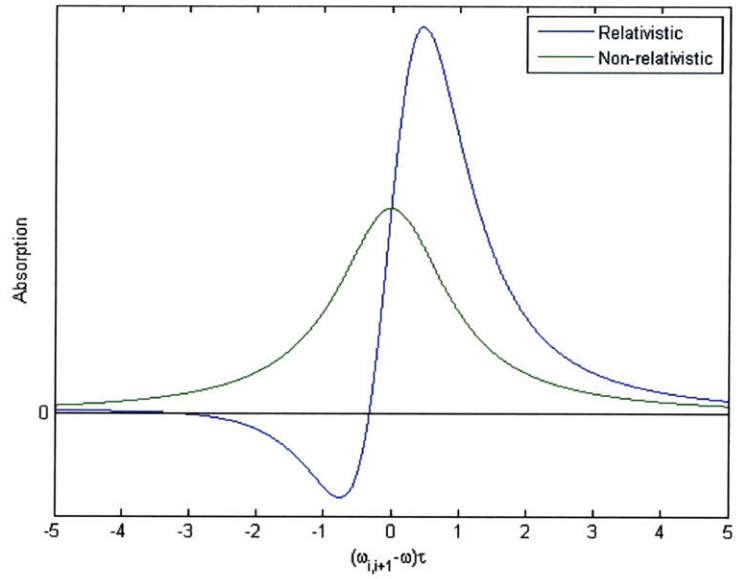

Figure 2-9: Stimulated emission of an electron in a magnetic field with relativistic and nonrelativistic treatment.

the gyrating electron become a function of the energy of the electron, can stimulated emission produce an energy gain for the electromagnetic field. Secondly, the frequency of the electromagnetic wave that we stimulate the system with must be slightly higher than the gyrofrequency of the electron, and as the energy of the electron decreases its gyrofrequency will increase until it begins absorbing energy. There is one other major finding that should be noted. Unlike a laser system where the excited state provides only one photon when it undergoes stimulated emission, a gyrotron that has very energetic electrons has a broader emission line width and can emit multiple photons as they pass through the cavity. This greatly increases the output power that can be achieved while maintaining an efficient system. Many of these findings are similar to the results observed with the electromagnetic treatment derived in Section 2.4. However, getting absolute efficiency values and design parameters is much more difficult with the quantum mechanical model and forces us to rely on the nonlinear single particle treatment in most cases.

2.6 Theory of Gyrotron Traveling Wave Tubes

Similar to the method described previously for gyrotron oscillators, tracking single particle behavior and averaging over a group of particles with a uniform phase distribution leads to a set of self-consistent non-linear equations that can describe the amplification process in a gyro-TWT. Excluding space charge effects, this method developed by Yulpatov [49] and later generalized by Nusinovich et al. [38] can also be simplified to produce a linear growth rate that is relatively easy to calculate. The equations of motion for an electron and the field amplitude are given by:

$$\frac{\partial \dot{w}}{\partial z'} = -2\frac{(1-w)^{s/2}}{1-bw}\mathrm{Re}\left\{F' e^{-i\bar{\theta}}\right\} \tag{2.29}$$

$$\frac{\partial \dot{\bar{\theta}}}{\partial z'} = \frac{1}{1-bw}\left\{-\bar{\Delta} + \bar{\mu}w + \frac{s}{(1-w)^{1-s/2}}\mathrm{Im}\left\{F' e^{-i\bar{\theta}}\right\}\right\} \tag{2.30}$$

$$\frac{\partial \dot{F}}{\partial z'} = -I_0'\frac{1}{2\pi}\int_0^{2\pi}\frac{(1-w)^{s/2}}{1-bw}J_n'(\xi)e^{-i\bar{\theta}}d\bar{\theta}_0 \tag{2.31}$$

where w is the normalized electron energy, $\bar{\theta}$ is the normalized electron phase, F is the normalized field amplitude, I_0' is the normalized current, $z' = kz$ is the normalized position, k is the wavenumber, s is the cyclotron harmonic and we define the normalized parameters

$$\begin{aligned}
b &= \frac{h\beta_{t0}^2}{2\beta_{z0}(1-h\beta_{z0})} \\
\bar{\mu} &= \frac{\beta_{t0}^2}{2\beta_{z0}}\frac{1-h^2}{1-h\beta_{z0}} \\
\bar{\Delta} &= \frac{1}{\beta_{z0}}\left(1 - s\frac{\mu}{\gamma} - h\beta_{z0}\right) \\
\mu &= \frac{eB_0}{m_{e0}\omega} \\
h &= k_z/k.
\end{aligned}$$

Additionally, we note that k_z is the axial wavenumber, $\beta_{z0} = \frac{v_{z0}}{c}$, v_{z0} is the initial

axial electron velocity, $\beta_{t0} = \frac{v_{t0}}{c}$, v_{t0} is the initial transverse electron velocity, γ is the relativistic mass factor, e is the electron charge, m_{e0} is the electron mass and B_0 is DC axial the magnetic field. In order to relate the normalized field amplitude to the waveguide modes

$$\vec{E} = \mathrm{Re}\left[A\vec{E}_s(r_t)e^{i(\omega t - k_z z)}\right] \tag{2.32}$$

$$\vec{H} = \mathrm{Re}\left[A\vec{H}_s(r_t)e^{i(\omega t - k_z z)}\right] \tag{2.33}$$

we need the relationship

$$F = \frac{\mu_0 c}{\kappa}\frac{1 - h\beta_{z0}}{\gamma_0\beta_{t0}\beta_{z0}}\frac{1}{2^s(s-1)!}\left(\frac{\kappa p'_{t0}}{\mu}\right)^{s-1} A' L_s(X,Y) \tag{2.34}$$

$$A' = \frac{eA}{m_{e0}c\omega} \tag{2.35}$$

where $\kappa = k_t/k$, k_t is the transverse wavenumber $p'_{t0} = \frac{p_{t0}}{m_{e0}c}$, p_{t0} is the initial transverse momentum. The normalized electron energy and phase are defined as

$$w = \frac{2(1 - h\beta_{z0})}{\beta_{t0}^2}\frac{\gamma_0 - \gamma}{\gamma} \tag{2.36}$$

$$\theta = s\Theta - (\omega t - k_z z) \tag{2.37}$$

$$\Theta = \mu\int_0^z p_z^{-1} dz' + \phi \tag{2.38}$$

where p_z is the axial momentum and ϕ defines the x and y momentum of the particle ($p_x = -p_\perp \sin(\phi)$ and $p_x = p_\perp \cos(\phi)$) at the entrance of the circuit. The current I in Amps is given by

$$I'_0 = \frac{e|I|}{N_s}\frac{2\mu_0^2}{k_t^2 m_{e0}\gamma_0}\frac{1 - h\beta_{z0}}{\beta_{z0}^2}\left(\frac{1}{2^s(s-1)!}\right)^2\left(\frac{\kappa p'_{t0}}{\mu}\right)^{2(s-1)}|L_s|^2 \tag{2.39}$$

L_s is the Form Factor of a waveguide mode, describing its interaction with an electron beam, and N_s is the Norm of a waveguide mode, accounting for the power in any given

transverse cross section.

$$L_s = \left[\frac{k}{k_\perp}\left(\frac{\partial}{\partial \mathbf{X}} + i\frac{1}{|s|}\frac{\partial}{\partial \mathbf{Y}}\right)\right]^{|s|} \Psi(\mathbf{X}, \mathbf{Y}) \tag{2.40}$$

$$N_s = \frac{c}{4\pi}\int \{\mathbf{E}_s \times \mathbf{H}_s^* - \mathbf{H}_s \times \mathbf{E}_s^*\} \cdot \mathbf{z}_0 dS_\perp \tag{2.41}$$

where X and Y are the transverse coordinates of the electron guiding center. It is very useful to define a coupling factor

$$\frac{|L_s^2|}{N_s} \equiv \text{Coupling Factor}, \tag{2.42}$$

which can be calculated in HFSS for different modes and beam radii to compare the strength of the interaction. If we take the Equations (2.29)-(2.31), it is possible to linearize them in the small signal regime and derive a dispersion relation that will give the growth rate for a mode:

$$\Gamma^3 - \bar{\Delta}\Gamma^2 - I_0'(n-b)\Gamma + (\bar{\mu} - \bar{\Delta}b)I_0' = 0. \tag{2.43}$$

The three roots of Γ correspond to the growth rates of the three waves that will couple with the electron beam. The three waves will propagate as $e^{i\Gamma kz}$.

2.7 Short Pulse Propagation and Amplification

The pulse in the interaction circuit is expected to suffer from two dispersive effects: waveguide dispersion from operating near the cutoff frequency of the interaction circuit and gain dispersion from the bandwidth-limited nature of the amplifier. Waveguide dispersion occurs because of the frequency dependence of the group velocity. It has a significant effect because the frequency of the pulse is very close to the cutoff of the waveguide ($k_z \ll k$). A waveguide filled with an active medium (the electron beam in this case) shows an additional dispersive effect due to that medium, especially near cyclotron resonance. This dispersive effect, referred to as gain dispersion,

is observed for pulse lengths with a spectral width on the order of or greater than the bandwidth of the Gyro-amplifier.

In order to accurately describe the propagation of a pulse in a gyro-TWT we will need to derive a non-stationary equation for the excitation of the waveguide. This derivation is similar to the work of Kovlev et al. [32] which derives the non-stationary equations for the excitation of waveguides. Let us define the excitation current $\mathbf{j}_R$ and the perturbed electric field $\mathbf{E}_R$ and magnetic field $\mathbf{H}_R$:

$$\mathbf{j}_R = \mathbf{j}(x, y, z, t)e^{-i\omega t} \tag{2.44}$$

$$\mathbf{E}_R = \mathbf{E}(x, y, z, t)e^{-i\omega t} \tag{2.45}$$

$$\mathbf{H}_R = \mathbf{H}(x, y, z, t)e^{-i\omega t} \tag{2.46}$$

Maxwell's equations for this system take the form

$$\nabla \times \mathbf{H}_R = \frac{\partial \mathbf{D}_R}{\partial t} + \mathbf{j} \tag{2.47}$$

$$\nabla \times \mathbf{E}_R = -\frac{\partial \mathbf{B}_R}{\partial t} \tag{2.48}$$

where we define the electric and magnetic flux as

$$\mathbf{D}_R = \int \epsilon(\hat{\omega})\mathbf{E}_R(z, \hat{\omega})e^{-i\hat{\omega}t}d\hat{\omega} \tag{2.49}$$

$$\mathbf{B}_R = \int \mu(\hat{\omega})\mathbf{H}_R(z, \hat{\omega})e^{-i\hat{\omega}t}d\hat{\omega}. \tag{2.50}$$

This allows us to have a permittivity and permeability that are a function of frequency. We consider only one forward and backward propagating waveguide mode for this system, given that the gyro-TWT is highly lossy for other modes and the electron beam parameters are tuned such that it does not interact strongly with other modes. The two modes will be identified as

$$\mathbf{E} = A_{\pm}\mathbf{E}_{\pm} \tag{2.51}$$

$$\mathbf{H} = A_{\pm}\mathbf{H}_{\pm} \tag{2.52}$$

where A is the instantaneous amplitude of the pulse envelope. The permittivity $\epsilon(\hat{\omega})$ and permeability $\mu(\hat{\omega})$ can be expanded as a series about a frequency ω, in our case the frequency of the pulse,

$$\epsilon(\hat{\omega}) = \sum_{n=0}^{\infty} \frac{1}{n!} \frac{d^n \epsilon}{d\omega^n} (\hat{\omega} - \omega)^n \tag{2.53}$$

$$\mu(\hat{\omega}) = \sum_{n=0}^{\infty} \frac{1}{n!} \frac{d^n \mu}{d\omega^n} (\hat{\omega} - \omega)^n. \tag{2.54}$$

Using the above definitions Equations (2.47) and (2.48) can be re-written as

$$\nabla \times \mathbf{E} = i\omega\mu\mathbf{H} + i \sum_{n=1}^{\infty} \frac{i^n}{n!} \left(\omega \frac{d^n \mu}{d\omega^n} + n \frac{d^{n-1}\mu}{d\omega^{n-1}} \right) \frac{\partial^n \mathbf{H}}{\partial t^n} \tag{2.55}$$

$$\nabla \times \mathbf{H} = -i\omega\epsilon\mathbf{E} - i \sum_{n=1}^{\infty} \frac{i^n}{n!} \left(\omega \frac{d^n \epsilon}{d\omega^n} + n \frac{d^{n-1}\epsilon}{d\omega^{n-1}} \right) \frac{\partial^n \mathbf{E}}{\partial t^n} + \mathbf{j}. \tag{2.56}$$

Using vector identities [37] defined as

$$\begin{aligned} \nabla \times A_{\pm}\mathbf{H}_{\pm} &= A_{\pm}(\nabla \times \mathbf{H}_{\pm}) - \mathbf{H}_{\pm} \times (\nabla A_{\pm}) && (2.57) \\ &= -A_{\pm} i\omega\epsilon \mathbf{E}_{\pm} + \frac{\partial A_{\pm}}{\partial z}(\hat{z} \times \mathbf{H}_{\pm}) && (2.58) \end{aligned}$$

$$\begin{aligned} \nabla \times A_{\pm}\mathbf{E}_{\pm} &= A_{\pm}(\nabla \times \mathbf{E}_{\pm}) - \mathbf{E}_{\pm} \times (\nabla A_{\pm}) && (2.59) \\ &= A_{\pm} i\omega\mu \mathbf{H}_{\pm} + \frac{\partial A_{\pm}}{\partial z}(\hat{z} \times \mathbf{E}_{\pm}) && (2.60) \end{aligned}$$

we simplify further to

$$\frac{\partial A_{\pm}}{\partial z}(\hat{z} \times \mathbf{E}_{\pm}) = i \sum_{n=1}^{\infty} \frac{i^n}{n!} \left(\omega \frac{d^n \mu}{d\omega^n} + n \frac{d^{n-1}\mu}{d\omega^{n-1}} \right) \frac{\partial^n \mathbf{H}}{\partial t^n} \tag{2.61}$$

$$\frac{\partial A_{\pm}}{\partial z}(\hat{z} \times \mathbf{H}_{\pm}) = -i \sum_{n=1}^{\infty} \frac{i^n}{n!} \left(\omega \frac{d^n \epsilon}{d\omega^n} + n \frac{d^{n-1}\epsilon}{d\omega^{n-1}} \right) \frac{\partial^n \mathbf{E}}{\partial t^n} + \mathbf{j}. \tag{2.62}$$

Multiply Equation (2.61) by $\mathbf{H}_-$ and Equation (2.62) by $\mathbf{E}_-$ and add them together:

$$\begin{aligned}\frac{\partial A_+}{\partial z} \quad & (\mathbf{E}_- \times \mathbf{H}_+ - \mathbf{H}_- \times \mathbf{E}_+)\hat{z} + \frac{\partial A_-}{\partial z}(\mathbf{E}_- \times \mathbf{H}_- - \mathbf{H}_- \times \mathbf{E}_-)\hat{z} \\ = \; & i\sum_{n=1}^{\infty}\frac{i^n}{n!}\left(\omega\frac{d^n\mu}{d\omega^n} + n\frac{d^{n-1}\mu}{d\omega^{n-1}}\right)\mathbf{H}_-\frac{\partial^n A_+\mathbf{H}_+}{\partial t^n} \\ & +i\sum_{n=1}^{\infty}\frac{i^n}{n!}\left(\omega\frac{d^n\mu}{d\omega^n} + n\frac{d^{n-1}\mu}{d\omega^{n-1}}\right)\mathbf{H}_-\frac{\partial^n A_-\mathbf{H}_-}{\partial t^n} \\ & -i\sum_{n=1}^{\infty}\frac{i^n}{n!}\left(\omega\frac{d^n\epsilon}{d\omega^n} + n\frac{d^{n-1}\epsilon}{d\omega^{n-1}}\right)\mathbf{E}_-\frac{\partial^n A_+\mathbf{E}_+}{\partial t^n} \\ & -i\sum_{n=1}^{\infty}\frac{i^n}{n!}\left(\omega\frac{d^n\epsilon}{d\omega^n} + n\frac{d^{n-1}\epsilon}{d\omega^{n-1}}\right)\mathbf{E}_-\frac{\partial^n A_-\mathbf{E}_-}{\partial t^n} + \mathbf{j}\mathbf{E}_- \end{aligned} \tag{2.63}$$

Integrating over the surface of the waveguide [32, 37] we define the Norm factor for the waveguide to be

$$\int \{\mathbf{H}_\nu \times \mathbf{E}_{-s} - \mathbf{H}_{-s} \times \mathbf{E}_\nu\} \cdot \hat{z} dS_\perp = N_s\delta_{s\nu}, \tag{2.64}$$

where $\delta_{s\nu}$ is 1 if $s = \nu$ and is 1 if $s \neq \nu$. We will consider the expansion Equation (2.63) n=1,2. And we note that

$$\int (-\mu\mathbf{H}_-\mathbf{H}_- + \epsilon\mathbf{E}_-\mathbf{E}_-)dS_\perp = 0. \tag{2.65}$$

We simplify Equation (2.63) as

$$\begin{aligned} N_s\frac{\partial A_+}{\partial z} \quad = \quad & \int (-\mu\mathbf{H}_-\mathbf{H}_+ + \epsilon\mathbf{E}_-\mathbf{E}_+)dS_\perp\frac{\partial A_+}{\partial t} \\ & +\frac{i}{2}\frac{d}{d\omega}\int (-\mu\mathbf{H}_-\mathbf{H}_+ + \epsilon\mathbf{E}_-\mathbf{E}_+)dS_\perp\frac{\partial^2 A_+}{\partial t^2} + \int \mathbf{j}\mathbf{E}_- dS_\perp \end{aligned} \tag{2.66}$$

If we use the following identities [32]

$$\frac{d}{d\omega}\mu\mathbf{H}_-\mathbf{H}_+ = \mathbf{H}_-\mathbf{H}_+\frac{d}{d\omega}\mu \tag{2.67}$$

$$\frac{d}{d\omega}\mathbf{H}_{\pm} = \mathbf{H}_{\pm}(\pm jz)\frac{dk}{d\omega} \tag{2.68}$$

$$N_s\frac{dk_z}{d\omega} = -\int(\epsilon\mathbf{E}_{-}\mathbf{E}_{+} - \mu\mathbf{H}_{-}\mathbf{H}_{+})dS_{\perp} \tag{2.69}$$

then Equation (2.66) becomes

$$N_s\frac{\partial A_{+}}{\partial z} = -N_s\frac{dk_z}{d\omega}\frac{\partial A_{+}}{\partial t} - \frac{i}{2}N_s\frac{d^2k_z}{d\omega^2}\frac{\partial^2 A_{+}}{\partial t^2} + \int \mathbf{j}\mathbf{E}_{-}dS_{\perp} \tag{2.70}$$

$$\frac{\partial A_{+}}{\partial z} + \frac{dk_z}{d\omega}\frac{\partial A_{+}}{\partial t} + \frac{i}{2}\frac{d^2k_z}{d\omega^2}\frac{\partial^2 A_{+}}{\partial t^2} = \frac{1}{N_s}\int \mathbf{j}\cdot\mathbf{E}^{*}dS_{\perp} \tag{2.71}$$

Here we have separated the mode's behavior into two parts; on the LHS are terms associated with propagation and the RHs is the interaction with the electron beam. This interaction is extremely complicated for the specific electron distribution in the case of gyro-TWTs. However, in [16] Chu shows that, for a continuous wave gyro-TWT, with small signal theory the beam's interaction with the field is linearly dependent on the axial field amplitude:

$$\frac{1}{N_s}\int \mathbf{j}\cdot\mathbf{E}^{*}dS_{\perp} = G(\omega)A_{+}. \tag{2.72}$$

In the linear regime the electron beam's interaction with the wave is only a function of the frequency of the wave. $G(\omega)$ could be determined theoretically from small signal theory as described in the previous section or it could be measured experimentally for a given operating point. The assumption of linear gain places some specific constraints on the system. The electrons must travel with an axial velocity (v_z) that is approximately equal to the group velocity (v_g) of the pulse. This requirement ensures that the bunched electrons will not become displaced from the pulse as it propagates down the circuit. This assumption falls apart if the pulse is severely broadened. Additionally, the gyro-TWT must not be operating in a saturated regime for Equation (2.72) to be true. If the group velocity and axial velocity of the electrons are not similar or the amplifier is operating in a saturated regime the electron's location and interaction with the pulse must be calculated instantaneously.

For a gyro-TWT operating in a linear regime a pulse's propagation through the interaction circuit can be described by

$$\frac{\partial A_+}{\partial z} + \frac{dk_z}{d\omega}\frac{\partial A_+}{\partial t} + \frac{i}{2}\frac{d^2k_z}{d\omega^2}\frac{\partial^2 A_+}{\partial t^2} = G(\omega)A_+ \tag{2.73}$$

Similar to optical systems [1, 25, 24], it is convenient to deal with the dispersion in the frequency domain, because of the pulse's inherent bandwidth and the frequency dependence of $G(\omega)$. Using the Fourier transform relationship:

$$[i(\omega - \bar{\omega_o})]^n A_+(z, \omega - \bar{\omega_o}) = F.T.\left[\frac{\partial^n}{\partial t^n}A_+(z,t)\right] \tag{2.74}$$

we transform to the frequency domain

$$\begin{aligned}\frac{\partial}{\partial z}A_+(z,\omega-\bar{\omega_o}) &= -\left[\frac{dk_z}{d\omega}(\omega-\bar{\omega_o}) + \frac{i}{2}\frac{d^2k_z}{d\omega^2}(\omega-\bar{\omega_o})^2\right]A_+(z,\omega-\bar{\omega_o}) \\ &\quad + G(\omega)A_+(z,\omega-\bar{\omega_o})\end{aligned} \tag{2.75}$$

$A_+(z, \omega - \bar{\omega_o})$ is the frequency spectrum of the pulse envelope. If we are interested not only in the envelope but in the instantaneous field, we can say:

$$a(z,\omega) = A_+(z,\omega-\bar{\omega_o})e^{-ik_z z} \tag{2.76}$$

$$\frac{\partial}{\partial z}a(z,\omega) = -i\left[k_z(\bar{\omega_o}) + \frac{dk_z}{d\omega}(\omega-\bar{\omega_o}) + \frac{1}{2}\frac{d^2k_z}{d\omega^2}(\omega-\bar{\omega_o})^2\right]a + G(\omega)a \tag{2.77}$$

The three terms with k_z are the first three terms for the expansion of $k_z(\omega)$, giving us our final result:

$$\frac{\partial}{\partial z}a(z,\omega) = -ik_z(\omega)a + G(\omega)a \tag{2.78}$$

To derive a simple algebraic expression describing the broadening of Gaussian pulses

we will revert to a temporal solution. First, we begin by expanding k_z and G

$$\frac{\partial}{\partial z}a(z,\omega) = -i\left[k_z(\bar{\omega_o}) + \frac{dk_z}{d\omega}(\omega-\bar{\omega_o}) + \frac{1}{2}\frac{d^2k_z}{d\omega^2}(\omega-\bar{\omega_o})^2\right]a + \left[G(\bar{\omega_o}) + \frac{dG}{d\omega}(\omega-\bar{\omega_o}) + \frac{1}{2}\frac{d^2G}{d\omega^2}(\omega-\bar{\omega_o})^2\right]a \quad (2.79)$$

redefine the frequency spectrum of the pulse envelope

$$a(z,\omega) = A'(z,\omega-\bar{\omega_o})e^{-ik_z z+Gz} \quad (2.80)$$

and invert our transform from Equation (2.74)

$$\frac{\partial}{\partial z}A' = -\frac{dk_z}{d\omega}\frac{\partial A'}{\partial t} + \frac{i}{2}\frac{d^2k_z}{d\omega^2}\frac{\partial^2 A'}{\partial t^2} - i\frac{dG}{d\omega}\frac{\partial A'}{\partial t} - \frac{1}{2}\frac{d^2G}{d\omega^2}\frac{\partial^2 A'}{\partial t^2}. \quad (2.81)$$

We can transform this equation to the moving frame of the pulse

$$\xi = z + \left(\frac{dk_z}{d\omega} + i\frac{dG}{d\omega}\right)t \quad (2.82)$$

$$\frac{\partial}{\partial \xi}A' = \left(\frac{i}{2}\frac{d^2k_z}{d\omega^2} - \frac{1}{2}\frac{d^2G}{d\omega^2}\right)\frac{\partial^2 A'}{\partial t^2} \quad (2.83)$$

We define a broadening term β''

$$\beta'' = \frac{d^2k_z}{d\omega^2} + i\frac{d^2G}{d\omega^2} \quad (2.84)$$

$$\frac{\partial}{\partial \xi}A' = \frac{i}{2}\beta''\frac{\partial^2 A'}{\partial t^2}. \quad (2.85)$$

The algebraic solution to this equation is known [24] for a Gaussian pulse. The output width can be approximated as

$$\tau_{out}^2 = \tau_{in}^2 + |\beta''|^2 l^2 \quad (2.86)$$

where l is the length of propagation. We note that $\frac{dk_z}{d\omega} = v_g$. If we define τ as the full width half max of the pulse we can simplify $\frac{d}{d\omega} \approx \Delta$, where Δ is the difference of the

operand measured at full width half max.

$$\tau_{out}^2 = \tau_{in}^2 + \left(\Delta\frac{1}{v_g} + \Delta\frac{dG}{d\omega}\right)^2 l^2. \tag{2.87}$$

2.8 Conclusion

A general explanation for the operation of electron cyclotron masers and gyro-TWTs has been presented. The bunching mechanism for both fast and slow waves in a streaming electron plasma was presented. The nonlinear theory of operation was derived, discussed and analyzed. Numerical simulations were performed that provided excellent agreement with published values. A quantum mechanical description of the energy levels of the electron was discussed. This approach shows that the medium is purely absorptive if it is fully nonrelativisitic. However, once the system is mildly relativistic the system will undergo stimulated emission if the frequency of the electromagnetic field is slightly greater than the gyration frequency of the electron. The dispersion relation for linear amplification in gyro-TWT was presented. The model for the amplification of short pulses in the linear regime of a gyro-TWT was derived from fundamental principles.

Chapter 3

250 GHz Gyro-TWT Design

3.1 Introduction

Studies have shown how the promise of high gain and high output power in gyro-TWTs is limited by the strong forward and backward wave gyrotron oscillations near the waveguide cut-off [4]. A scheme of distributed loading was demonstrated to suppress the gyrotron backward wave oscillations (gyro-BWO) and forward wave gyrotron oscillations near the waveguide cut-off using fundamental mode interaction circuits [13]. Operation in fundamental modes is not feasible at high frequencies, such as 250 GHz, where the radius of the interaction structure would be on the order of a fraction of a millimeter. This results in high ohmic losses that can lead to thermal damage and reduced gain. It also presents a significant challenge in transporting an electron beam over long distances (~30 cm) without causing beam interception on the waveguide walls. Operation in higher order modes poses its own problems with oscillations at lower order modes. To prevent these oscillations a mode selective interaction circuit with distributed loss that is easy to manufacture is highly desirable. The danger of oscillations from lower order modes is easily seen in Figure 3-1 where the dispersion relation for several modes in a cylindrical waveguide is plotted. One candidate mode for an amplifier at 250GHz would be the TE_{03}. However, when the electron beam line for a grazing condition is considered it becomes apparent that oscillations are possible where the beam intercepts with other modes. A forward wave

oscillation with the TE_{23} mode or a backward wave oscillation with the TE_{81} and TE_{42} modes are the most significant. Clever selection of electron beam parameters, the inclusion of severs or distributed loading can increase the start current for oscillations, but any realistic design must have an interaction circuit that directly addresses the presence of lower order modes.

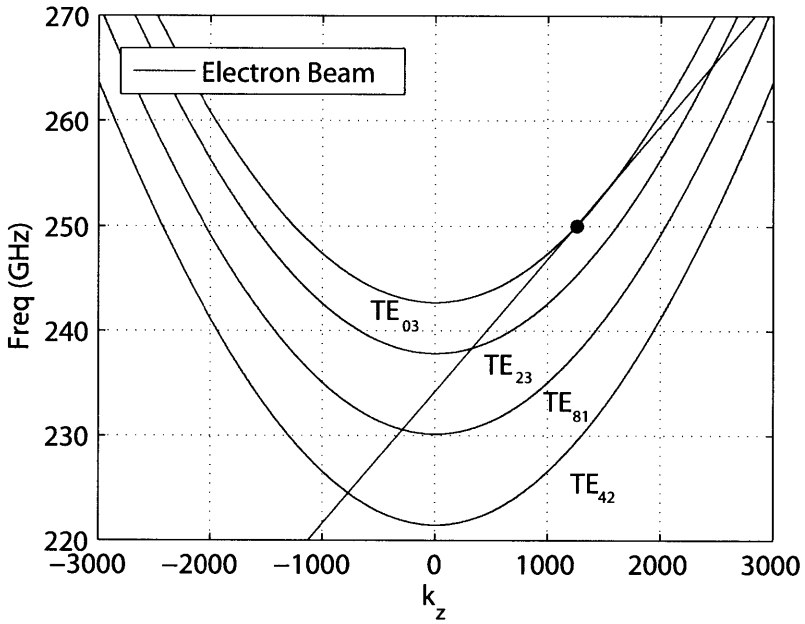

Figure 3-1: Dispersion relation for a circular waveguide with a 2 mm radius.

The design of a 250 GHz gyrotron traveling wave amplifier for nanosecond pulses with gain exceeding 50 dB that focuses on the presence of lower order modes is presented in this chapter. The amplifier uses a novel photonic band gap (PBG) interaction circuit with mode selective properties. The PBG interaction structure confines a TE_{03}-like mode with comparable interaction efficiency to a circular waveguide, while providing lower-order mode suppression and distributed loss along the entire interaction circuit. The design of the input coupler, output coupler and electron gun will also be discussed in this chapter.

3.2 Attenuation in Waveguides

In order for the gyro-amplifier to operate correctly self start oscillations, driven oscillations and BWOs must all be subdued. The traditional method for suppressing these oscillations consists of minimizing reflections in the amplifier circuit to lower the diffractive Q and placing severs (short sections of highly attenuating waveguide) to increase the start current for these oscillations. Both of these features are complicated to design and manufacture for very high frequency systems. Severs can also waste valuable space in the flat top of the magnetic field thereby decreasing the performance of the amplifier. An alternate approach is to design an interaction circuit that has an attenuation constant that is highly frequency dependent in such a way to prevent oscillations at lower frequency modes and near cutoff for the operational mode. Traditional waveguide circuits do have a frequency dependence in the attenuation constant especially near cutoff, but it is insufficient to suppress these oscillations. In a circular waveguide the electric and magnetic fields for TE_{nm} modes can be written as:

$$E_\rho = \frac{-i\omega\mu n}{k_c^2\rho} A\cos(n\phi)\mathbf{J}_n(k_c\rho)e^{-ik_z z},$$

$$E_\phi = \frac{i\omega\mu}{k_c} A\sin(n\phi)\mathbf{J}'_n(k_c\rho)e^{-ik_z z},$$

$$E_z = 0,$$

$$H_\rho = \frac{-ik_z}{k_c} A\sin(n\phi)\mathbf{J}'_n(k_c\rho)e^{-ik_z z},$$

$$H_\phi = \frac{-ik_z n}{k_c^2\rho} A\cos(n\phi)\mathbf{J}_n(k_c\rho)e^{-ik_z z},$$

$$H_z = A\sin(n\phi)\mathbf{J}_n(k_c\rho)e^{-ik_z z},$$

where $k_c = \nu_{nm}/a$, ν_{nm} is the mth root of the nth order Bessel function and a is the waveguide radius. In order to calculate the attenuation constant (α_c) we must find the power propagating down the waveguide (P_0) and the power dissipated on the conducting walls (P_l) of the waveguide. The power propagating down the waveguide

is found by integrating the Poynting vector over the cross sectional surface of the waveguide

$$P_0 = \frac{1}{2}\mathbf{Re}\left\{\int_{\rho=0}^{a}\int_{\phi=0}^{2\pi} \bar{E}\times\bar{H}^*\cdot\hat{z}\rho d\phi d\rho\right\} \tag{3.1}$$

where $\hat{z}$ is the direction of propagation. The dissipated power is found by integrating the surface current J_s on the surface of the waveguide at that cross section

$$P_l = \frac{R_s}{2}\int_{\phi=0}^{2\pi} |\bar{J}_s^2| a d\phi \tag{3.2}$$

where R_s is the surface resistivity and $|J_s|^2$ is given by the magnetic fields on the surface $[|H_\phi|^2 + |H_z|^2]$. Once P_0 and P_l are known the attenuation constant can be defined as

$$\alpha_c = \frac{P_l}{2P_o} \tag{3.3}$$

Due to the surface currents and the propagation constant k_z the attenuation constant is frequency dependent and mode dependent. For waveguides with complicated geometries like confocal or photonic band gap structures it is not possible to analytically calculate the attenuation constant because the fields of the mode are not well defined. One must use a numerical code, such as High Frequency Structure Simulator (HFSS), to observe how power propagates through the waveguide as a function of frequency. An ideal interaction circuit would confine the operating mode with limited loss in the amplification region and have an attenuation constant that is very high for modes that are not of interest. Mode selective circuits can be made in a variety of ways (dielectric loading, confocal, PBG, etc.) that often have a detrimental impact on the mode of interest as well as additional complexity in fabrication. Finding a balance is the key to developing a successful overmoded interaction circuit for a gyro-TWT.

3.3 Photonic Band Gaps

It is possible to create a large variety of photonic band gap structures in one, two and three dimensions that support TE, TM and TEM waves. A photonic band gap of interest for gyro-TWTs needs to support TE modes that will not diffract in the transverse direction with respect to the electron beam. Furthermore, if the circuit is to be overmoded then the lowest band gap for a given set of lattice constants should not extend to zero frequency. Taking these things into consideration we have selected a two dimensional triangular metallic lattice (Figure 3-2) for the gyro-TWT and it will be the only one discussed presently. We begin by defining the conductivity profile of the lattice as

$$\sigma\left(\vec{x}_\perp + \vec{T}_{mn}\right) = \sigma\left(\vec{x}_\perp\right) \tag{3.4}$$

$$\vec{T}_{mn} = \left(m + \frac{n}{2}\right) b\hat{e}_x + \frac{\sqrt{3}}{2} nb\hat{e}_y \tag{3.5}$$

where b is the lattice spacing, m and n are integers and $\vec{x}_\perp = x\hat{e}_x + y\hat{e}_y$.

We will define our fields as a function of $\vec{x}_\perp$, z, t. Due to the symmetry and linearity of the system we can assume that the axial wave number k_z and the frequency ω are fixed. We write the Helmholtz wave equation as

$$\vec{\nabla}_\perp^2 \psi\left(\vec{x}_\perp\right) = \left(k_z^2 - \frac{\omega^2}{c^2}\right) \psi\left(\vec{x}_\perp\right) \tag{3.6}$$

with the boundary condition

$$\frac{\partial \psi}{\partial \vec{n}}|_S = 0 \tag{3.7}$$

where $\vec{n}$ is the vector normal to the metallic surface S. The discrete array of metallic rods has a solution that can be written in Bloch form

$$\psi\left(\vec{x}_\perp + \vec{T}_{mn}\right) = \psi\left(\vec{x}_\perp\right) e^{i\vec{k}_\perp \cdot \vec{T}_{mn}} \tag{3.8}$$

where $\vec{k}_\perp = k_x\hat{e}_x + k_y\hat{e}_y$ is the transverse wave number, allowing us to solve the wave

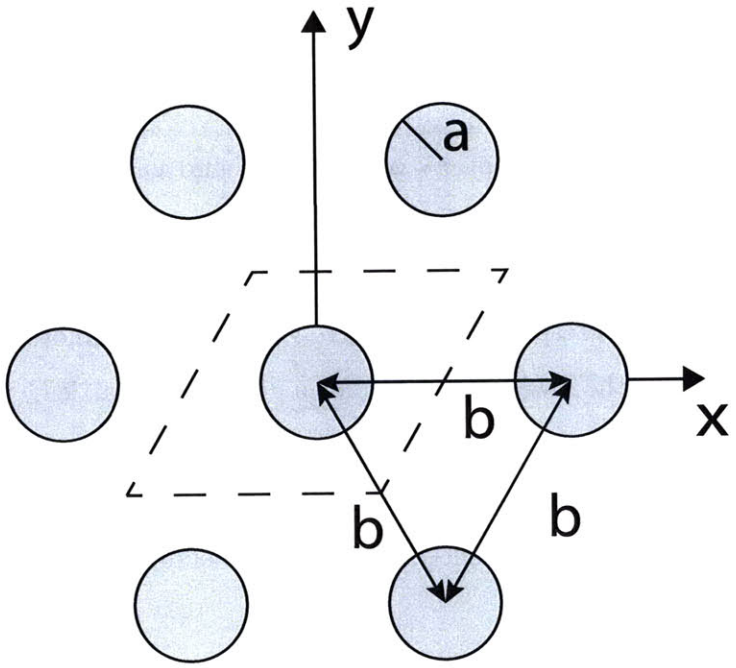

Figure 3-2: Triangular lattice of metallic rods. The fundamental unit cell is marked with a dashed line.

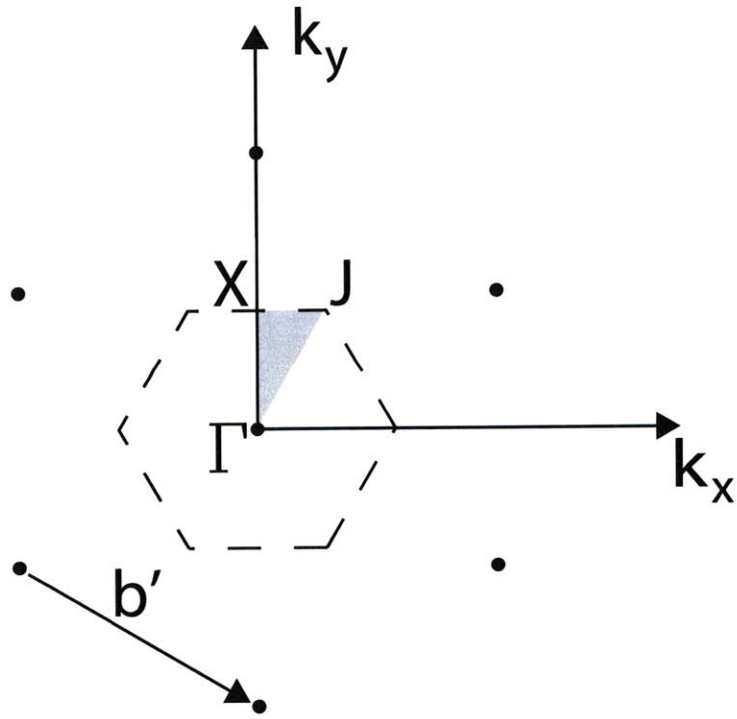

Figure 3-3: Reciprocal triangular lattice where $b' = \frac{4\pi}{\sqrt{3}b}$. The gray area is the irreducible Brillouin zone.

equation in the fundamental cell in Figure 3-2 given by

$$\left| x - \frac{y}{\sqrt{3}} \right| \leq \frac{b}{2}, |y| \leq \frac{\sqrt{3}}{4} b. \tag{3.9}$$

The discrete nature of the system also imposes periodic boundary conditions:

$$\psi\left(\frac{b}{2} + \frac{1}{\sqrt{3}}y, y\right) = e^{ik_x b}\psi\left(-\frac{b}{2} + \frac{1}{\sqrt{3}}y, y\right) \tag{3.10}$$

$$\psi\left(x, \frac{\sqrt{3}b}{4}\right) = e^{ik_x b/2 + ik_y\sqrt{3}b/2}\psi\left(x - \frac{b}{2}, -\frac{\sqrt{3}b}{4}\right). \tag{3.11}$$

Equation (3.8) imposes limits on the value of $\vec{k}_\perp$, shown as the Brillouin zone in Figure 3-3. The three special points Γ, X and J are at $\vec{k}_\perp = 0$, $\vec{k}_\perp = (2\pi/\sqrt{3}b)\hat{e}_y$ and $\vec{k}_\perp = (2\pi/\sqrt{3}b)(\hat{e}_x + 1/\sqrt{3}\hat{e}_y)$.

One possible method to solve the wave equation in the unit cell area is using HFSS [41]. By imposing the proper boundary conditions we can pre-select for TE modes and fully explore the possible k-space of the system. For any given $k_\perp$ there will be a corresponding phase advance across the unit cell. Perfect H boundaries are defined on the top and bottom of the unit cell to limit eigenmode solutions to TE modes. The wave number can be specified by creating a master/slave boundary as shown in Figure 3-4. The master/slave boundary defines the phase advance across the two orthogonal directions of the unit cell thereby specifying the wave number. For example, going from the Γ point to the X point, on Figure 3-3, k_x will always be zero, but $0 \leq k_y \leq 2\pi/\sqrt{3}b$. If we consider the periodic boundary conditions for this range of values, Equation (3.10) indicates that the phase shift $\phi_1 = 0$ from the master #1 to the slave #1 boundary and Equation (3.11) indicates there is a $0 \leq \phi_2 \leq \pi$ phase shift from the master #2 to the slave #2 boundaries in Figure 3-4. Performing the same analysis from X to J and J to Γ will complete the exploration of the Brillouin zone. The necessary values of k_x and k_y and the corresponding phases of the master/slave boundaries are listed in Table 3.1.

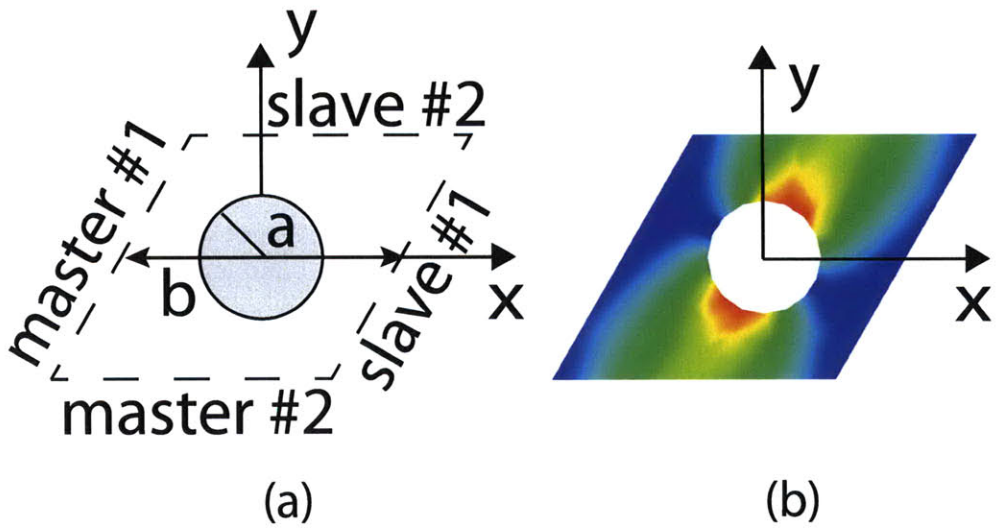

Figure 3-4: (a)Master/slave boundaries for the unit cell and (b) the equivalent HFSS model with the complex magnitude of the electric field of the lowest order propagating mode for $a/b = 0.2$, $\phi_1 = \pi/9$ and $\phi_1 = 19\pi/18$.

Table 3.1: Simulation Parameters to Investigate Brillouin Zone

	k_x	k_y	ϕ_1	ϕ_2
Γ to X	0	$0 \rightarrow 2\pi/\sqrt{3}b$	0	$0 \rightarrow \pi$
X to J	$0 \rightarrow 2\pi/3b$	$2\pi/\sqrt{3}b$	$0 \rightarrow 2\pi/3$	$\pi \rightarrow 4\pi/3$
J to Γ	$2\pi/3b \rightarrow 0$	$2\pi/\sqrt{3}b \rightarrow 0$	$2\pi/3 \rightarrow 0$	$4\pi/3 \rightarrow 0$

The results of eigenmode simulations for $a/b = 0.2$ and the full range of values in Table 3.1 are shown in Figure 3-5. The 8 lowest order modes are plotted as a function of $k_\perp$ and normalized frequency. A photonic band gap is defined as a range of frequencies over which no mode has a solution. In Figure 3-5 we observe that a very small gap opens from $\omega b/c = 6.69$ to $\omega b/c = 6.75$. Figure 3-5 is in excellent agreement with results published by Smirnova et al. [45] using alternate methods. In Figure 3-6 the eigenmode frequencies are plotted for $a/b = 0.43$ which corresponds to the radius to spacing ratio of the design mode. In this figure we can see three photonic band gaps for $\omega b/c = 5.35 \rightarrow 6.62$, $\omega b/c = 11.37 \rightarrow 12.12$ and $\omega b/c = 15.26 \rightarrow 16.93$.

Performing HFSS simulations over the full range of a/b it is possible to produce the global photonic band gap plot for a triangular lattice shown in Figure 3-7. This

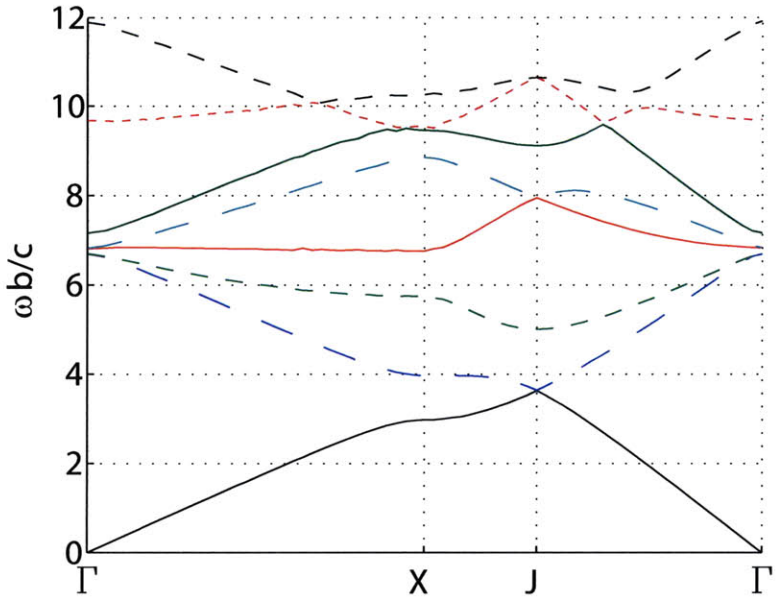

Figure 3-5: Normalized eigenmode frequencies as a function of $k_\perp$ for $a/b = 0.2$.

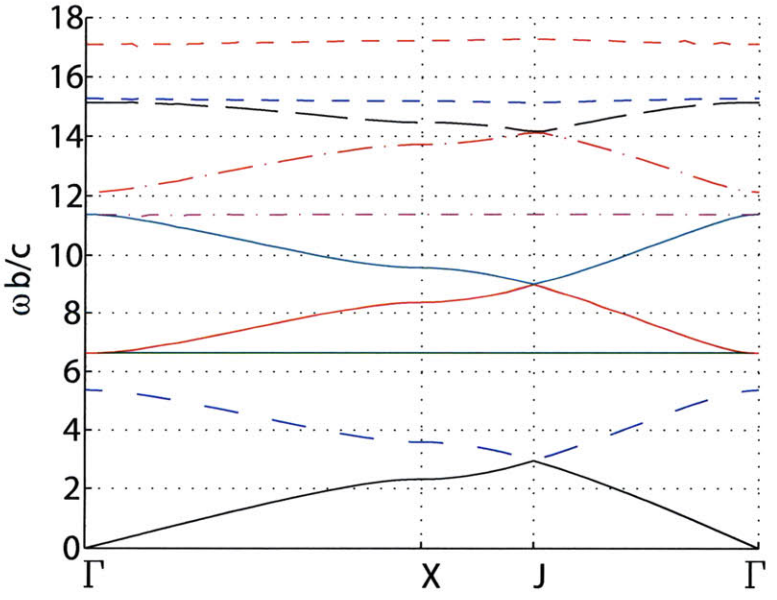

Figure 3-6: Normalized eigenmode frequencies as a function of $k_\perp$ for $a/b = 0.43$.

band gap plot is also in excellent agreement with results published by Smirnova et al. [45].

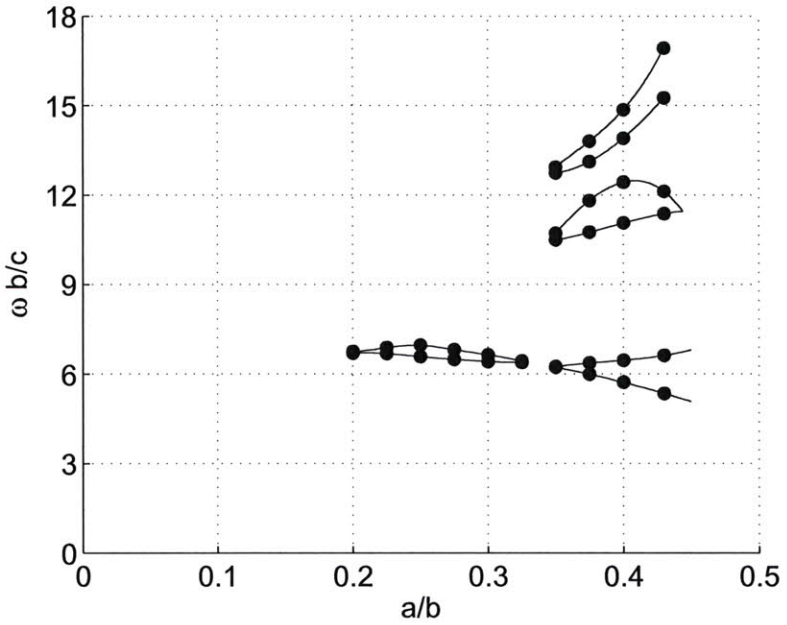

Figure 3-7: The global band gap plot for a triangular lattice, where a is the spacing and b is the diameter of the rod.

3.4 PBG Interaction Circuit

The interaction circuit is the most sensitive component in the entire design process and in large part defines the standards that other elements of the gyrotron amplifier must meet. The interaction region is limited to the flat top length of the magnetic field defined by 0.1% variation in the magnetic field (30 cm for this experiment). In order for the amplifier to interact efficiently with the electron beam, the beam must undergo a phase bunching process that results from the interaction with an electromagnetic field. After the phase bunching process is complete a majority of the power that will be extracted from the beam is produced in a few cenitmeters. It is important to quickly terminate the interaction with the beam to prevent reabsorption of microwave power. The selected photonic band gap (PBG) waveguide is a novel interaction structure for

gyro-TWTs that is highly mode selective and has strong coupling with the electron beam resulting in high interaction efficiency. A variety of geometries have been studied to find suitable mode confinement and frequency dependent characteristics. The circuit is based on a PBG composed of a two dimensional triangular lattice of metal rods with a central defect and it will be shown that it can meet the requirements of mode selectivivity and high interaction efficiency. The advantage of using this PBG structure is that its band gap structure is favorable for supression of lower order modes. With the proper lattice constants the PBG can confine electromagnetic radiation at 250 GHz while suppressing both higher and lower frequencies. The dimensions of the lattice are tuned so that the lattice acts as a perfect reflector in a narrow band of frequencies around the operating mode. A defect is created in the lattice by removing some rods, allowing a higher order mode to be confined with a high quality factor (Q). Other modes that can exist in the defect either at higher or lower frequencies suffer significant losses because of the partially transparent lattice [45]. A PBG gyrotron oscillator has already been demonstrated confirming the advantages of such a circuit in overmoded operation [43].

A transverse cross section of a triangular lattice of metallic rods is shown in Figure 3-2. The properties of the lattice are governed by the radius a and spacing b of the rods. The fundamental unit cell is demarcated by a dashed line. The fundamental cell should be infinitely repeated to create a perfect PBG. However, a non-infinite lattice still exhibits the basic nature of the PBG with highly reflective bands, especially in the case of metallic lattice. The corresponding band gap plot for the triangular lattice in Figure 3-2 is shown in Figure 3-8. The enclosed regions are the band gaps of the lattice. An electromagnetic wave of a given frequency will be perfectly reflected by a lattice with corresponding lattice constants a and b that reside in a band gap. If the frequency does not reside in the band gap the wave will be partially or fully transmitted through the lattice. The design point for the experiment at 250 GHz is marked with a red dot. The lower edge of the gap was selected because we are concerned about oscillations from lower order modes and this guarantees that none

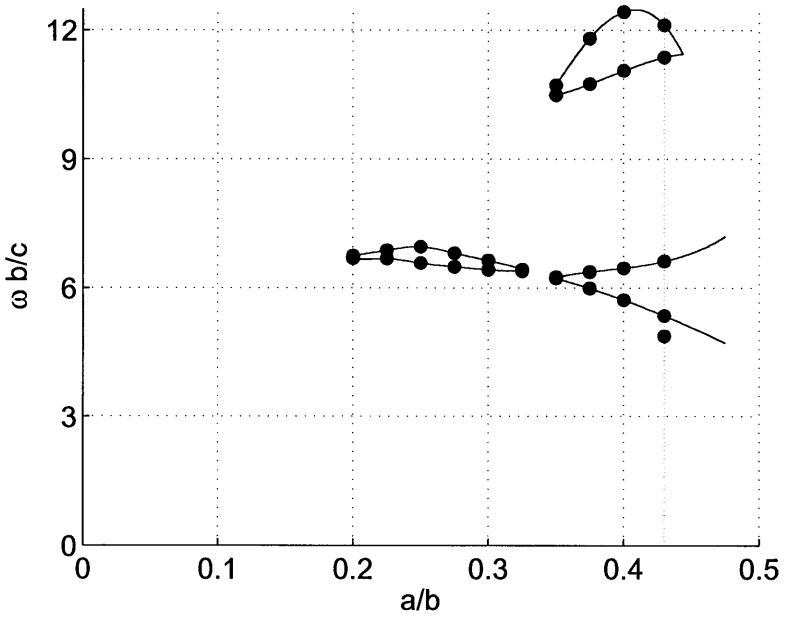

Figure 3-8: The global band gap plot with the operational spacing of $a/b = 0.43$ is marked with a dashed red line. The TE_{03} mode for a finite lattice with three rods removed is marked with a red point.

will be confined.

One difficulty of using a PBG structure is finding a mode that will interact well with an electron beam. By removing a number of rods a defect region is created in the lattice whereby a mode can be confined. Starting with the central location and removing three concentric rows of rods a TE_{03}-like mode can be excited. This mode is similar to the TE_{03} mode in a lossy circular waveguide and will have a good interaction with an electron beam that has a 1.1 mm radius that would reside on the second radial maximum of the electric field. This structure was simulated using the eigenmode solver in HFSS to find the confined modes. In Figure 3-9 the TE_{03} mode is plotted in a circular waveguide with a radius of 2 mm. This waveguide has many lower order modes that could easily spark oscillations in particular the TE_{23}, TE_{81} and TE_{42}. The corresponding TE_{03}-like mode confined be a PBG waveguide is shown in Figure 3-10 with a cutoff at 242.68 GHz, the PBG lattice constants of $\omega b/c = 4.87$ and $a/b = 0.43$ provide the appropriate amount of confinement and suppression of other modes. The diameter of the defect region is approximately the same size as

the circular waveguide. Unlike the TE_{03} mode in a circular waveguide, the main mechanism for attenuation is not ohmic losses, but diffractive radiation through the lattice due to the finite nature of the lattice. This should minimize the amount of ohmic heating on the metallic rods and it will require the addition of lossy material after the lattice to absorb the stray radiation.

Using a combination of eigenmode and driven modal simulations in HFSS it is possible to calculate the attenuation in the waveguide as a function of frequency as shown in Figure 3-11. With a loss of approximately -2dB/cm at 250 GHz we have a reasonable amount of attenuation in the waveguide. Additionally, HFSS simulations indicate the TE_{23}, TE_{81} and TE_{42} modes are not supported in the PBG waveguide.

HFSS can also be used to calculate the coupling between a waveguide mode and the electron beam. The normalized coupling factor [37] from Equation (2.42) for the TE_{03} mode in a circular and PBG waveguide are plotted relative to each other in Figure 3-12. The region of interest is the second maximum in the coupling factor, because an electron beam radius of less than 1 mm is impractical for this experiment. For an electron beam radius of 1.1 mm the normalized coupling factor for the PBG waveguide is 48% compared to a circular waveguide. The decrease in the normalized coupling factor between the electron beam and the PBG waveguide mode is acceptable in light of the additional advantages of the PBG waveguide. Furthermore, the interaction between the electron beam and a waveguide mode can be increased by adjusting electron beam parameters. The normalized coupling factor of the PBG waveguide is almost constant between 1-1.2 mm allowing for some variation in the electron beam radius without impacting the coupling.

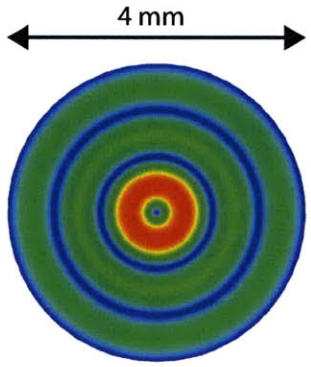

Figure 3-9: The complex magnitude of the electric field for the TE_{03} mode confined in a circular waveguide.

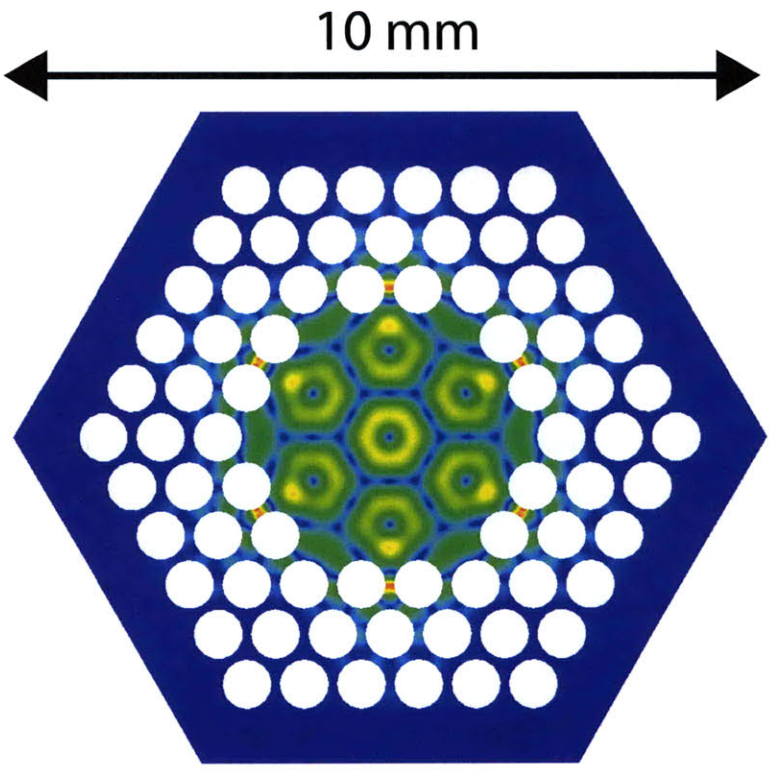

Figure 3-10: The complex magnitude of the electric field for the TE_{03}-like mode confined in a PBG composed of a triangular lattice of metal rods.

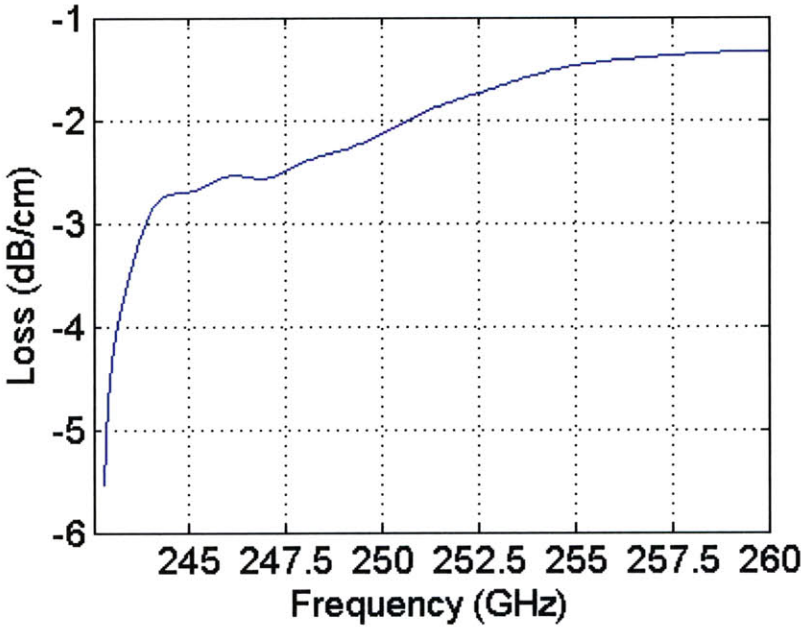

Figure 3-11: Attenuation as a function of frequency for the TE_{03}-like mode.

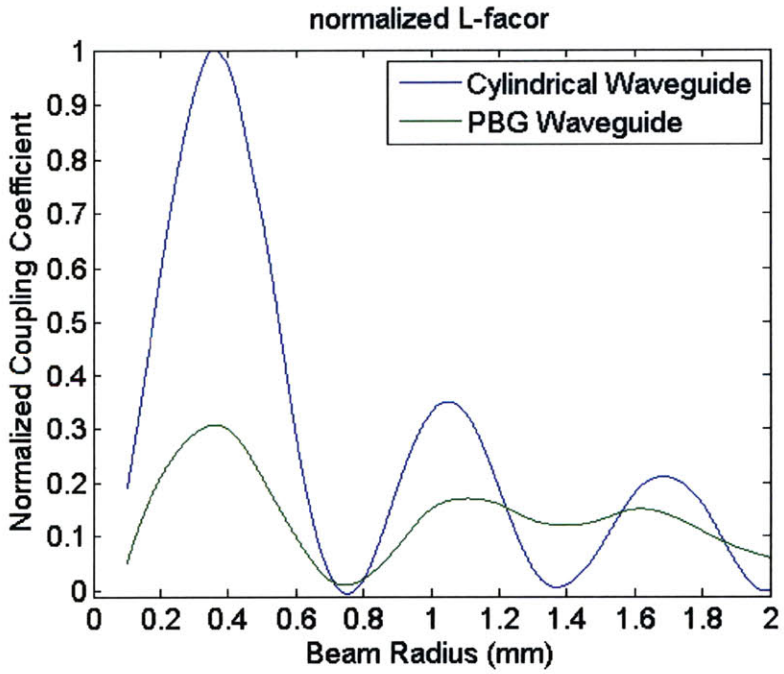

Figure 3-12: Normalized coupling coefficient comparison for a circular waveguide and the PBG waveguide. The electron beam radius for the gyro-TWT will be 1.1 mm.

3.5 Linear Growth Rate

In the limit of small signal gain the equations of motion for the electrons in the gyro-TWT, Equations (2.29)-(2.31), can be linearized [38] to produce the dispersion relation in Equation (2.43). Using this small signal dispersion relation in combination with the normalized coupling coefficient, loss parameters for the PBG circuit, and S-parameters for circular to PBG waveguide junctions calculated in HFSS it is possible to calculate the single pass and round trip gain for the device. The linear growth rate is extremely dependent on the electron beam parameters and needs to be optimized to maximize the circuit gain and bandwidth. It is easiest to achieve large bandwidths when the amplifier is slightly detuned from a grazing condition with the waveguide dispersion relation. The further the grazing condition is from cutoff the larger the bandwidth, but lower the gain. There are also several disadvantages that come with operating too close to cutoff. First, a strong interaction between the wave and the beam close to cutoff increases the possibility of self start oscillations. Second, waveguide dispersion limits the gyro-TWTs ability to amplify short pulses, as will be discussed in detail in Chapter 4. For these reasons the amplifier's bandwidth is centered at 3% above cutoff or 250 GHz. There are also some advantages to lowering the linear growth rate (for a fixed attenuation constant) in order to make a high gain amplifier while avoiding driven oscillations. If the growth rate is relatively small a long circuit will be required to achieve the desired gain of more than 50 dB. For a driven oscillation to occur, the roundtrip gain must be greater than 0 dB, meaning a wave that is amplified, reflected from the end of the interaction region, propagates to the start of the circuit and is reflected again has increased in energy. If the gain per cm is approximately twice the attenuation per cm it is easier to suppress the driven oscillation. With an attenuation of -2dB/cm at 250GHz a linear growth rate of 4dB/cm meets this condition. Taking these things into consideration the optimized electron beam parameters that were calculated for this structure are listed in Table 3.2.

Figure 3-13 shows the linear growth rate as a function of frequency for the TE_{03}

Table 3.2: Design Operating Parameters from Linear Theory

Beam voltage, V_0	32 kV
Beam current, I_0	1.0 A
Beam pitch factor, α	0.75
Beam Radius	1.1 mm
Input power	1 mW
Center Frequency	250 GHz
Peak Magnetic Field	8.81 T
Operating Mode	PBG TE_{03}-like
Circuit Length	22 cm

mode in a circular and PBG waveguide for the same electron beam parameters, calculated using Equation (2.43) and the parameters in Table 3.2. These operational parameters provide a reasonable growth rate, a very large bandwidth and no amplification within 2 GHz of the cutoff frequency. As was mentioned previously the normalized coupling factor is considerably lower for the PBG waveguide compared to the circular waveguide, but it has a limited impact on the growth rate.

It is reasonable to assume that the amplifier will be operating at the edge of the linear regime so we can use the linear growth rate for an estimate of the circuit gain. For a fixed input power of 1mW, of which only 1/3 couples into the growing solution of the dispersion relation in Equation (2.43), the circuit gain is calculated by subtracting the attenuation from the growth rate and multiplying by the circuit length, with the results show in Figure 3-14. In addition to the single pass gain, it is important to calculate the round trip gain to consider the effect of driven oscillations. As shown in Figure 3-14 the round trip gain is below 0 dB for the full operational range of the amplifier.

In order to include the effects of perpendicular velocity spread of the electron beam MAGY [10], a non-linear, self-consistent simulation code, was used. This software is the most common package used for the design of gyrotron oscillators and amplifiers, and has shown good experimental agreement for both cases [10] [31]. In Figure 3-15

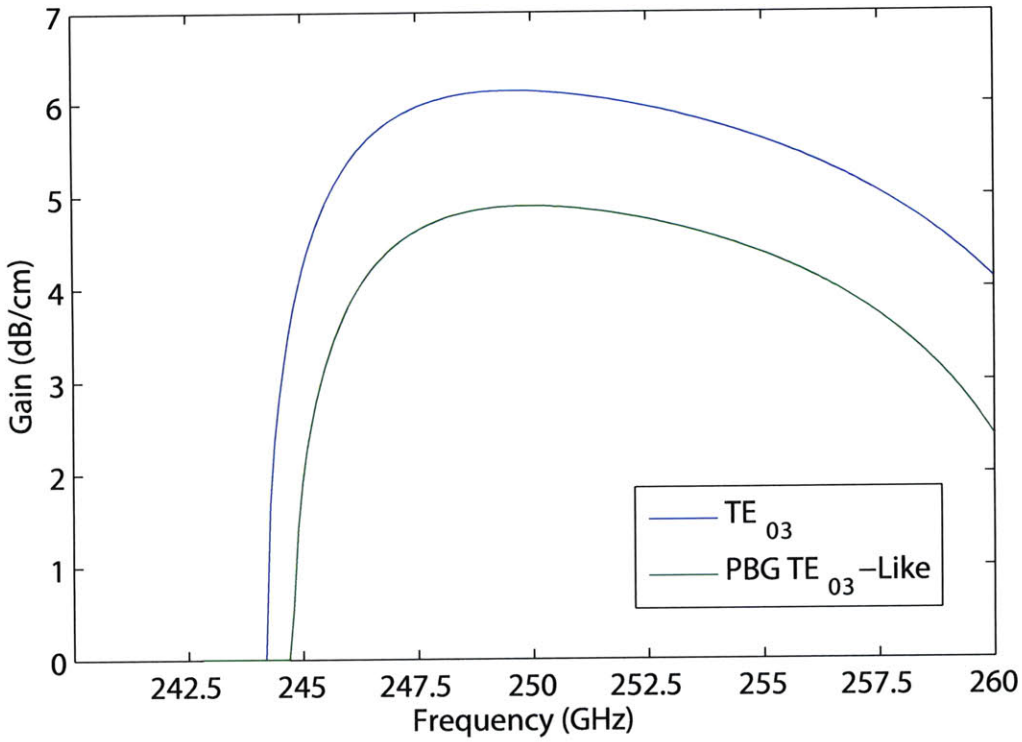

Figure 3-13: Gain in dB/cm from linear theory.

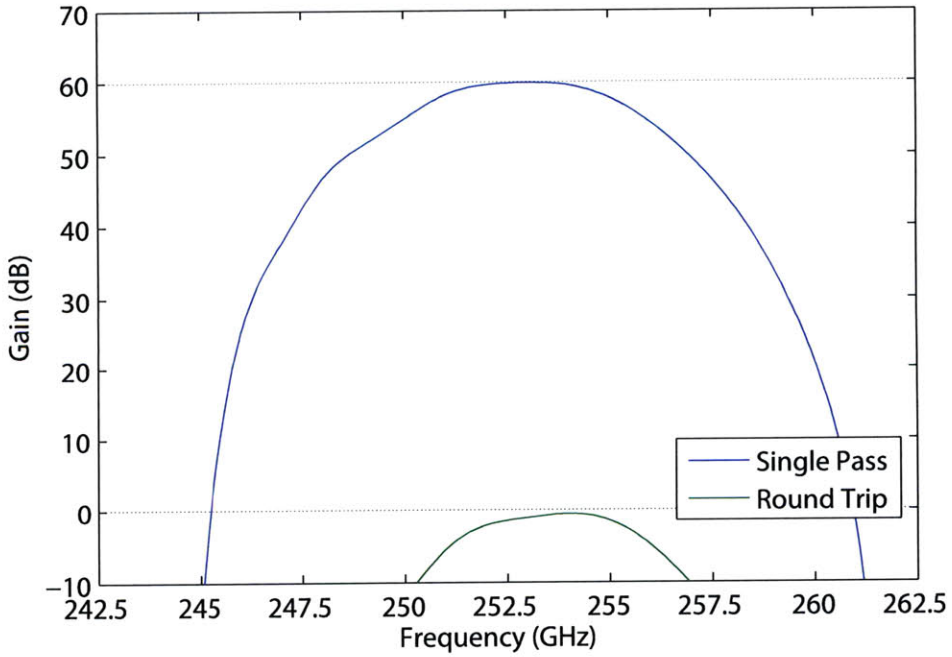

Figure 3-14: Gain in the device calculated from the linear growth rate and loss per unit length of the circuit. Reflections are suppressed enough to prevent oscillations.

the gain in dB/cm is shown for the linear growth rate and simulations using MAGY at 250 GHz. A practical electron gun should be able to achieve 5% perpendicular velocity spread as will be shown in Section 3.8. The electron beam in the MAGY simulations presented includes 5% velocity spread and is otherwise identical to the parameters listed in Table 3.2. In addition to the previous calculations using the linear growth rate and a circuit length of 22 cm, Figure 3-16 shows the results of MAGY for a 26cm cavity. The frequency dependent characteristics of the structure that are calculated using HFSS were implemented in MAGY. MAGY simulations require the use of a circular waveguide and the geometry cannot be altered to take into account the PBG. To account for this the electron beam was placed at a slightly larger radius where it would have the same coupling coefficient as the PBG mode. To achieve the correct attenuation constant the conductivity of the waveguide in the interaction region was altered to match the the values in Figure 3-11. The circuit in MAGY also includes an uptaper designed using CASCADE to minimize reflections, discussed in Section 3.7. The input power for the numerical simulations was 1 mW. Agreement between linear theory and MAGY is excellent, with both cases showing approximately 3 GHz of bandwidth. The center frequency of the MAGY simulations is slightly lower than the linear theory due to the impact of velocity spread which is more severe on higher frequencies.

The output power of the amplifier for a 1 mW input and for saturated operation is shown in Figure 3-18. For an input of 1 mW the amplifier produces more than 1 kW of peak output power. The saturated output power shows that the amplifier is operating on the edge of the saturated regime. Figure 3-19 shows the input versus output power curve for 250 GHz. Below 1 mW of input power the amplifier exhibits linear behavior and above 1 mW the gain falls rapidly as the output of the amplifier saturates.

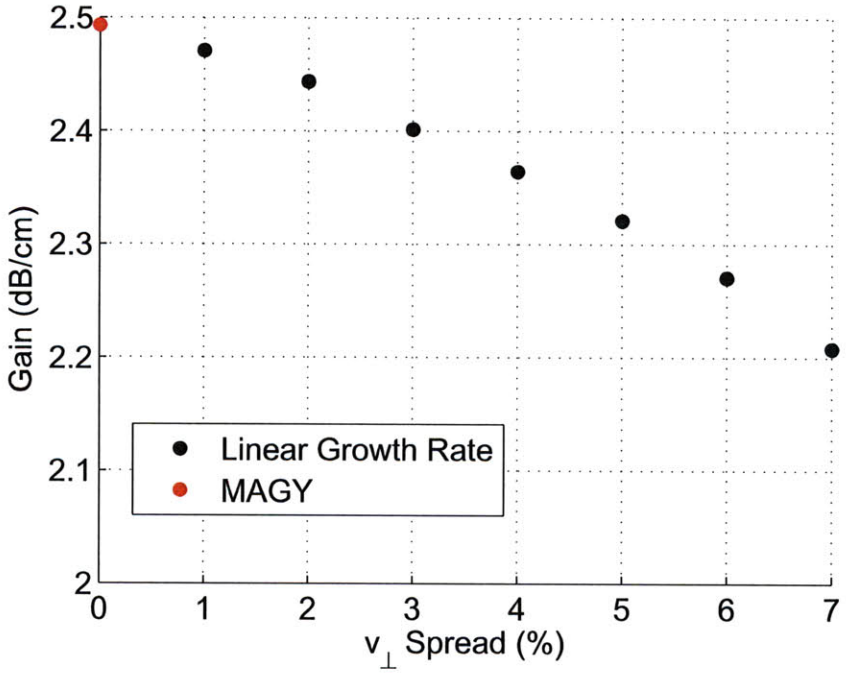

Figure 3-15: Gain in dB/cm at 250 GHz as a function of perpendicular velocity spread calculated from the linear growth rate and MAGY.

Table 3.3: Design Operating Parameters from MAGY

Beam voltage, V_0	32 kV
Beam current, I_0	1.0 A
Beam pitch factor, α	0.75
Beam Radius	1.1 mm
Input power	1 mW
Center Frequency	250 GHz
Peak Magnetic Field	8.81 T
Operating Mode	PBG TE_{03}-like
Perpendicular Velocity Spread	5%
Circuit Length	26 cm

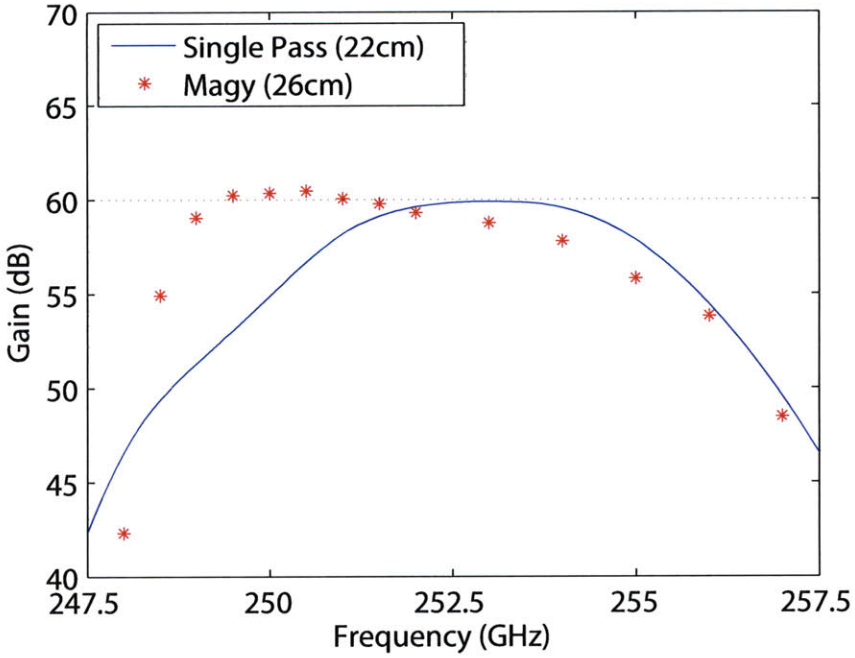

Figure 3-16: Gain in the device calculated from the linear growth rate for a 22 cm circuit compared to results from MAGY for a 26 cm circuit with 5% perpendicular velocity spread.

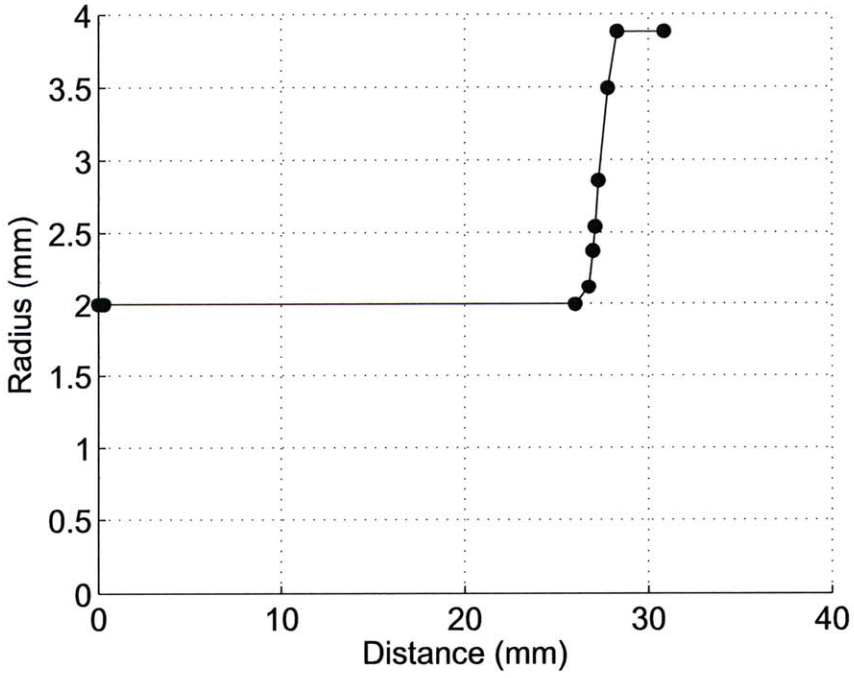

Figure 3-17: Dimensions of circuit simulated in MAGY.

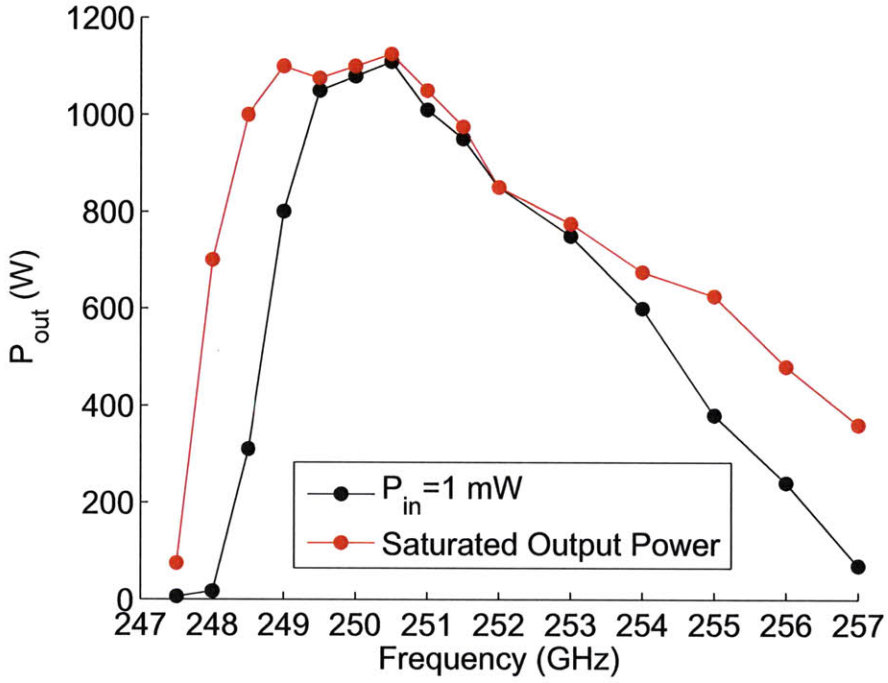

Figure 3-18: Output power as a function of frequency simulated with MAGY using a 32 kV, 1 A electron beam with 5% $v_\perp$ spread.

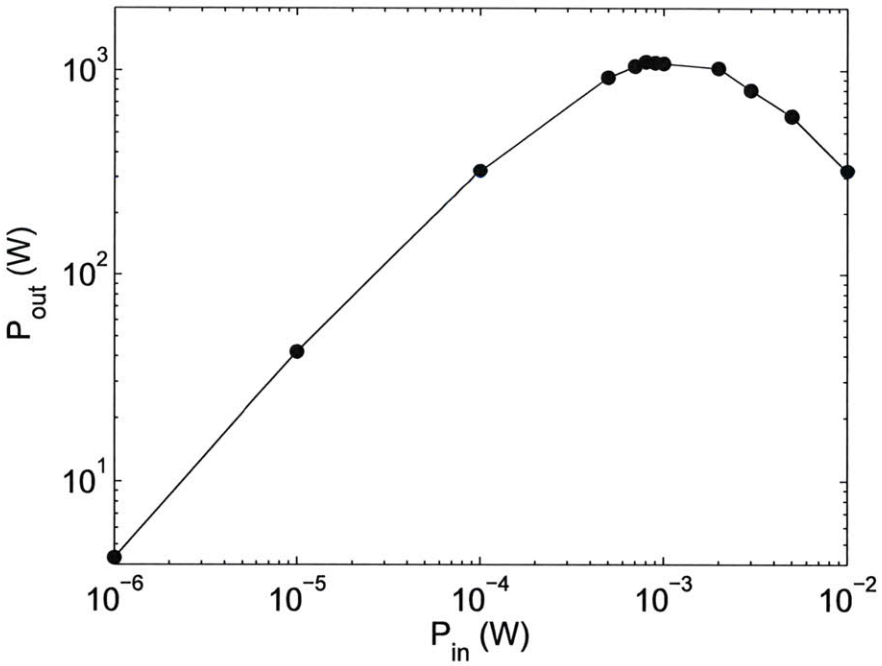

Figure 3-19: Output power as a function of the input power for 250 GHz.

3.6 Input Coupler

The input coupler must efficiently convert the 250 GHz driver signal from TE_{10} mode in a fundamental rectangular waveguide into the operational mode of the amplifier. The operational mode of the amplifier is very similar to the TE_{03} mode in a circular waveguide. The proposed method for the efficient excitation of the amplifier is the use of a wraparound coupler for a small section of circular waveguide, with a radius that corresponds to the same cutoff frequency of the PBG waveguide, that mates directly to the PBG structure.

A wraparound coupler works by exciting a standing wave in a rectangular resonant ring that wraps around the circular waveguide. Coupling slots are placed at nulls in the electric field of the ring resonator to induce currents in a circular waveguide that will excite the TE_{03} mode. Once the mode is excited in the circular waveguide as much energy as possible should be directed towards the interaction region. To direct the mode towards the PBG structure a down taper is placed on one side of the coupling slots. The down taper reduces the size of the circular waveguide until it goes below cutoff for the TE_{03} mode. This reflects the power traveling towards the electron gun without producing mode conversion. The additional benefit of having a down taper is the electron gun is protected from high power radiation in the TE_{03} mode that could be generated if the amplifier begins to oscillate. Simulations of the structure were run in HFSS using driven modal solutions with an input waveport on the rectangular waveguide leading to the wraparound coupler. An output waveport was placed at the end of 5 mm of PBG structure and short cylindrical section. This allows the S-parameters to account only for the pure TE_{03} content of the waveguide. An electric field symmetry plane was used to reduce simulation time. The geometry is symmetric about the x-z plane.The schematic of the wraparound coupler is shown in Figure 3-20(a) as it was modeled in HFSS. In Figure 3-20(b)-(d) the evolution of the complex magnitude of the electric field is shown as it propagates down the coupler. The wave begins by forming a standing wave in the resonant ring that then

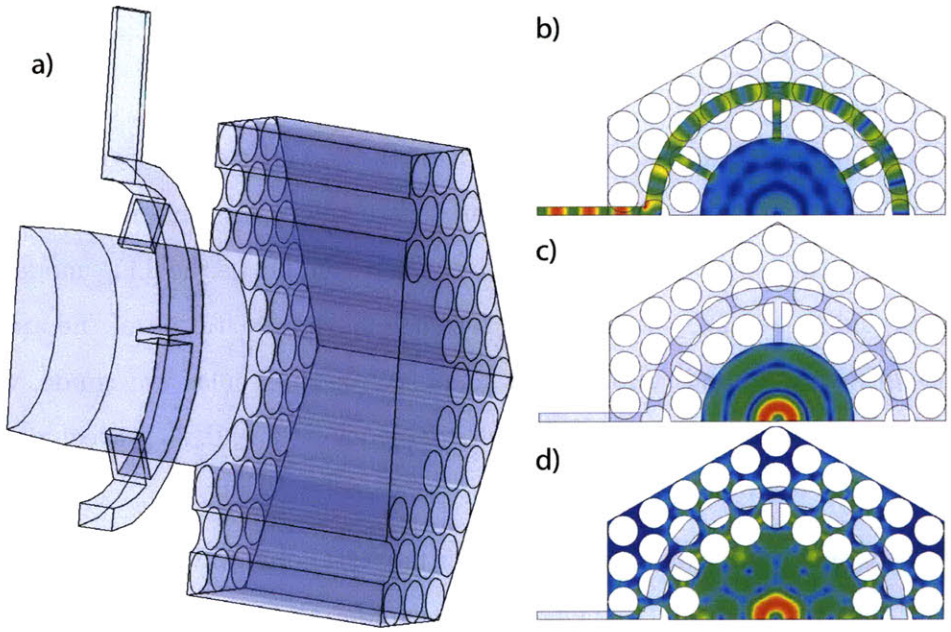

Figure 3-20: The (a) cross section the input coupler with the components (from left to right) downtaper, wraparound, circular waveguide and PGB waveguide. The complex magnitude of the electric field at 250 GHz shown in (b) the wraparound, (c) the circular waveguide and (d) the PBG waveguide.

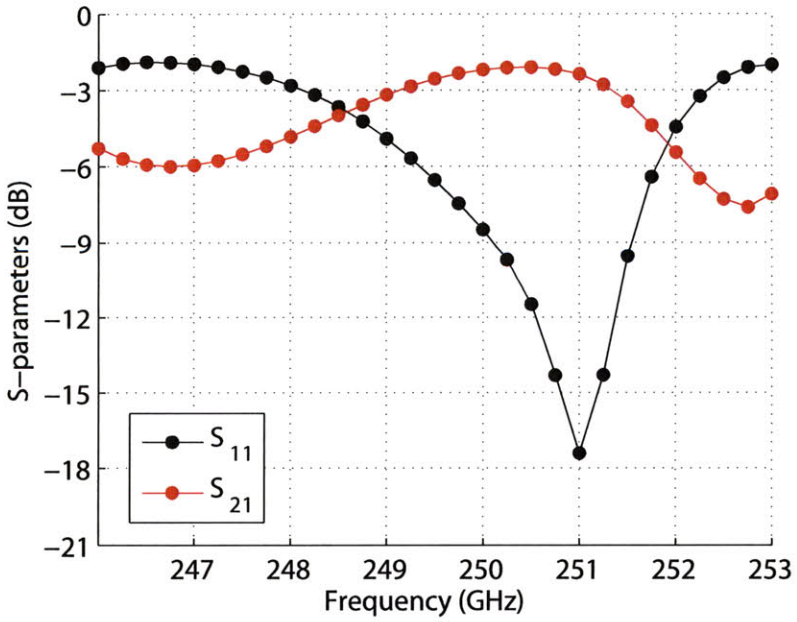

Figure 3-21: S-parameters for the wraparound input coupler.

couples into the circular waveguide where the TE_{03} mode is formed. After the TE_{03} propagates into the PBG waveguide it changes into a form that is very similar to the result in Figure 3-10. The S-parameters of the coupler are shown in Figure 3-21. Using HFSS we calculated the S_{11} for the input coupler to be -18 dB at 251 GHz. S_{21} is measured after the wave has propagated into the PBG waveguide. The coupler converts more than 50% of the power into a forward propagating wave over 2 GHz of bandwidth.

3.7 Output Coupler

Power extraction from the amplifier must meet two criteria: minimum reflections into the interaction circuit and a radiation pattern that will couple into a transmission line. As a first stage of the output coupler the near cutoff interaction circuit is enlarged to lower the cutoff frequency, decrease the interaction with the electron beam and minimize reflections. Using CASCADE a multi-step uptaper was optimized to minimize reflections from cutoff up to 260 GHz. The final radius of the waveguide, $a = 3.88$ mm was selected so that the bounce angle would be $\theta_B \approx 50°$ determined by

$$\theta_B = sin^{-1}\left(\nu_{nm}/ka\right). \tag{3.12}$$

The uptaper simulated in CASCADE is shown in Figure 3-22. Both ends of the waveguide are perfectly matched in this simulation and do not produce reflections. S_{11} and S_{21} for the TE_{03} mode in a circular waveguide are shown in Figure 3-23 and Figure 3-24, respectively. After the uptaper, the TE_{03} mode can either be extracted axially or it can be mode converted into a Gaussian beam and be extracted radially. The axial configuration is simplest, but not optimal for pulsed DNP experiments as they require a Gaussian beam to propagate the radiation to the NMR test stand and couple it into the sample [3]. The Gaussian beam mode converter can be designed by considering the quasi-optical nature of the 250 GHz signal and decomposing the

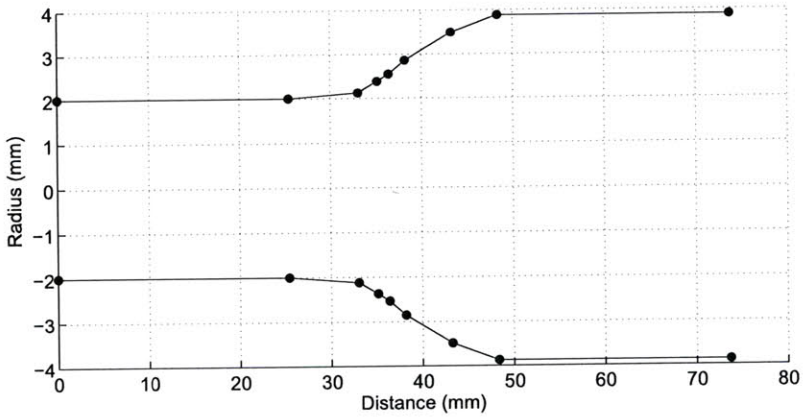

Figure 3-22: Uptaper dimensions simulated and optimized in CASCADE.

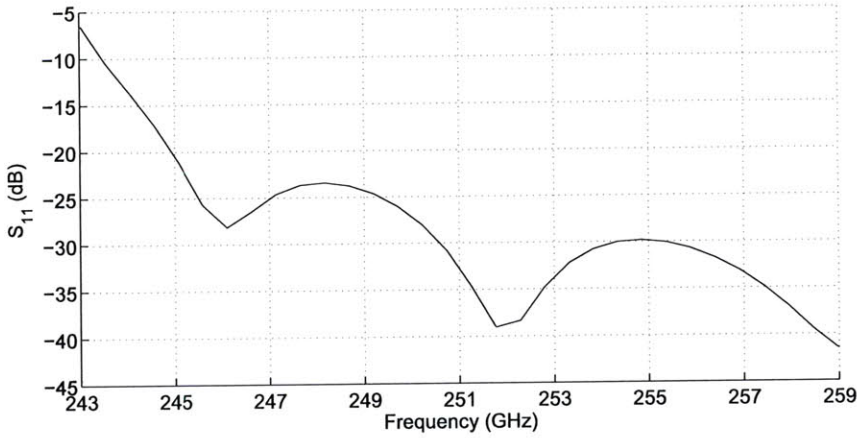

Figure 3-23: S_{11} of the uptaper for the TE_{03} mode.

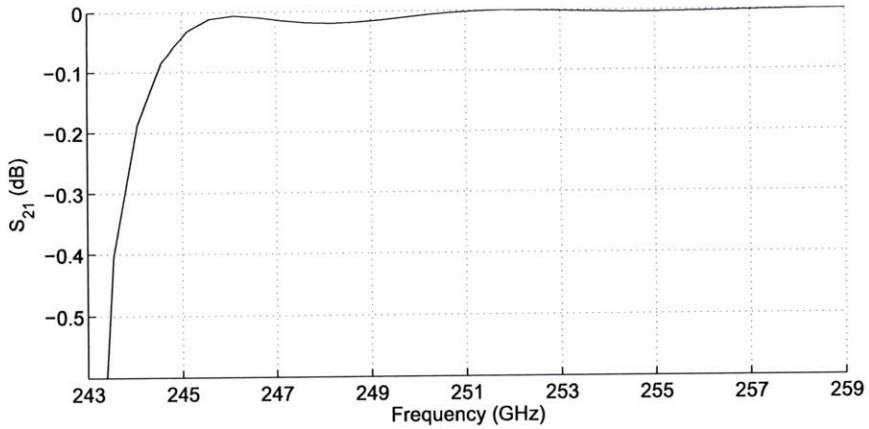

Figure 3-24: S_{21} of the uptaper for the TE_{03} mode..

waveguide mode into a series of plane waves that propagate at a bounce angle based on the radius of the waveguide. If the waveguide was terminated these plane waves would radiate outward radially permitting a parabolic mirror to reflect them as a plane wave. In order to limit the direction of the radiation the termination is not a smooth cut, but a notch in the waveguide that allows all of the exiting plane waves to radiate into a half-space.

3.8 Electron Gun

The electron gun must meet very specific requirements in order for the amplifier circuit to operate successfully, because the interaction efficiency is highly dependent on the beam quality. In a standard electron gun a large electric field extracts electrons from an annular ring on the cathode. The extraction of electrons occurs by heating the cathode and applying a large potential bias between the cathode and anode. The electric field between the cathode and anode is partially transverse to the static axial magnetic field at the cathode. The transverse component causes the electrons to begin gyrating. The electrons undergo compression as they enter the higher intensity magnetic field area. The static magnetic field also prevents the electrons from being intercepted by the anode which is before the interaction region. There can be either one (diode) or two (triode) anodes in the electron gun. The triode configuration increases the beam quality by creating extraction and acceleration regions. Additionally, the ability to modify the voltage on the first anode (mod-anode) provides increased control over the static electric field profile allowing the user to vary the alpha of the electron beam. This is of great importance in the operation of the gyro-TWT as it allows the user to tune the operating region of the amplifier by raising or lowering the main magnetic field and adjusting the alpha accordingly to reach grazing condition. The electron gun was designed using the simulation code MICHELLE. Initial design parameters for the electron gun configuration were calculated using equations based on conservation of angular momentum and adiabatic

Table 3.4: Electron gun parameters

Electron Gun	Preliminary Parameters
Type	Triode
Beam Voltage	35 kV
Beam Current	2 A
Beam Radius	1.0 mm
Velocity Pitch Factor, α	0.75
Perpendicular Velocity Spread	$\leq$ 3%
Cathode Radius	4.4 mm
Compression Ratio	19
Magnetic Field at Gun	0.46 T
Electric Field at Gun	$\leq$ 100 kV/cm
Cathode - Main Anode Voltage	15 kV

electron motion.

Using the design equations given in [2] a first order design was found by specifying the main design parameters: current, voltage, main magnetic field, compression and velocity pitch factor, α. Experience has shown [34] that a slope of 50 degrees (between the axis of symmetry and the emitter surface) for the emitter produces the highest quality beams with an acceptable beam width. The basic gun design parameters can be plotted as a function of the mean emitter radius as shown in Figure 3-25. In order to minimize the maximum electric field and decrease the width of the emitter strip a large compression factor is favorable. The practical limit for the compression factor is approximately 25, setting this as the criteria we arrive at a mean emitter radius of 5.2 mm. The remaining design parameters are marked as black dots in Figure 3-25.

The initial drawing of the triode electron gun using the design parameters from Figure 3-25 for a cathode slope of 50 degrees was optimized using MICHELLE to minimize the perpendicular velocity spread. MICHELLE also verified the performance of the electron gun over a range of beam voltage(up to 50 kV) and mod-anode voltage to ensure that the electron gun would have the desired tunability. The final CAD drawing of the electron gun is shown in Figure 3-26. The mean emitter radius, emitter strip width, cathode slope and cathode to anode spacing correspond to the

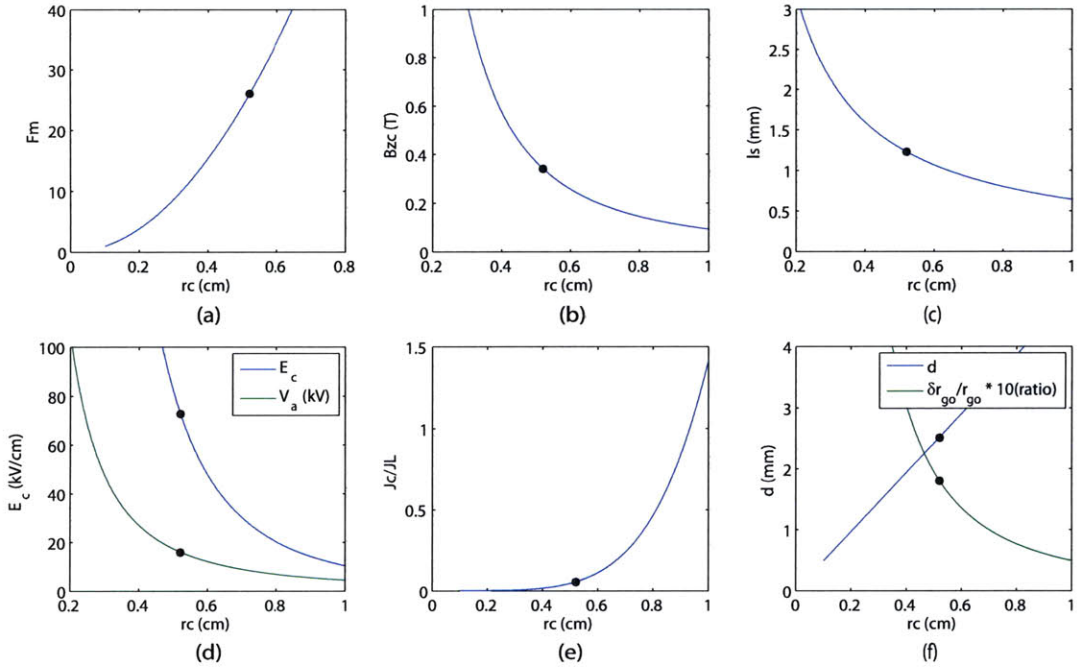

Figure 3-25: Gun parameters calculated using equations derived by Baird and Lawson for a 32 kV 2 A beam and 50 degree cathode tilt. The (a) compression, (b) magnetic field at the emitter, (c) emitter width, (d) maximum electric field and cathode to mod-anode potential, (e) Langmuir space charge, and (f) cathode to mod-anode spacing, d, and guiding center spread are plotted versus the mean emitter radius. Black dots mark the selected design values.

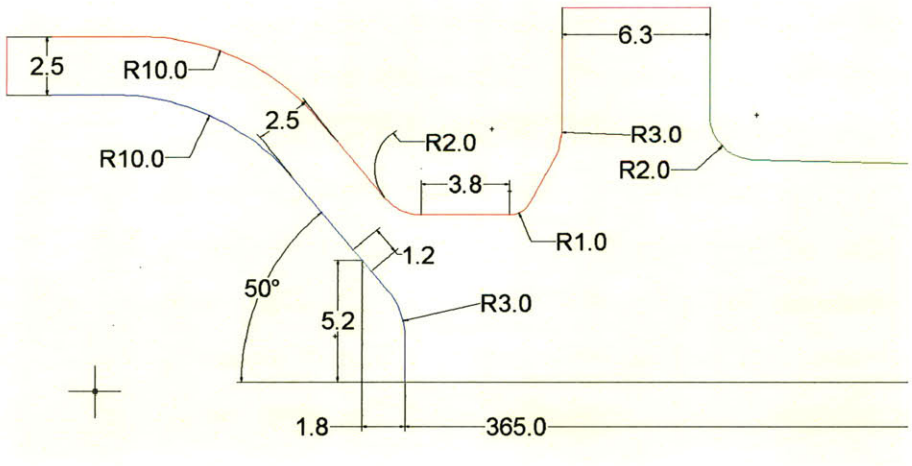

Figure 3-26: Schematic of the electron gun design with all units in mm unless otherwise marked.

design parameters shown in Figure 3-25. The drawing of the electron gun includes the cathode (blue line), emitter (teal line), mod-anode (red line), the anode or common (green line) and dielectric spacers (purple line). The full CAD drawing as modeled extends to the right until the beginning of the interaction circuit and the electron gun is cylindrically symmetric about the black line. The electron gun placement was determined using the magnetic field profile of the 9.6 T Cryomagnetics magnet currently under construction. The emitter strip is located 366.8 mm before the beginning of the flat top of the magnetic field. One important consideration is that the magnetic field is monotonically increasing from the emitter location to the flat top. The magnetic field used to model the electron gun and the guiding center radius is plotted in Figure 3-27. The guiding center radius is monotonically decreasing as it approaches the flat top of the magnetic field. In Figure 3-27 the flat top of the magnetic field extends from 0 to 30 cm. The location of the electron gun is marked with a black dot. For the current design the magnetic field uses an internal gun coil at 25% of its rated current to decrease the magnetic field at the cathode. It is possible that during operation the gun location could be changed requiring an adjustment of the current in the gun coil to maintain the compression and ensure a proper guiding center radius. The magnetic field $\pm 25\%$ the rated current of the gun coil is shown in Figure 3-28. The magnetic field at the cathode for the optimized electron gun is marked with a black dot.

The physical location of the electron gun will reside comfortably within the 5 in magnet bore. A side view of the 9.6 T Cryomagnetics magnet is show in Figure 3-31. The emitter strip will be located 1 cm into the bore of the magnet. The electron gun will be encased in a metallic can to provide a grounding plane allowing for the option of moving the electron gun without affecting the grounding plane by the presence of the inner wall of the magnet bore.

The optimal design parameters of the electron gun consist of a 2 A beam with a cathode voltage of -32 kV, a mod-anode voltage of -18kV, and an anode voltage of

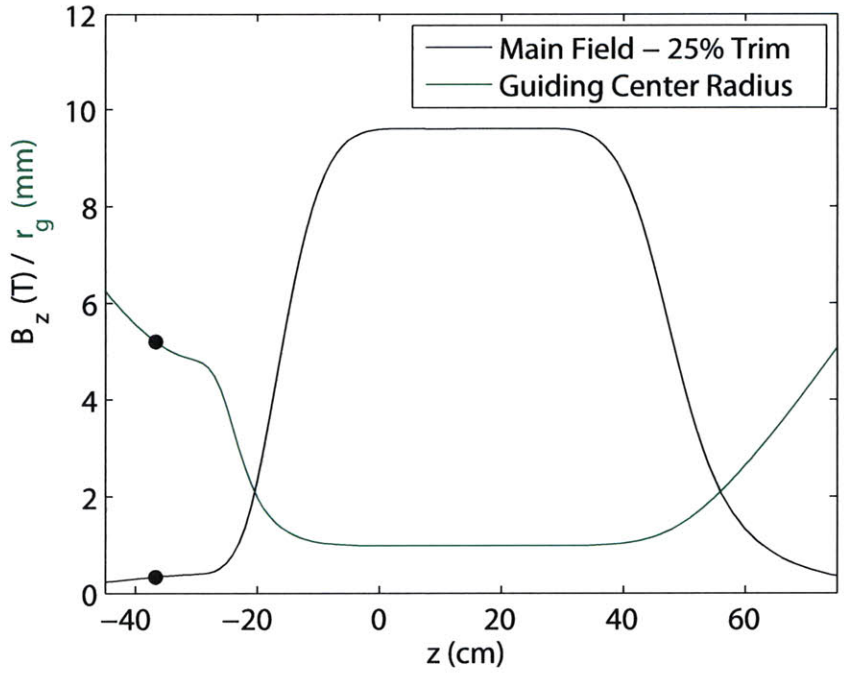

Figure 3-27: The magnetic field as used to model the electron gun performance. The guiding center radius is also plotted along the axis of the magnet.

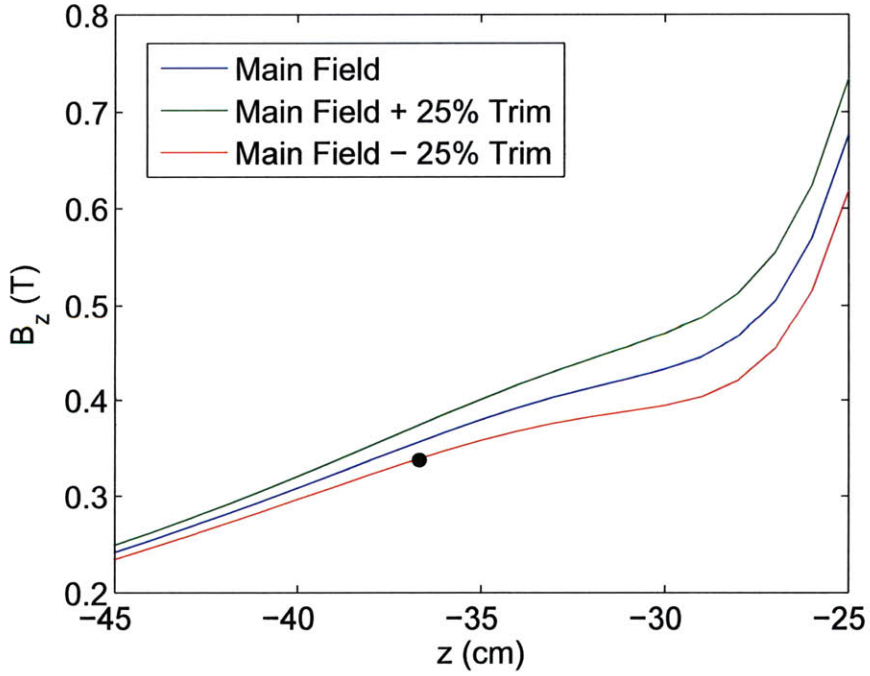

Figure 3-28: The main magnetic field with the gun coil magnet at 0% and ±25% of the rated current.

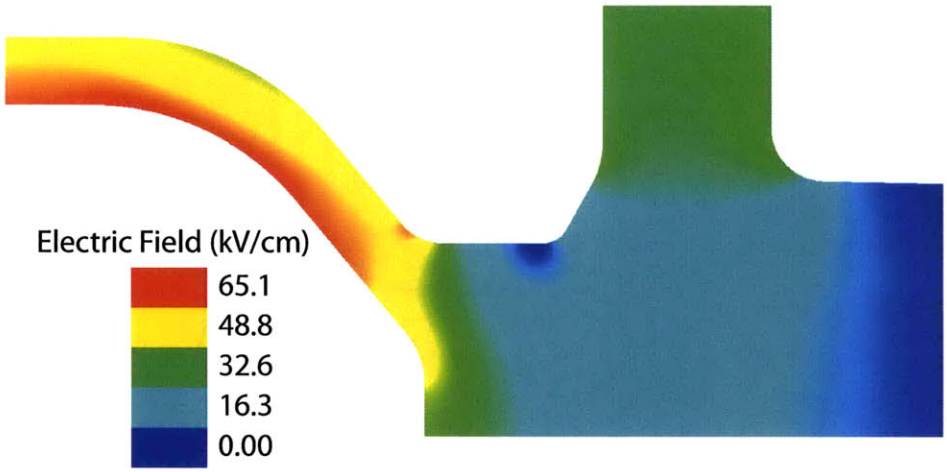

Figure 3-29: Electric field distribution for the cathode at -32 kV, mod-anode at -18kV and anode at ground.

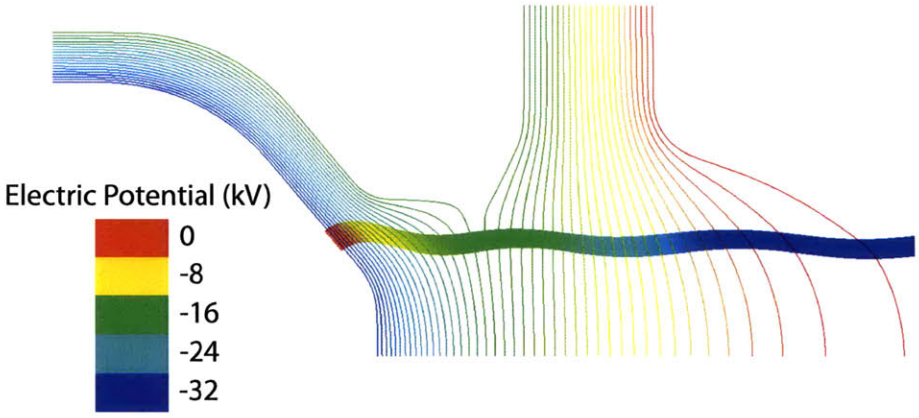

Figure 3-30: Electric potential lines and particle trajectories for the cathode at -32 kV, mod-anode at -18kV and anode at ground. Gun coil at 25% of rated current.

0 V. The electric field produced under these conditions is shown in Figure 3-29 with a comfortable maximum of 65.1 kV/cm. The potential lines and particle trajectories under the same conditions are show in Figure 3-30. Two distinct regions can be observed in the electron gun. The first stage extracts the electrons with the field produced by the mod-anode and is approximately one cyclotron orbit in length. The α and velocity spread are primarily determined in this section. The accelerating region occurs after the first complete cyclotron orbit where the electrons pass over potential lines that are transverse to their motion.

The triode electron gun designed using MICHELLE produces the desired beam pitch factor of 0.75 with a velocity spread of less than 2% for a 32 kV 2 A beam and 18 kV mod-andode voltage as shown in Figure 3-32. The electron gun was also investigated over a large range of mod-anode and beam voltages with results in Figure 3-32, Figure 3-33 and Figure 3-34 indicating that this design is capable of producing an α of 0.75 for beam voltages as high as 50 kV with a velocity spread of $\sim$2%. The velocity spread in the constructed electron gun will be greater due to surface roughness effects and machining errors and could rise to as much as $\sim$5%. The current design consists of a cathode with a 50 degree tilt that can comfortably produce a 2 A beam (current density of 5 A/m^2). The gun coil will provide additional tunability of the beam pitch factor and aid in the suppression of velocity spread. From 32-50 kV varying the mod-anode voltage to be 50-66% of the cathode voltage varies the beam from an α of 1-0.6 without ever exceeding the 96 kV/cm limit or reflecting electrons.

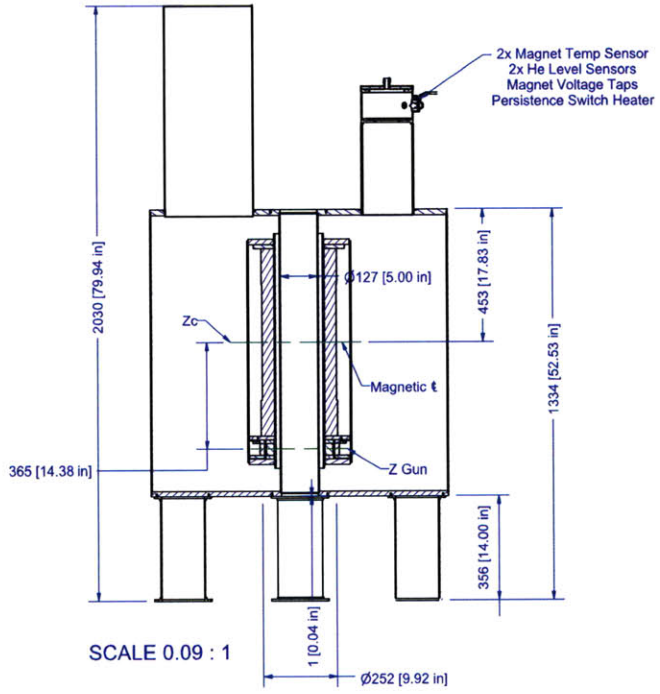

Figure 3-31: Cross sectional CAD drawing of 9.6 Tmagnet.

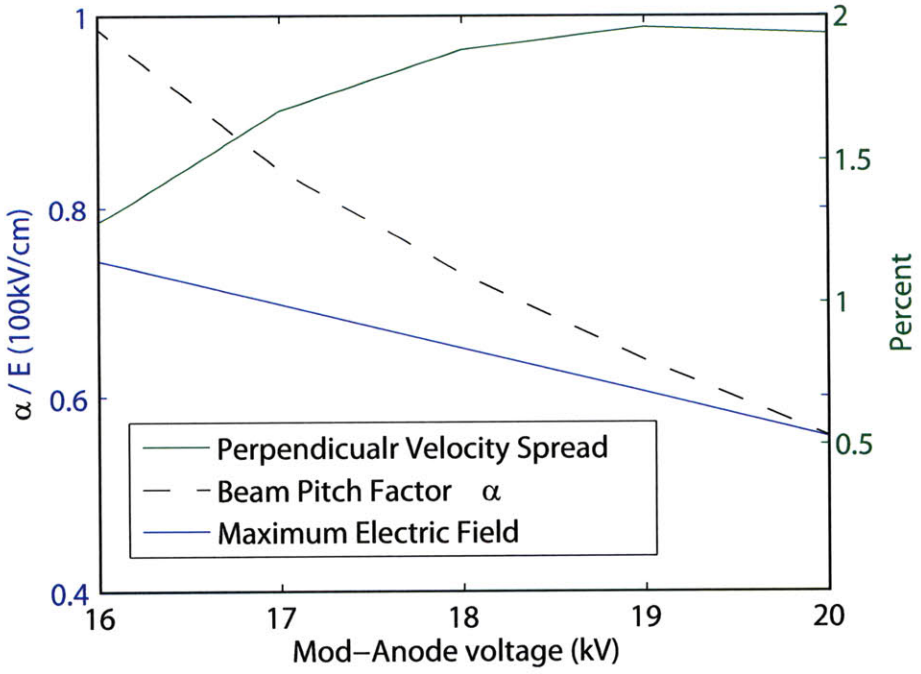

Figure 3-32: Operational parameters for the electron gun at 32 kV. Gun coil at 25% of rated current.

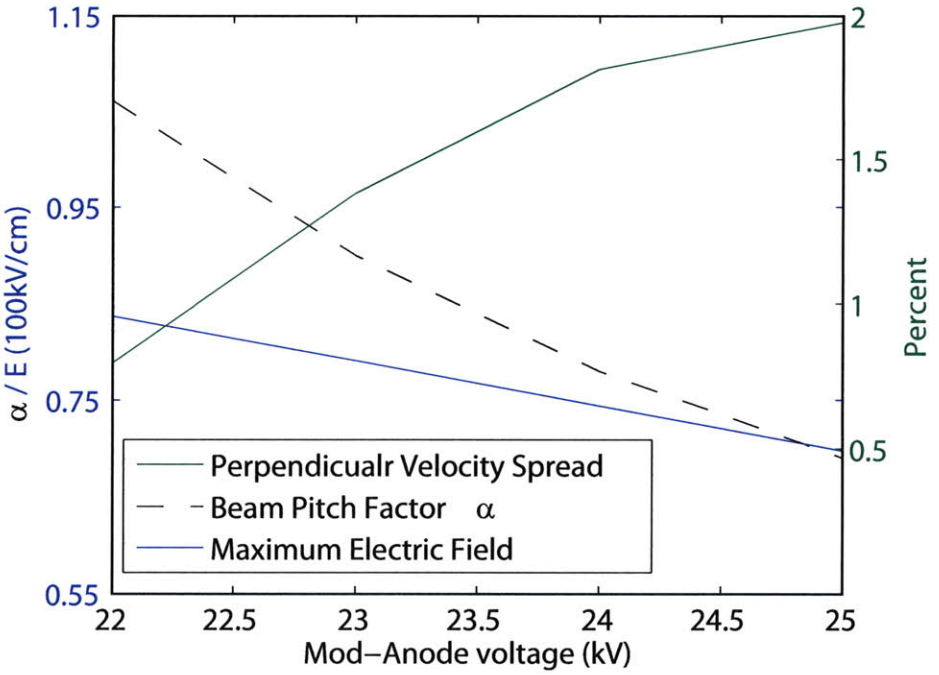

Figure 3-33: Operational parameters for the electron gun at 40 kV. Gun coil at 25% of rated current.

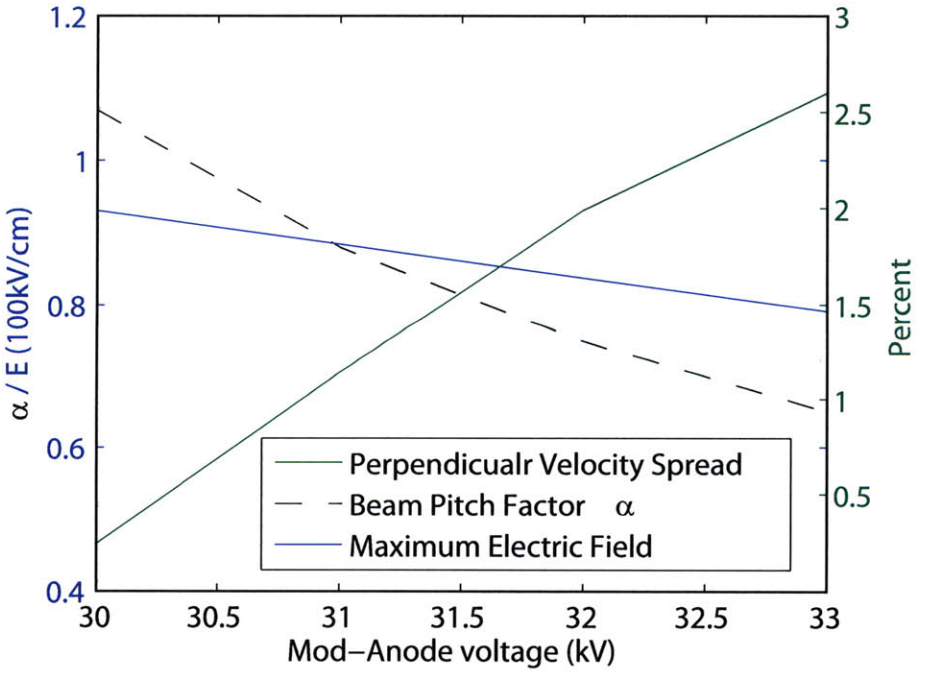

Figure 3-34: Operational parameters for the electron gun at 50 kV. Gun coil at 25% of rated current.

3.9 Conclusion

The complete design of a novel 250 GHz gyro-TWT based on a PBG interaction circuit has been presented. This design relies on the frequency dependent distributed loss provided by the interaction circuit to suppress both forward and backward wave oscillations from lower order modes. Linear theory and non-linear simulations have shown reasonable operational parameters and circuit length will provide the desired gain and bandwidth. With 60 dB of amplification and over 3 GHz of bandwidth the design meets the requirements of pulsed DNP experiments. An electron gun that meets the operational requirements of the gyro-TWT has also been designed. With $\sim$2% velocity spread from 32-50 kV while providing a an α of 0.6-1 the triode configuration provides the necessary tunability to $\sim$5%. maximize the effectiveness of the amplifier. Surface roughness and machining errors are expected to increase the velocity spread to A wraparound input coupler with more than 50% power transmission from fundamental waveguide to the PBG will provide the required mode conversion from the solid state source to the amplifier circuit. For the current configuration a multi-step uptaper provides -20 dB reflection from cutoff to 260 GHz while allowing for axial beam extraction.

Chapter 4

Short Pulse Amplification

4.1 Introduction

In order for an amplifier to perform adequately in pulsed DNP NMR experiments it is not only required to produce kW power levels, it is also necessary to amplify pulse trains without distortion. For pulse trains with a frequency spectrum on the order of the amplifier's bandwidth this could prove problematic and has not been previously investigated. Using an existing experimental setup at 140 GHz, linear amplification of pulses was thoroughly investigated and compared to a theory for amplification of short pulses in a gyro-TWT that was derived in Section 2.7. In a gyro-TWT gain occurs near the intersection of the beam line in Equation (1.1) and the waveguide dispersion line in Equation (1.2) as shown for the HE_{06} mode of a confocal waveguide in Figure 4-1. The 140 GHz gyro-TWT used in this experiment has produced a 3-dB gain bandwidth of over 1.5 GHz (1.1%) with a peak power of 570 W from a 38.5 kV, 2.5 A electron beam [29]. A maximum output power of 0.82 kW was achieved. The amplifier circuit is an overmoded quasi-optical confocal waveguide consisting of three 7 cm long gain sections separated by two 3.7 cm severs. Figure 4-1 shows a cross section of the confocal waveguide with the waveguide rails of 6.93 mm radius separated by a distance $L_\perp$ of 6.93 mm. The gyro-TWT operates in the HE_{06} mode. The electron beam is tuned to a grazing intersection with the HE_{06} waveguide mode. The beam line intersection with the HE_{05} mode can lead to backward wave oscillations

limiting the beam current in the circuit. By adjusting parameters such as the main magnetic field, the electron beam voltage and the voltage on the control anode, the beam line may be moved from close to the cutoff position to much farther from the cutoff position.

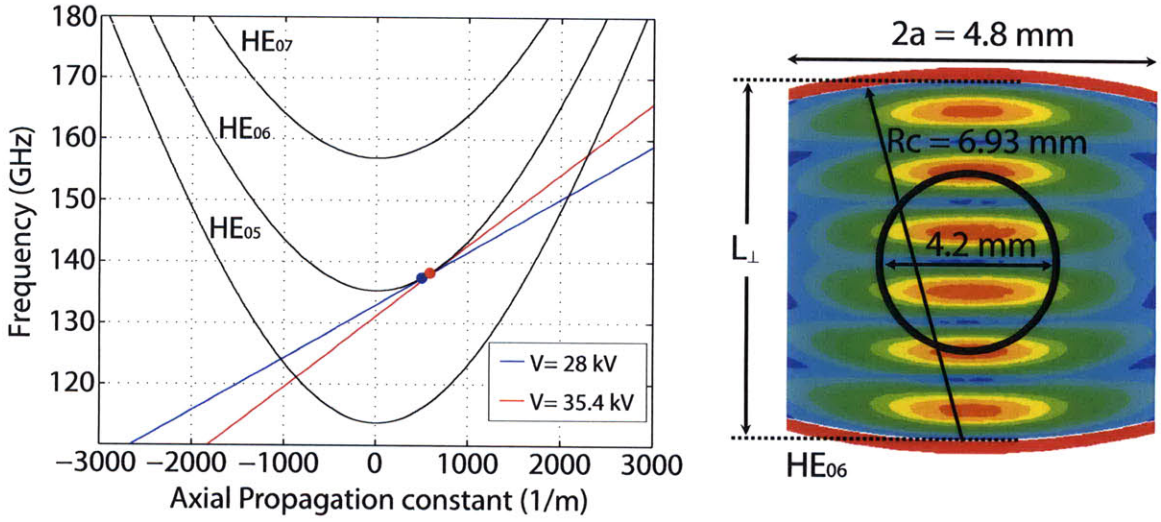

Figure 4-1: Dispersion diagram of HE_{06} gyro-TWT in a confocal waveguide (left) and cross sectional view (right). The annular electron beam has a 4.2 mm diameter.

For this study, the gyro-TWT was first operated in longer pulses, on the microsecond scale, to establish the gain and bandwidth in long pulse (quasi-CW) operation, prior to the short pulse tests. Results were obtained at voltages of 35.4 kV and 28 kV, with 1.8 A beam current and 5.01 T magnetic field. Figure 4-2 and Figure 4-3 show the theoretical and measured gain bandwidth for two operating conditions that were investigated. The measured gain, for a 1 μs pulse, was as high as 30 dB and the output power was about 10 W, which is well within the linear gain regime. The linear regime operation was verified by measuring the input power vs. output power over a range of input power values, as shown in Figure 4-4. Simulations of the gyro-TWT were performed using the computer code MAGY [10] with a beam velocity ratio α = 1.1 and 1.4 and a perpendicular velocity spread of 9.5% and 12% for 35.4 kV and 28 kV, respectively. The measured data points in Figure 4-2 and Figure 4-3 are in

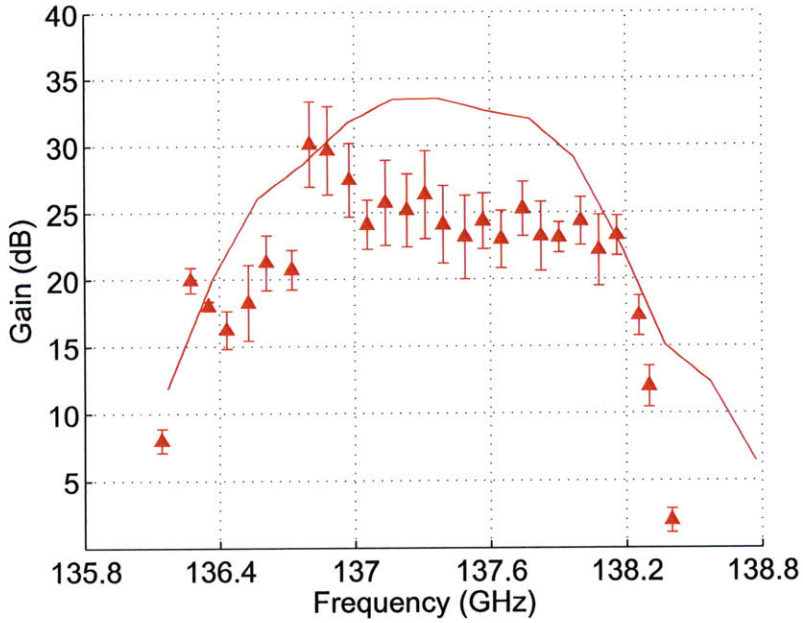

Figure 4-2: Measured (dots) and calculated (solid line) gain-bandwidth curve for a beam voltage of 28 kV.

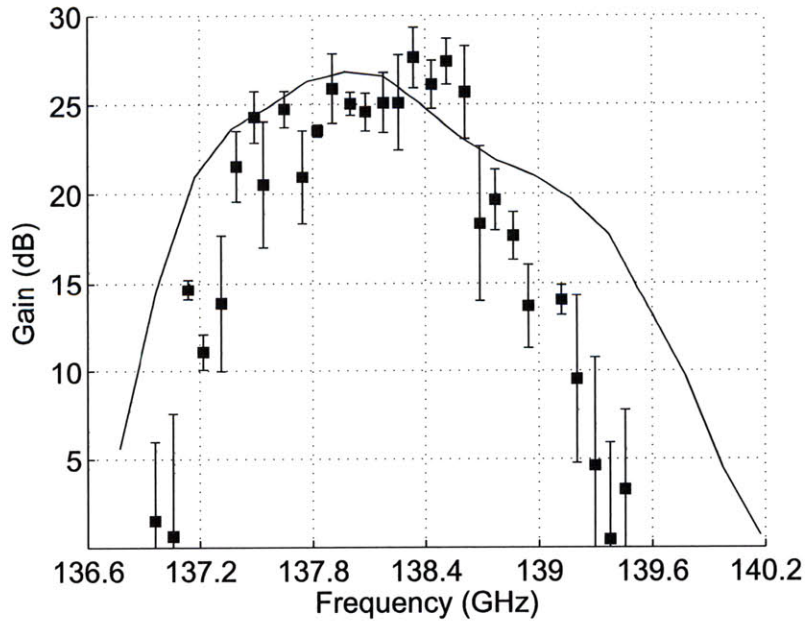

Figure 4-3: Measured (dots) and calculated (solid line) gain-bandwidth curve for a beam voltage of 35.4 kV.

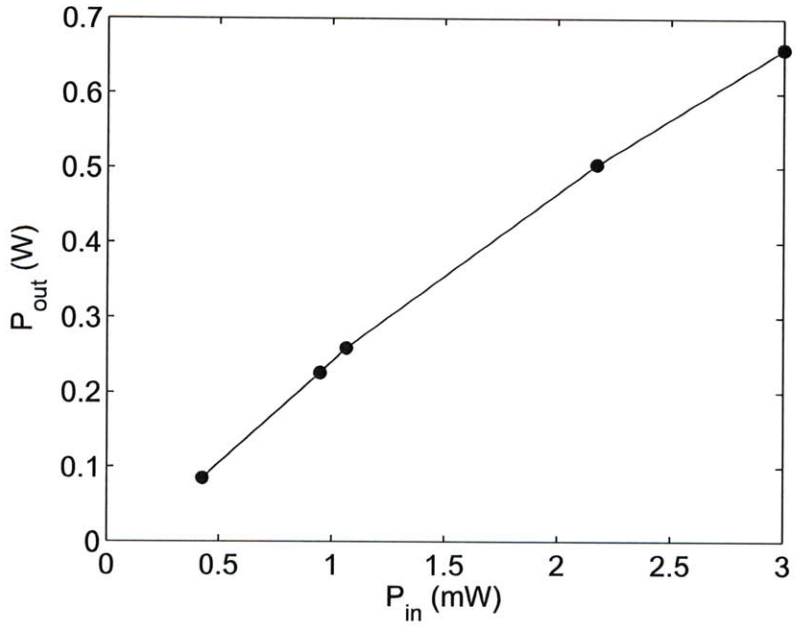

Figure 4-4: Measured input and output power at 137.8 GHz for the 35.4 kV operating point. The gain is 23.5±0.34 dB

reasonable agreement with theoretical predictions. The 3-dB bandwidths of both cases are about 1.2 GHz, with a center frequency of 137.4 GHz and 138.1 GHz for the 28kV and 35.4 kV operating points respectively. Following the microsecond gain experiments, we conducted tests of the gain and dispersion of the gyro-TWT with picosecond input pulses.

4.2 Experimental Setup

Figure 4-5 shows a schematic of the picosecond pulse amplifier experiments. The picosecond drive pulses are generated by a solid-state source consisting of an X-band mixer switch with an up-converter to 35 GHz and a Virginia Diodes, Inc × 4 multiplier to 140 GHz [30]. The driver input at the gyro-TWT after the 3-dB directional coupler as shown in Figure 4-5 was approximately 16 mW over the 135-143 GHz range in pulses as short as 400 ps. The detector diode outputs were measured by an oscilloscope with a 10-GHz bandwidth and a 40 GS/s sampling rate. The

relative temporal responses of the input diode and the output diode were tested and compared while simultaneously connected to a common directional coupler. The temporal responses of the two detector diodes from 400 ps to 1 ns agreed to within 5%.

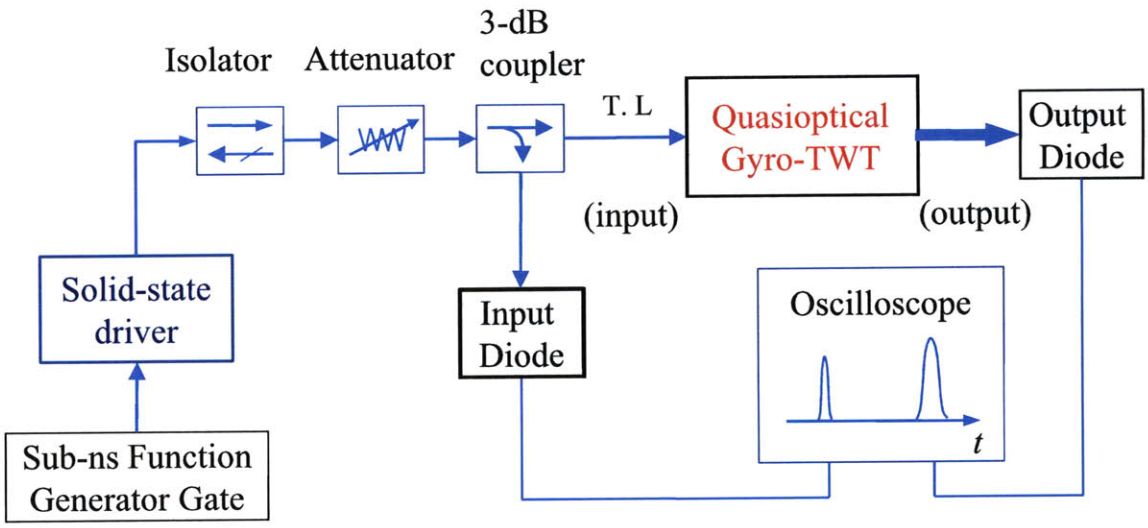

Figure 4-5: Schematic diagram of the picosecond pulse amplification in a quasioptical gyro-TWT.

4.3 Short Pulse Amplification

As described in Section 2.7, the pulse in the interaction circuit is expected to suffer from two dispersive effects. Both waveguide dispersion and gain dispersion will play a major role in the broadening of pulses in the amplifier. If the amplifier is operating in the linear regime, the pulse's interaction with the electron beam can be described by

$$\frac{\partial}{\partial z}a(z,\omega) = -ik_z a + G(\omega)a \tag{4.1}$$

where $a(z,\omega)$ is the frequency spectrum of the pulse, k_z is the axial wave number and $G(\omega)$, the linear gain over the spectral range of the pulse, can be determined from theory or from experiment [16], as in Figure 4-2 and Figure 4-3. The effects of dispersion can be modeled as distortions to the frequency spectrum of the pulse as it

travels through the interaction circuit. Theoretical broadening curves were generated by observing the broadening of Gaussian pulses as they traveled through the circuit. For a pulse $A(z_0, t)$ at the start of the circuit, the frequency spectrum is given by,

$$a(\omega) = \frac{1}{\sqrt{2\pi}} \int_{-\infty}^{\infty} A(z_0, t) e^{-i\omega t}\, dt. \tag{4.2}$$

and we can propagate the pulse in the frequency domain using the solution to Equation (4.1)

$$a'(z, \omega) = a(\omega) e^{-ik_z z} e^{G(\omega) z}. \tag{4.3}$$

For the Fourier transform of a pulse, if we amplify and advance the phase of every spectral component, it will be equivalent to propagating the pulse through the circuit. Performing an inverse Fourier transform on this new spectrum

$$A'(z_1, t) = \frac{1}{\sqrt{2\pi}} \int_{-\infty}^{\infty} a(\omega) e^{-ik_z z_1} e^{G(\omega) z_1} e^{i\omega t}\, d\omega \tag{4.4}$$

produces the output pulse in the time domain. Equation (4.4) shows that gain dispersion plays a significant role in broadening of picosecond pulses when the spectral bandwidth of the amplified pulse is comparable to the gain bandwidth of the gyro-TWT. In addition to measuring $G(\omega)$ experimentally, the cutoff frequency must be determined in order to calculate the phase advance produced by k_z. Using a network analyzer to measure the cutoff frequency for traditional fundamental mode waveguide is relatively easy. However, the interaction circuit has the added complications of being highly lossy and requiring coupling from a fundamental mode waveguide to the HE_{06} mode. Furthermore, the cutoff frequency could be altered when the circuit is installed in the magnet bore. An alternate approach to determine the cutoff frequency is finding the best fit for the time of flight for a pulse traveling through the circuit.

In order to benchmark our procedures, we measured the dispersion of picosecond pulses in an empty WR4 waveguide with cutoff frequency of 139.25±0.1 GHz. The cutoff frequency was measured using a vector network analyzer (VNA) as shown in

Figure 4-6. It is simple to calculate (blue line) the attenuation of the TE_{10} mode in 10 cm of WR4 waveguide for a specific cutoff frequency, showing excellent agreement with the measured data (green line) in Figure 4-6. It is important to calibrate the measurement at the input and output ports of the WR4 waveguide. The inclusion of the WR4-WR6 transitions in the measurement (red line) shows a significant difference in the attenuation due to the characteristics of the transitions.

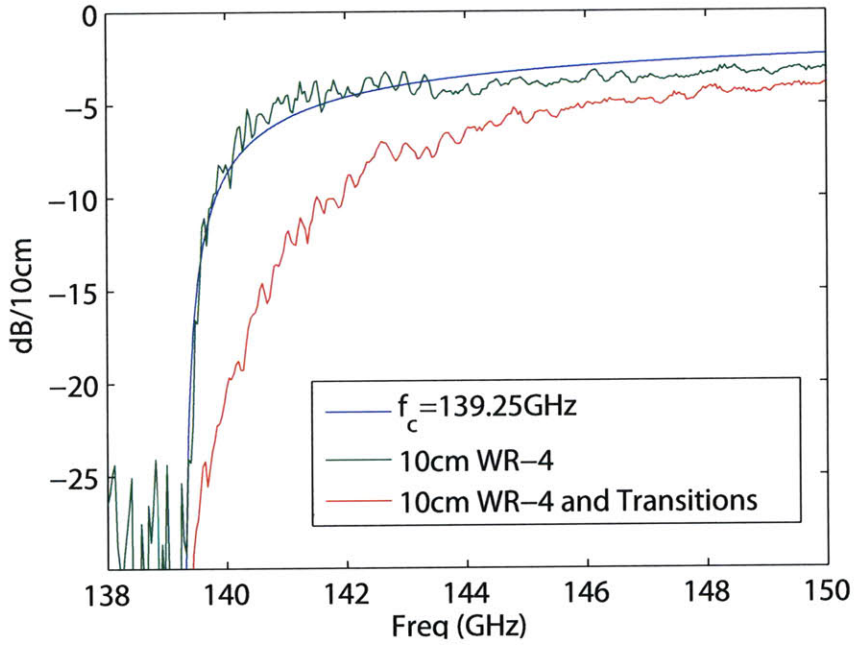

Figure 4-6: Attenuation as a function of frequency in a 10 cm section of WR4 waveguide.

In the case of empty WR4 waveguide only waveguide dispersion, as given by Equation (1.2), is present. In Figure 4-7(a) pulses traveling through 10 cm of the WR4 waveguide showed pulse transit time delays that are highly dependent on the cutoff frequency of the waveguide. The time of flight data in Figure 4-7(a) is in excellent agreement with the 139.25 GHz cutoff measured using the VNA.

A waveguide filled with an active medium (the electron beam in this case) shows an additional dispersive effect due to that medium, especially near cyclotron resonance. In Figure 4-7(b) we show the measured transit time delay for 500 ps pulses

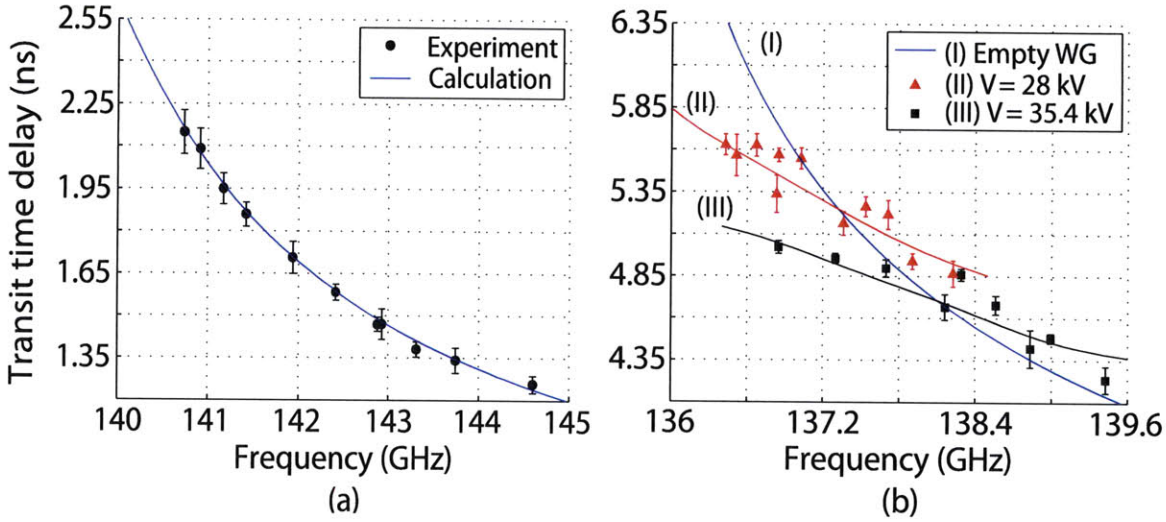

Figure 4-7: Measured (dots) and calculated (solid line) transit time delay of 500 ps pulses in (a) 10 cm long WR4 waveguide with a cutoff frequency of 139.25 GHz and (b) the 28.4 cm gyro-TWT confocal waveguide structure with a cutoff frequency of 135.0 $\pm$ 0.3 GHz.

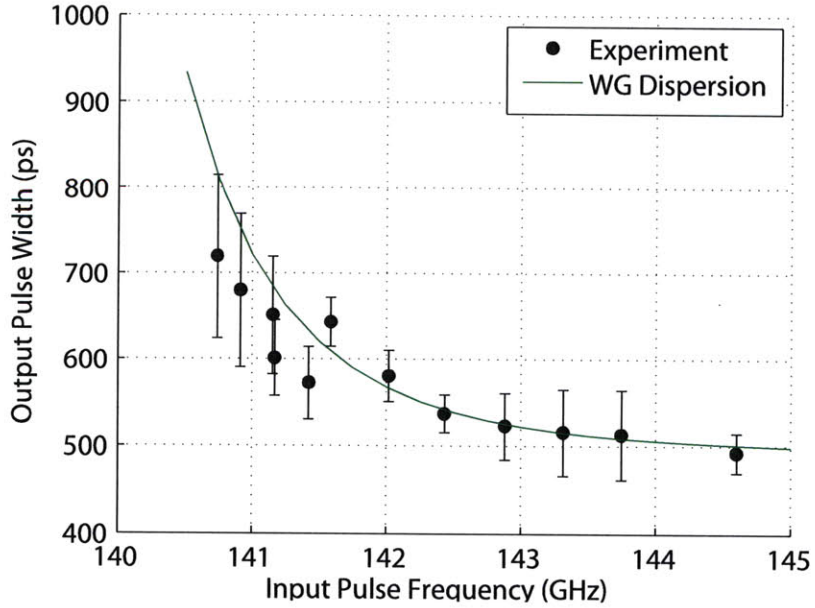

Figure 4-8: Output pulse width as a function of input frequency for 10 cm WR4 waveguide and a constant input pulse width of 500$\pm$25 ps.

traveling through the 28.4 cm confocal waveguide structure of the gyro-TWT at two different voltages as a function of frequency. Equation (4.4) was used to calculate the theoretical results shown in Figure 4-7(b). The theory curves use the $G(\omega)$ that was measured in Figure 4-2 and Figure 4-3 and a cutoff of 135 GHz. These results are in excellent agreement with the experimental data at the two different operating voltages. In Figure 4-7(b), (I) is the calculated transit time delay in the gyro-TWT including only waveguide dispersion, that is, for the empty waveguide with no electron beam present; (II) and (III) are the measured and calculated transit time delay of picosecond pulses in the gyro-TWT for two different beam voltages, namely 28 kV and 35.4 kV. These results show that the active medium, the electron beam, has a significant effect on the transit time.

The broadening of ps pulses in cold WR4 waveguide was also used as a bench mark. The waveguide dispersion causes the ps pulses in the WR4 waveguide to undergo significant pulse broadening. The broadening results for a constant input pulse width of 500±25 ps as a function of frequency are shown in Figure 4-8. As expected, pulses of a frequency that is closer to the waveguide cutoff are broadened much more severely.

Similarly, Gaussian pulses of the same width but different frequencies can be amplified in the gyro-TWT where both dispersive mechanisms will be present. For the 28 kV operating point pulses with an input width of 425±25 ps were amplified for a variety of input frequencies. The results in Figure 4-9 show that the minimum broadening occurs slightly above center frequency of the gain spectrum because of the strong effects from waveguide dispersion. As the frequency moves away from this minimum, either closer to or further from the cutoff of the interaction circuit, the broadening increases. The frequency spectrum of a pulse that is amplified with an input frequency close to the edge of the gain spectrum is severely distorted resulting in pulse broadening. There is very good agreement between the measured and calculated broadening values when both forms of dispersion are included. Figure 4-9 also shows the theoretical broadening curve for the interaction circuit with only

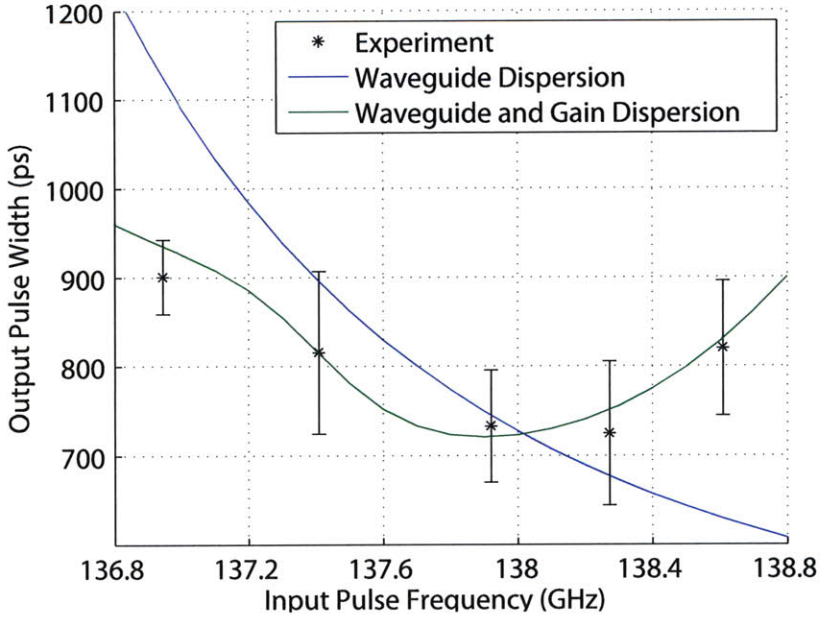

Figure 4-9: Output pulse width as a function of input frequency for a beam voltage of 28kV and a fixed input pulse width of 425±25 ps.

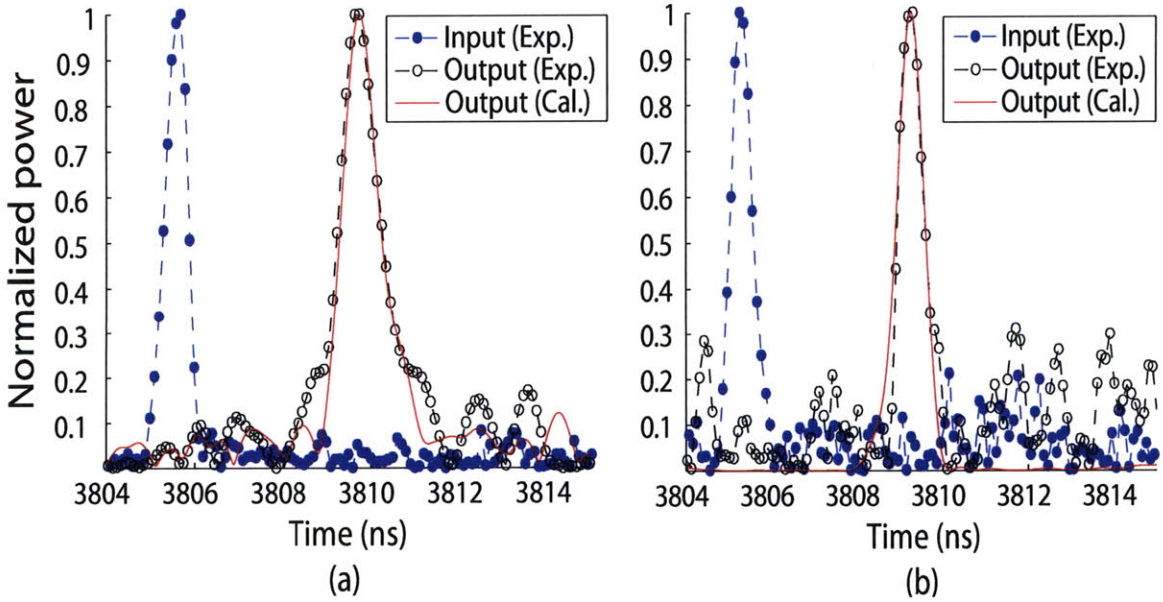

Figure 4-10: Pulse shapes for an input pulse of 580 ps at the 35.4 kV operating point. The output pulse at (a) 137.3 GHz has a measured width of 1045 ps and (b) at 138.13 GHz has a measured width of 660 ps.

waveguide dispersion. It is evident that the broadening data is in stark contrast with these calculations. This shows the importance of considering not only the effect that waveguide dispersion will have on short pulse amplification, but also the effect of gain dispersion.

The time domain recordings of pulse envelopes taken by detector diodes, as shown in the schematic of Figure 4-5 before and after amplification in the gyro-TWT, can also be used to compare with theory. Figure 4-10 shows an example of the measured temporal shapes of input and output pulses. Operating at 35.4 kV with a 600 ps input pulse, the detected output pulse envelopes vary with frequency in good agreement with the numerical simulation results based on Equation (4.4). From Figure 4-10, we can clearly see that for a sub-nanosecond pulse traversing an interaction space with a gain bandwidth of 1.2 GHz, the output pulse will suffer significant pulse broadening in the time domain, especially if the frequency of the pulse is not centered in the gain spectrum.

4.3.1 Pulse Broadening Curves

Figure 4-11 and Figure 4-12 show experimental results and theoretical calculations of the output pulse width vs. input pulse width for the gyro-TWT, showing clear evidence of pulse broadening effects. For very long pulses (not shown in the figure), greater than a few nanoseconds, there is no pulse broadening, as expected; the output pulse has the same width as the input pulse. Results are presented for the two beam voltages for which the gain spectra are shown in Figure 4-2 and Figure 4-3. Figure 4-11(b) and Figure 4-12(b) show pulse broadening curves at the center of the gain spectrum where the broadening due to gain narrowing should be minimized. We also find that even though both operating points have a similar gain bandwidth, for the case of Figure 4-11(b) the broadening is more severe than Figure 4-12(b). Theory shows that this arises because the frequency of the pulse in case Figure 4-11(b) is 0.75 GHz closer to cutoff, thus increasing the waveguide dispersion contribution to

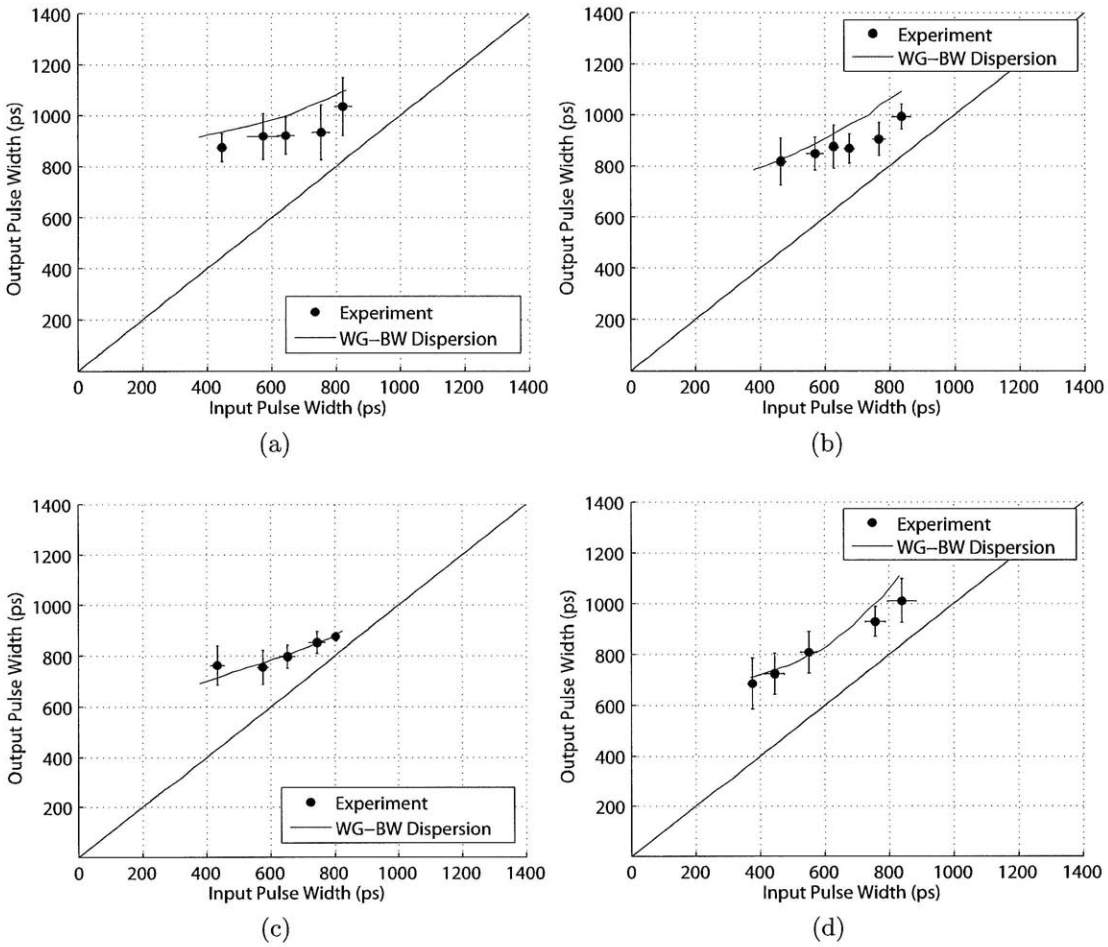

Figure 4-11: Measured (dots) and calculated (solid lines) output pulse width after amplification as a function of input pulse width for 28 kV and (a)136.94 GHz, (b)137.4 GHz, (c) 137.92 GHz and (d)138.2 GHz.

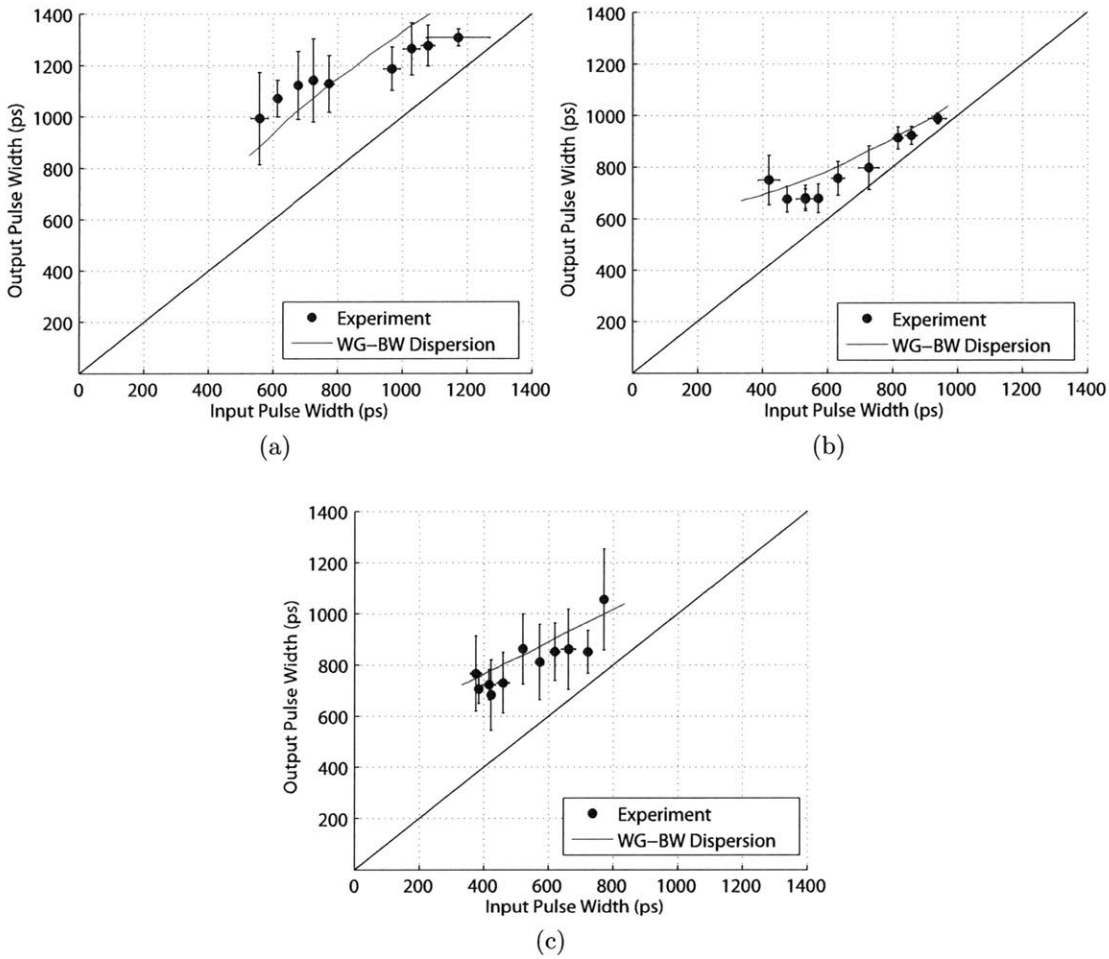

Figure 4-12: Measured (dots) and calculated (solid lines) output pulse width after amplification as a function of input pulse width for 35.4 kV and (a)137.3 GHz, (b)138.13 GHz and (c)138.8 GHz.

the broadening. Figure 4-12(a)-(c) was produced for the same beam voltage (35 kV), but for different input pulse frequencies. Figure 4-12(b) displays the least broadening because it is centered in the gain spectrum of the amplifier at 138.13 GHz. Figure 4-12(a) is both 0.85 GHz below the center of the gain spectrum and closer to cutoff. As a result, pulse broadening arises from both gain narrowing and the proximity to waveguide cutoff, resulting in very large broadening. At the 138.8 GHz operating frequency of Figure 4-12(c), pulse broadening is also worse than Figure 4-12(b) because this point is 0.65 GHz above the center of the gain spectrum, causing gain narrowing. Data taken at 28kV is shown in Figure 4-11(a)-(d) for different input pulse frequencies. Similar observations can be made about pulse broadening. The closer to cutoff the more severe the effect of waveguide dispersion. So much so that the minimum broadening is not in the middle of the gain spectrum (also visible in Figure 4-9). Furthermore, amplification of pulses at the limits of the gain spectrum also produces severe pulse broadening. Theoretical calculations of output pulse width vs. input pulse width were carried out for the cases shown in Figure 4-11 and Figure 4-12 using Gaussian pules and Equation (4.4), based on the experimentally measured gain spectra of Figure 4-2 and Figure 4-3, respectively. As seen in Figure 4-12 and Figure 4-11, the theoretical curves are in very good agreement with the experimental measurements.

4.4 Summary

In summary, the amplification of a sub-ns pulse in a 140 GHz gyro-TWT was successfully studied over a wide range of parameters. The experimental data of pulse broadening and transit time delay in the gyro-TWT are in good agreement with calculations in the linear gain regime that take into account the effects of waveguide dispersion and finite gain bandwidth. These results show that amplification of short pulses in a gyro-TWT will display significant broadening if the operating point is selected close to cutoff or close to the edge of the gain bandwidth. Based on the present results, it is crucial to both choose an operating frequency at least several

percent above the cutoff of the waveguide circuit and to provide the necessary gain bandwidth of at least 1 GHz. These guidelines will permit use of the gyro-TWT for its intended application, namely amplification of pulses down to 1 ns pulse length for use in pulsed dynamic nuclear polarization enhanced nuclear magnetic resonance experiments. The criteria described here are satisfied with the design of the 250 GHz gyro-TWT presented in the previous chapter. The 250 GHz gyro-TWT was designed to have 3GHz of bandwidth centered at 3% above cutoff.

Bibliography

[1] G.P. Agrawal. Effect of gain dispersion on ultrashort pulse amplification in semiconductor laser amplifiers. *IEEE Journal of Quantum Electronics*, 27(6):1843–1849, 1991.

[2] J.M. Baird and W. Lawson. Magnetron injection gun(MIG) design for gyrotron applications. *International Journal of Electronics*, 61(6):953–967, 1986.

[3] A.B. Barnes, G. De Paëpe, P.C.A. van der Wel, K.N. Hu, C.G. Joo, V.S. Bajaj, M.L. Mak-Jurkauskas, J.R. Sirigiri, J. Herzfeld, R.J. Temkin, et al. High-field dynamic nuclear polarization for solid and solution biological NMR. *Applied Magnetic Resonance*, 34(3):237–263, 2008.

[4] L.R. Barnett, J.M. Baird, Y.Y. Lau, K.R. Chu, and V.L. Granatstein. A high gain single stage gyrotron traveling-wave amplifier. In *1980 International Electron Devices Meeting*, volume 26, pages 314–317, 1980.

[5] B.N. Basu. *Electromagnetic theory and applications in beam-wave electronics.* World Scientific Pub. Co. Inc., 1996.

[6] M. Bennati, C.T. Farrar, J.A. Bryant, S.J. Inati, V. Weis, G.J. Gerfen, P. Riggs-Gelasco, J. Stubbe, and R.G. Griffin. Pulsed electron-nuclear double resonance (ENDOR) at 140 GHz. *Journal of Magnetic Resonance*, 138(2):232–243, 1999.

[7] M. Blank, P. Borchard, S. Cauffman, F. Felch, and P.A. CPI. Broadband W-band gyrotron amplifier development. In *2006 International Conference on Infrared Millimeter Waves and Teraherz Electronics*, page 198, 2006.

[8] M. Blank, P. Borchard, S. Cauffman, and K. Felch. Demonstration of a broadband W-band gyro-TWT amplifier. In *2005 IEEE International Conference on Plasma Science*, page 112, 2005.

[9] D.R. Bolton, P.A.S. Cruickshank, D.A. Robertson, and G.M. Smith. Sub-nanosecond coherent pulse generation at millimetre-wave frequencies. *Electronics Letters*, 43(6):43–44, 2007.

[10] M. Botton, T.M. Antonsen Jr, B. Levush, K.T. Nguyen, and A.N. Vlasov. MAGY: a time-dependent code for simulation of slow and fastmicrowave sources. *IEEE Transactions on Plasma Science*, 26(3):882–892, 1998.

[11] V.L. Bratman, A.W. Cross, G.G. Denisov, W. He, A.D.R. Phelps, K. Ronald, S.V. Samsonov, C.G. Whyte, and A.R. Young. High-gain wide-band gyrotron traveling wave amplifier with a helically corrugated waveguide. *Physical Review Letters*, 84(12):2746–2749, 2000.

[12] K.R. Chu. The electron cyclotron maser. *Reviews of Modern Physics*, 76(2):489–540, 2004.

[13] K.R. Chu, H.Y. Chen, C.L. Hung, T.H. Chang, L.R. Barnett, S.H. Chen, and T.T. Yang. Ultrahigh gain gyrotron traveling wave amplifier. *Physical Review Letters*, 81(21):4760–4763, 1998.

[14] K.R. Chu, A.T. Drobot, H.H. Szu, and P. Sprangle. Theory and simulation of the gyrotron traveling wave amplifier operating at cyclotron harmonics. *IEEE Transactions on Microwave Theory and Techniques*, 28(4):313–317, 1980.

[15] K.R. Chu and J.L. Hirshfield. Comparative study of the axial and azimuthal bunching mechanisms in electromagnetic cyclotron instabilities. *Physics of Fluids*, 21:461, 1978.

[16] K.R. Chu and A.T. Lin. Gain and bandwidth of the gyro-TWT and CARM amplifiers. *IEEE Transactions on Plasma Science*, 16(2):90–104, 1988.

[17] B.G. Danly and R.J. Temkin. Generalized nonlinear harmonic gyrotron theory. *Physics of Fluids*, 29(2):561, 1986.

[18] K.L. Felch, B.G. Danly, H.R. Jory, K.E. Kreischer, W. Lawson, B. Levush, and R.J. Temkin. Characteristics and applications of fast-wave gyrodevices. *Proceedings of the IEEE*, 87(5):752–781, 1999.

[19] AV Gapanov. Addendum izvestia. *Izv. VUZ. Radiofizika*, 2:450–462, 1959.

[20] A.V. Gapanov. Interaction of helical electron beams with the electromagnetic field in a waveguide. *Radiotekh. I Elektron.*, 10:1414–1153, 1961.

[21] N.S. Ginzburg, I.V. Zotova, A.S. Sergeev, I.V. Konoplev, A.D.R. Phelps, A.W. Cross, S.J. Cooke, V.G. Shpak, M.I. Yalandin, S.A. Shunailov, et al. Experimental observation of cyclotron superradiance under group synchronism conditions. *Physical Review Letters*, 78(12):2365–2368, 1997.

[22] M.Y. Glyavin, A.G. Luchinin, and G.Y. Golubiatnikov. Generation of 1.5-kW, 1-THz coherent radiation from a gyrotron with a pulsed magnetic field. *Physical Review Letters*, 100(1):15101, 2008.

[23] M.K. Haldar and A.H. Beck. Simple derivation of the expression for the synchronous field in circular cylindrical cavity gyrotrons. *Electronics Letters*, 15:487, 1979.

[24] H.A. Haus. Waves and fields in optoelectronics. *Prentice-Hall Inc.*, 1984.

[25] H.A. Haus and W.S. Wong. Solitons in optical communications. *Reviews of Modern Physics*, 68(2):423–444, 1996.

[26] M.K. Hornstein. *A continuous-wave second harmonic gyrotron oscillator at 460GHz.* PhD thesis, Massachusetts Institute of Technology, 2005.

[27] M.K. Hornstein, V.S. Bajaj, R.G. Griffin, K.E. Kreischer, I. Mastovsky, M.A. Shapiro, J.R. Sirigiri, and R.J. Temkin. Second harmonic operation at 460 GHz and broadband continuous frequency tuning of a gyrotron oscillator. *IEEE Transactions on Electron Devices*, 52(5):798–807, 2005.

[28] T. Idehara, K. Yoshida, N. Nishida, I. Ogawa, M.L. Pereyaslavets, and T. Tatsukawa. CW operation of a submillimeter wave gyrotron (gyrotron FU IV) for high stability of the output frequency. *International Journal of Infrared and Millimeter Waves*, 19(6):793–801, 1998.

[29] C.D. Joye, M.A. Shapiro, J.R. Sirigiri, and R.J. Temkin. Demonstration of a 140-GHz 1-kW confocal gyro-traveling-wave Amplifier. *IEEE Transactions on Electron Devices*, 56:818–827, 2009.

[30] H.J. Kim, C.D. Joye, M.A. Shapiro, J.R. Sirigiri, R.J. Temkin, P.P. Woskov, T. Maly, and R.G. Griffin. An overmoded 140 GHz, 1 kW quasioptical gyro-twt with an internal mode converter. In *2009 International Conference on Infrared, Millimeter, and Terahertz Waves*, pages 1–2. IEEE, 2009.

[31] H.J. Kim, E.A. Nanni, M.A. Shapiro, J.R. Sirigiri, and R.J. Temkin. Experimental Measurement of Picosecond Pulse Amplification in a 140 GHz Gyro-TWT. In *2010 IEEE International Vacuum Electronics Conference*, pages 193–194, 2009.

[32] N.F. Kovalev and A.V. Palitsyn. Method of coupled waves in the theory of excitation of waveguides by high-frequency currents with slowly varying amplitudes. *Radiophysics and Quantum Electronics*, 48(3):177–184, 2005.

[33] L. Landau. Diamagnetismus der metalle. *Zeitschrift fur Physik A Hadrons and Nuclei*, 64(9):629–637, 1930.

[34] K. Nguyen, B. Danly, B. Levush, M. Blank, R. True, K. Felch, and P. Borchard. Electron gun and collector design for 94-GHz gyro-amplifiers. In *Particle Accelerator Conference, 1997. Proceedings of the 1997*, volume 3, 1997.

[35] K.T. Nguyen, J.P. Calame, D.E. Pershing, B.G. Danly, M. Garven, B. Levush, and T.M. Antonsen Jr. Design of a Ka-band gyro-TWT for radar applications. *IEEE Transactions on Electron Devices*, 48(1):108 – 115, 2001.

[36] T. Notake, T. Saito, Y. Tatematsu, A. Fujii, S. Ogasawara, L. Agusu, I. Ogawa, T. Idehara, and VN Manuilov. Development of a novel high power sub-THz second harmonic gyrotron. *Physical Review Letters*, 103(22):225002, 2009.

[37] G.S. Nusinovich. *Introduction to the Physics of Gyrotrons.* Johns Hopkins University Press, 2004.

[38] G.S. Nusinovich and H. Li. Theory of gyro-travelling-wave tubes at cyclotron harmonics. *International Journal of Electronics*, 72(5):895–907, 1992.

[39] G.S. Park, S.Y. Park, R.H. Kyser, A.K. Ganguly, and C.M. Armstrong. Gain broadening in an inhomogeneous gyrotron traveling wave amplifier. In *1990 Electron Devices Meeting Technical Digest*, pages 703–705, 1990.

[40] J. Schneider. Stimulated emission of radiation by relativistic electrons in a magnetic field. *Physical Review Letters*, 2(12):504–505, 1959.

[41] M.A. Shapiro. Private communication. 2010.

[42] J.R. Sirigiri. *A novel wideband gyrotron traveling wave amplifier.* PhD thesis, Massachusetts Institute of Technology, 2003.

[43] J.R. Sirigiri, K.E. Kreischer, J. Machuzak, I. Mastovsky, M.A. Shapiro, and R.J. Temkin. Photonic-band-gap resonator gyrotron. *Physical Review Letters*, 86(24):5628–5631, 2001.

[44] J.R. Sirigiri, M.A. Shapiro, and R.J. Temkin. High-power 140-GHz quasioptical gyrotron traveling-wave amplifier. *Physical Review Letters*, 90(25):258302, 2003.

[45] E.I. Smirnova, C. Chen, M.A. Shapiro, J.R. Sirigiri, and R.J. Temkin. Simulation of photonic band gaps in metal rod lattices for microwave applications. *Journal of Applied Physics*, 91:960, 2002.

[46] R.J. Temkin, K. Kreischer, S.M. Wolfe, D.R. Cohn, and B. Lax. High frequency gyrotrons and their application to tokamak plasma heating. *Journal of Magnetism and Magnetic Materials*, 11(1-3):368–371, 1979.

[47] R.J. Temkin, K.E. Kreischer, W.J. Mulligan, S. MacCabe, and H.R. Fetterman. A 100 kW, 140 GHz pulsed gyrotron. *International Journal of Infrared and Millimeter Waves*, 3(4):427–437, 1982.

[48] R.Q. Twiss. Radiation transfer and the possibility of negative absorption in radio astronomy. *Australian Journal of Physics*, 11(4):567–579, 1958.

[49] V.K. Yulpatov. Nonlinear theory of the interaction between a periodic electron beam and an electromagnetic wave. *Radiophysics and Quantum Electronics*, 10(6):471–476, 1967.

[50] V.K. Yulpatov. Averaged equations for oscillations in the CRM-monotron. *3rd Winter School for Engineers, Saratov*, 4:144–178, 1974.

[51] N.I. Zaytsev, T.B. Pankratova, M.I. Petelin, and V.A. Flyagin. Millimeter-and submillimeter-wave gyrotrons. *Radio Eng. Electron. Phys*, 19(5):103–107, 1974.